NUREG/CR–4667
ANL–95/41
Vol. 20

Environmentally Assisted Cracking in Light Water Reactors

Semiannual Report
October 1994 – March 1995

Prepared by
H. M. Chung, O. K. Chopra, D. J. Gavenda, A. G. Hins,
T. F. Kassner, W. E. Ruther, W. J. Shack, and W. K. Soppet

Argonne National Laboratory

Prepared for
U.S. Nuclear Regulatory Commission

D602
1/1

AVAILABILITY NOTICE

Availability of Reference Materials Cited in NRC Publications

Most documents cited in NRC publications will be available from one of the following sources:

1. The NRC Public Document Room, 2120 L Street, NW., Lower Level, Washington, DC 20555-0001

2. The Superintendent of Documents, U.S. Government Printing Office, P. O. Box 37082, Washington, DC 20402-9328

3. The National Technical Information Service, Springfield, VA 22161-0002

Although the listing that follows represents the majority of documents cited in NRC publications, it is not intended to be exhaustive.

Referenced documents available for inspection and copying for a fee from the NRC Public Document Room include NRC correspondence and internal NRC memoranda; NRC bulletins, circulars, information notices, inspection and investigation notices; licensee event reports; vendor reports and correspondence; Commission papers; and applicant and licensee documents and correspondence.

The following documents in the NUREG series are available for purchase from the Government Printing Office: formal NRC staff and contractor reports, NRC-sponsored conference proceedings, international agreement reports, grantee reports, and NRC booklets and brochures. Also available are regulatory guides, NRC regulations in the *Code of Federal Regulations*, and *Nuclear Regulatory Commission Issuances*.

Documents available from the National Technical Information Service include NUREG-series reports and technical reports prepared by other Federal agencies and reports prepared by the Atomic Energy Commission, forerunner agency to the Nuclear Regulatory Commission.

Documents available from public and special technical libraries include all open literature items, such as books, journal articles, and transactions. *Federal Register* notices, Federal and State legislation, and congressional reports can usually be obtained from these libraries.

Documents such as theses, dissertations, foreign reports and translations, and non-NRC conference proceedings are available for purchase from the organization sponsoring the publication cited.

Single copies of NRC draft reports are available free, to the extent of supply, upon written request to the Office of Administration, Distribution and Mail Services Section, U.S. Nuclear Regulatory Commission, Washington, DC 20555-0001.

Copies of industry codes and standards used in a substantive manner in the NRC regulatory process are maintained at the NRC Library, Two White Flint North, 11545 Rockville Pike, Rockville, MD 20852-2738, for use by the public. Codes and standards are usually copyrighted and may be purchased from the originating organization or, if they are American National Standards, from the American National Standards Institute, 1430 Broadway, New York, NY 10018-3308.

DISCLAIMER NOTICE

NUREG/CR–4667
ANL–95/41
Vol. 20

Environmentally Assisted Cracking in Light Water Reactors

Semiannual Report
October 1994 – March 1995

Manuscript Completed: December 1995
Date Published: January 1996

Prepared by
H. M. Chung, O. K. Chopra, D. J. Gavenda, A. G. Hins,
T. F. Kassner, W. E. Ruther, W. J. Shack, and W. K. Soppet

Argonne National Laboratory
9700 South Cass Avenue
Argonne, IL 60439

M. McNeil, NRC Project Manager

Prepared for
Division of Engineering Technology
Office of Nuclear Regulatory Research
U.S. Nuclear Regulatory Commission
Washington, DC 20555–0001
NRC Job Code A2212

Previous Documents in Series

Environmentally Assisted Cracking in Light Water Reactors Semiannual Report April—September 1985, NUREG/CR–4667 Vol. I, ANL–86–31 (June 1986).

Environmentally Assisted Cracking in Light Water Reactors Semiannual Report October 1985—March 1986, NUREG/CR–4667 Vol. II, ANL–86–37 (September 1987).

Environmentally Assisted Cracking in Light Water Reactors Semiannual Report April—September 1986, NUREG/CR–4667 Vol. III, ANL–87–37 (September 1987).

Environmentally Assisted Cracking in Light Water Reactors Semiannual Report October 1986—March 1987, NUREG/CR–4667 Vol. IV, ANL–87–41 (December 1987).

Environmentally Assisted Cracking in Light Water Reactors Semiannual Report April—September 1987, NUREG/CR–4667 Vol. V, ANL–88–32 (June 1988).

Environmentally Assisted Cracking in Light Water Reactors Semiannual Report October 1987—March 1988, NUREG/CR–4667 Vol. 6, ANL–89/10 (August 1989).

Environmentally Assisted Cracking in Light Water Reactors Semiannual Report April—September 1988, NUREG/CR–4667 Vol. 7, ANL–89/40 (March 1990).

Environmentally Assisted Cracking in Light Water Reactors Semiannual Report October 1988—March 1989, NUREG/CR–4667 Vol. 8, ANL–90/4 (June 1990).

Environmentally Assisted Cracking in Light Water Reactors Semiannual Report April—September 1989, NUREG/CR–4667 Vol. 9, ANL–90/48 (March 1991).

Environmentally Assisted Cracking in Light Water Reactors Semiannual Report October 1989—March 1990, NUREG/CR–4667 Vol. 10, ANL–91/5 (March 1991).

Environmentally Assisted Cracking in Light Water Reactors Semiannual Report April—September 1990, NUREG/CR–4667 Vol. 11, ANL–91/9 (May 1991).

Environmentally Assisted Cracking in Light Water Reactors Semiannual Report October 1990—March 1991, NUREG/CR–4667 Vol. 12, ANL–91/24 (August 1991).

Environmentally Assisted Cracking in Light Water Reactors Semiannual Report April—September 1991, NUREG/CR–4667 Vol. 13, ANL–92/6 (March 1992).

Environmentally Assisted Cracking in Light Water Reactors Semiannual Report October 1991—March 1992, NUREG/CR–4667 Vol. 14, ANL–92/30 (August 1992).

Environmentally Assisted Cracking in Light Water Reactors Semiannual Report April—September 1992, NUREG/CR–4667 Vol. 15, ANL–93/2 (June 1993).

Environmentally Assisted Cracking in Light Water Reactors Semiannual Report October 1992—March 1993, NUREG/CR–4667 Vol. 16, ANL–93/27 (September 1993).

Environmentally Assisted Cracking in Light Water Reactors Semiannual Report April—September 1993, NUREG/CR–4667 Vol. 17, ANL–94/26 (June 1994).

Environmentally Assisted Cracking in Light Water Reactors Semiannual Report October 1993—March 1994, NUREG/CR–4667 Vol. 18, ANL–95/2 (March 1995).

Environmentally Assisted Cracking in Light Water Reactors Semiannual Report April—September 1994, NUREG/CR–4667 Vol. 19, ANL–95/25 (September 1995).

Environmentally Assisted Cracking in Light Water Reactors Semiannual Report October 1994–March 1995

by

H. M. Chung, O. K. Chopra, D. J. Gavenda, A. G. Hins,
T. F. Kassner, W. E. Ruther, W. J. Shack, and W. K. Soppet

Abstract

This report summarizes work performed by Argonne National Laboratory on fatigue and environmentally assisted cracking (EAC) in light water reactors (LWRs) from October 1994 to March 1995. Topics that have been investigated include (a) fatigue of carbon and low-alloy steel used in reactor piping and pressure vessels, (b) EAC of Alloy 600 and 690, and (c) irradiation-assisted stress corrosion cracking (IASCC) of Type 304 SS. Fatigue tests were conducted on ferritic steels in water with several dissolved-oxygen (DO) concentrations to determine whether a slow strain rate applied during different portions of a tensile-loading cycle are equally effective in decreasing fatigue life. Tensile properties and microstructures of several heats of Alloy 600 and 690 were characterized for correlation with EAC of the alloys in simulated LWR environments. Effects of DO and electrochemical potential on susceptibility to intergranular cracking of high- and commercial-purity Type 304 SS specimens from control-blade absorber tubes and a control-blade sheath irradiated in boiling water reactors were determined in slow-strain-rate-tensile tests at 289°C. Microchemical changes in the specimens were studied by Auger electron spectroscopy and scanning electron microscopy to determine whether trace impurity elements may contribute to IASCC of these materials.

Contents

Figures

Tables

Executive Summary

Fatigue of Ferritic Piping and Pressure Vessel Steels

Plain carbon and low-alloy steels are used extensively in steam supply systems of pressurized and boiling water nuclear reactors (PWRs and BWRs) as piping and pressure vessel materials. Fatigue tests are being conducted on A106-Gr B carbon steel and A533-Gr B and A302-Gr B low-alloy steels in water and in air at 288°C to establish the effects of material and loading variables on fatigue life. The results indicate only a marginal effect of low-dissolved-oxygen (DO) PWR environment on fatigue life. Environmental effects on fatigue life are significant when five conditions are satisfied simultaneously, viz., applied strain range is above a minimum threshold level, strain rate <1%/s, temperature ≥150°C, DO ≥0.05 ppm, and sulfur content >0.003 wt.% in the steel. A slow strain rate applied during the tensile-loading cycle is more effective in environmentally assisted reduction of fatigue life than when applied during the compressive-loading cycle. During the present reporting period, several exploratory tests were conducted in which a slow strain rate is applied during only a portion of the tensile-loading cycle. The results indicate that a slow strain rate applied during each portion of the tensile-loading cycle above the threshold strain is equally effective in decreasing fatigue life in high-DO water. Fatigue tests were also conducted to establish the effects of room-temperature water and of material orientation on the fatigue life of carbon and low-alloy steels. The results indicate strong effects of orientation and also of strain rate. Structural factors such as ferrite morphology and distribution are responsible for poor fatigue properties. The experimental data are compared with estimates based on the statistical model.

Environmentally Assisted Cracking of Alloys 600 and 690 in Simulated LWR Water

Characterization of several heats of Alloys 600 and 690 for corrosion-fatigue testing was conducted. Tensile properties of cylindrical specimens in air at 25, 290, and 320°C were determined in accordance with ASTM Standard E8. Vickers hardness was measured at room temperature, and average grain size was determined by the procedure in ASTM Standard E112. In general, the tensile properties at 25°C were consistent with those in certified material test reports (CMTRs) supplied by vendors and documentation obtained from the Electric Power Research Institute, Palo Alto, CA, who provided 1-in.-thick plates of many of the heats. The dependence of yield stress of annealed Alloy 600 and 690 specimens on average grain size tends to follow a Petch relation, i.e., $\sigma_y = \sigma_i + k \cdot d^{-1/2}$, where σ_y is the yield stress, d the grain diameter, k an empirical constant, and σ_i the "friction" stress, which is a measure of intrinsic resistance of the material to dislocation motion.

Metallographic specimens were prepared to determine qualitatively, by optical metallography, the degree of grain-boundary carbide coverage. Specimens were polished to an 0.25-μm diamond finish, and a Vickers hardness indentation was made to provide a reference point for subsequent examination to reveal the carbide distribution and grain boundaries after different chemical etching methods. The specimens were electroetched in a 10% H_3PO_4 solution and photographed at 500X to reveal carbides present in the material. The specimens were repolished and electroetched in a 5% nital solution and the specimens were photographed at the same magnification and in the same location with the aid of the hardness indentation to better reveal grain boundaries and thus obtain a qualitative estimate of the extent of carbide precipitation thereon. Five heats of Alloy 600 exhibited either

semicontinuous or continuous carbide precipitation at grain boundaries plus a significant amount of intragranular carbide. Four heats of Alloy 690 revealed continuous precipitation of carbides at grain boundaries and relatively few intragranular carbides. According to published information, precipitate phases in Alloy 600 and 690 are Cr-rich M_7C_3 and $M_{23}C_6$ carbides and TiN.

Fracture-mechanics crack growth rate tests are being conducted at 289 and 320°C on compact-tension specimens of mill-annealed Alloy 600 and thermally treated Alloy 690 in oxygenated water and in deaerated water containing B, Li, and dissolved H_2 at low concentrations.

Irradiation-Assisted Stress Corrosion Cracking of Type 304 SS

The effect of water chemistry on susceptibility to IASCC of Type 304 SS was investigated over a wide range of DO (≈0.001 to ≈8 ppm) and ECP (-600 to +300 mV SHE). The objective was twofold: (1) to better define the effects of water chemistry on susceptibility to intergranular (IG) cracking in slow-strain-rate-tensile (SSRT) tests of specimens fabricated from HP and CP Type 304 SS BWR components, and thereby provide an independent confirmation of the protection potential, and (2) to provide insight into the origin of significant heat-to-heat variation in susceptibility to IASCC. Additional SSRT results were obtained and a correlation of IGSCC susceptibility to grain-boundary microchemistry was made. Effects of DO in water and ECP on susceptibility of CP Type 304 SS BWR neutron-absorber tubes to IASCC in SSRT tests in simulated BWR water at 289°C were similar to those of CP-grades of Type 304 SS in another investigation. Threshold values of DO and ECP to mitigate IASCC of CP-grade materials were confirmed; namely, <0.01 ppm and <-140 mV SHE, respectively.

Susceptibility to IASCC in SSRT tests of HP specimens of Type 304 SS fabricated from BWR components differed from that of CP materials. Namely, the susceptibility of HP heats was less dependent on DO and ECP. This can be explained best by the premise that at low DO and ECP, where the concentration of Cr ions dissolved in water should be negligible, the catalytic role of F in water promotes anodic dissolution of Fe at the crack tip. HP-grade neutron-absorber tubes were considerably more susceptible to IASCC than CP tubes or a control-blade sheath. Grain boundaries in HP materials were characterized by lower concentrations of Cr, Ni, and Li and higher concentrations of F, V, and N than those of CP-grade materials, indicating that higher levels of Cr, Ni, and B and lower levels of F, V, and N in these steels tend to suppress IASCC. Inclusions in the materials formed during the steel-making process can play an indirect but important role by trapping detrimental and beneficial impurities or by promoting crack initiation at surfaces in contact with water.

Acknowledgments

The authors thank W. F. Burke, T. M. Galvin, and J. Franklin for their contributions to the experimental effort. The authors are grateful to L. James and D. Jones of Bettis Atomic Power Laboratory, Pittsburgh, PA, for providing the A302–GrB steel, and to J. R. Crum of INCO Alloys International, Huntington, WV; A. McIlree of the Electric Power Research Institute, Palo Alto, CA; and C. M. Blanchard of the EPRI NDE Center, Charlotte, NC, for supplying heats of Alloys 600 and 690 for this investigation. This work is sponsored by the Office of Nuclear Regulatory Research, U.S. Nuclear Regulatory Commission, under FIN Number A2212; Program Manager: Dr. M. B. McNeil.

1 Introduction

Fatigue and environmentally assisted cracking (EAC) of piping, pressure vessels, and core components in light water reactors (LWRs) are important concerns in operating plants and for extended reactor lifetimes. The degradation processes in U.S. reactors include fatigue of austenitic stainless steel (SS) in emergency core cooling systems* and pressurizer surge line** piping in pressurized water reactors (PWRs), intergranular stress corrosion cracking (IGSCC) of austenitic SS piping in boiling water reactors (BWRs), and propagation of fatigue or stress corrosion cracks (which initiate in sensitized SS cladding) in low-alloy ferritic steels in BWR pressure vessels.*** Similar cracking has also occurred in upper-shell-to-transition-cone girth welds in PWR steam generator vessels,+ and cracks have been found in steam generator feedwater distribution piping.++ Occurrences of mechanical-vibration- and thermal-fluctuation-induced fatigue failures in LWR plants in Japan have also been documented.[1]

Another concern is failure of reactor-core internal components after accumulation of relatively high fluence. The general pattern of the observed failures indicates that as nuclear plants age and neutron fluence increases, many apparently nonsensitized austenitic materials become susceptible to intergranular failure by a degradation process commonly known as irradiation-assisted stress corrosion cracking (IASCC). Some of these failures have been reported for components subjected to relatively low or negligible stress levels, e.g., control-blade sheaths and handles and instrument dry tubes of BWRs. Although most failed components can be replaced, some safety-significant structural components, such as the BWR top guide,+++ core plate,+++ and shroud,¶ would be very difficult or impracticai to replace. Research during the past six months has focused on fatigue of ferritic steels used in piping, steam generators, and pressure vessels; EAC of wrought austenitic SSs and Alloy 600; and IASCC in high- and commercial-purity (HP and CP) Type 304 SS specimens from control-blade absorber tubes and a control-blade sheath used in operating BWRs.

2 Fatigue of Ferritic Steels (O. K. Chopra, D. J. Gavenda, and W. J. Shack)

Plain carbon and low-alloy steels are used extensively in PWR and BWR steam supply systems as piping and pressure-vessel materials. The ASME Boiler and Pressure Vessel Code Section III,[2] Subsection NB, which contains rules for the construction of Class 1 components for nuclear power plants, recognizes fatigue as a possible mode of failure in pressure vessel steels and piping materials. Figure I-90 of Appendix I to Section III of the ASME Code specifies fatigue design curves for applicable structural materials. However, Section III, Subsection NB-3121, of the Code states that environmental effects on fatigue resistance of the material are

*USNRC Information Bulletin No. 88-08, "Thermal Stresses in Piping Connected to Reactor Coolant Systems," June 1988; Supplement 1, June 1988; Supplement 2, August 1988; Supplement 3, April 1989.

**USNRC Information Bulletin No. 88-11, "Pressurizer Surge Line Thermal Stratification," December 1988.

***USNRC Information Notice No. 90-29, "Cracking of Cladding in Its Heat-Affected Zone in the Base Metal of a Reactor Vessel Head," April 1990.

+USNRC Information Notice No. 90-04, "Cracking of the Upper Shell-to-Transition Cone Girth Welds in Steam Generators," January 1990.

++USNRC Information Notice No. 91-19, "Steam Generator Feedwater Distribution Piping Damage," March 1991; Notice No. 93-20, "Thermal Fatigue Cracking of Feedwater Piping to Steam Generators," March 1993.

+++USNRC Information Notice No. 95-17, "Reactor Vessel Top Guide and Core Plate Cracking," March 1995.

¶USNRC Information Notice No. 94-42, "Cracking in the Lower Region of the Core in Boiling-Water Reactors," June 1994; Notice No. 93-79, "Core Shroud Cracking at Beltline Region Welds in Boiling-Water Reactors," September 1993.

not explicitly addressed in the design fatigue curves. Therefore, effects of environment on fatigue resistance of materials in all operating PWR and BWR plants whose primary-coolant pressure boundary components are constructed to the specification of Section III of the Code are somewhat uncertain.

Recent fatigue strain vs. life (S–N) data from the U.S.[3–17] and Japan[18–23] illustrate potentially significant effects of LWR environments on the fatigue resistance of carbon and low-alloy steels. The results indicate only a marginal effect of low-dissolved-oxygen (DO) PWR environment on fatigue life (fatigue life is lower by a factor of <2 than in air). Environmental effects on fatigue life are significant when five conditions are satisfied simultaneously, viz., applied strain range is above a minimum threshold level, strain rate <1%/s, temperature ≥150°C, DO ≥0.05 ppm, and sulfur content in steel >0.003 wt.%. Under certain conditions of loading and environment, fatigue lives in water can be a factor of 100 shorter than those in air. Based on existing fatigue S–N data, we have developed interim fatigue design curves that take into account temperature, DO concentration in water, sulfur level in steel, and strain rate.[24] Statistical models have also been developed for estimating the effects of various material and loading conditions on fatigue life of materials used in the construction of nuclear power plant components.[25,26] Results of the statistical analysis have been used to estimate the probability of fatigue cracking in reactor components.

The objectives of our task are to conduct fatigue tests on carbon and low-alloy steels under conditions where information is lacking in the existing S–N data base, establish the effects of material and loading variables on fatigue life, and validate and update the proposed interim fatigue design curves. Fatigue tests are being conducted on carbon and low-alloy steels in air and water environments. During the present reporting period, several exploratory tests were conducted in which a slow strain rate is applied during only a portion of the tensile-loading cycle to check whether each portion of the tensile cycle is equally effective in decreasing fatigue life in high-DO water. Fatigue tests were also conducted to establish the effects of room-temperature water and of material orientation on fatigue life of carbon and low-alloy steels. Results from these tests are presented and experimental data are compared with estimates based on the statistical model.

2.1 Experimental

Low-cycle fatigue tests are being conducted on A106-Gr B and A333-Gr 6 carbon steel and A533-Gr B and A302-Gr B low-alloy steel with MTS closed-loop electrohydraulics machines. The A106-Gr B material was obtained from a 508-mm-diam., schedule 140 pipe fabricated by the Cameron Iron Works, Houston, TX. The A333-Gr 6 material was supplied by the Ishikawajima-Harima Heavy Industries Co. (IHI) of Japan. It was obtained from a 436-mm-diam. x 36-mm-wall pipe fabricated by Sumitomo Metal Industries, Ltd. The A533-Gr B material was obtained from the lower head of the Midland reactor vessel, which was scrapped before the plant was completed. The A302-Gr B low-alloy steel had been used in a previous study of the effect of temperature and cyclic frequency on fatigue crack growth behavior in a high-temperature aqueous environment at the Bettis Atomic Power Laboratory.[27,28] The material showed increased crack growth rates (CGRs) in simulated PWR water at 243°C. The chemical compositions and heat treatments of the materials are given in Table 1, and the average room-temperature tensile properties are given in Table 2. The microstructure of carbon steels consists of pearlite and ferrite, whereas the low-alloy steels contain tempered

bainite plus ferrite. The morphology of sulfides along three orientations, e.g., rolling (R), transverse (T), and radial (T2) directions,† for A302–Gr B low–alloy steel differ significantly.[14]

Table 1. Chemical composition (wt.%) of ferritic steels for fatigue tests

Material	Source	Chemical Composition							
		C	P	S	Si	Cr	Ni	Mn	Mo
					Carbon Steel				
A106–B[a]	ANL	0.29	0.013	0.015	0.25	0.19	0.09	0.88	0.05
	Supplier	0.29	0.016	0.015	0.24	–	–	0.93	–
A106–B	Terrell	0.26	0.008	0.020	0.28	0.015	0.002	0.92	0.003
A333–6	Higuchi	0.20	0.020	0.015	0.31	–	–	0.93	–
A333–6[b]	EFD	0.21	0.016	0.012	0.31	–	–	1.14	–
					Low–Alloy Steel				
A533–B[c]	ANL	0.22	0.010	0.012	0.19	0.18	0.51	1.30	0.48
	Supplier	0.20	0.014	0.016	0.17	0.19	0.50	1.28	0.47
A533–B	JNUFAD	0.19	0.020	0.010	0.27	0.13	0.60	1.45	0.52
A302–B[d]	Bettis	0.19	0.015	0.027	0.21	–	–	1.17	0.48
	Supplier	0.21	0.021	0.027	0.22	0.14	0.23	1.34	0.51

[a]508–mm O.D. schedule 140 pipe fabricated by Cameron Iron Works, Heat J–7201. Actual heat treatment not known.
[b]436–mm O.D. 36–mm wall pipe fabricated by Sumitomo Metal Industries, Ltd. Austenitized at 900°C for 1/2 h and air cooled.
[c]162–mm–thick hot–pressed plate from Midland reactor lower head. Austenitized at 871–899°C for 5.5 h and brine quenched and then tempered at 649–663°C for 5.5 h and brine quenched. The plate was machined to a final thickness of 127 mm. The I.D. surface was inlaid with 4.8–mm weld cladding and stress relieved at 607°C for 23.8 h.
[d]102–mm thick plate. Austenitized at 899–927°C for 4 h, water quenched to 538°C and air cooled, tempered at 649–677°C, then stress relieved at 621–649°C for 6 h (6 cycles).

Table 2. Average room–temperature tensile properties of the steels

Material	Reference[a]	Yield Stress (MPa)	Ultimate Stress (MPa)	Elongation (%)	Reduction in Area (%)
		Carbon Steel			
A106–B	ANL	301	572	23.5	44.0
A106–B	Terrell (7,8)	300	523	36.3	66.3
A333–6	Higuchi (18)	302	489	41.0	80.0
A333–6	Higuchi (21)	383	549	35.0	–
		Low–Alloy Steel			
A533–B	ANL	431	602	27.8	66.6
A533–B	JNUFAD	488	630	27.7	65.2
A302–B	Bettis (29)	389	552	–	–

[a]Reference number given within parentheses.

Smooth cylindrical specimens with 9.5–mm diameter and 19–mm gage length were used for the fatigue tests. The A302–Gr B specimens were machined from a composite bar fabricated by electron–beam welding two 19.8–mm diameter, 137–mm long bars of A533–Gr B

†The three orientations are represented by the direction that is perpendicular to the fracture plane. Both transverse and radial directions are perpendicular to the rolling direction but the fracture plane is across the thickness of the plate in transverse orientation and parallel to the plate surface in radial orientation.

steel on each side of a 18.8–mm diameter, 56–mm long section of A302–Gr B steel. Thus, the gauge length and shoulders of the specimen were A302–Gr B and the grip region was A533–Gr B steel. After welding, the composite bars were stress relieved at 650°C for 6 h. The gage length of all specimens was given a 1–μm surface finish in the axial direction to prevent circumferential scratches that might act as sites for crack initiation. Unless stated otherwise, all tests were conducted at 288°C with fully reversed axial loading (i.e., strain ratio R = –1) and a triangular or sawtooth waveform. The strain rate for the triangular wave and fast–loading half of the sawtooth wave was 0.4%/s.

A small autoclave with an annular volume of 12 mL was used for fatigue tests in water. Descriptions of the test facility and procedure are given in Ref. 12. Tests in water were performed under stroke control where the specimen strain was controlled between two locations outside the autoclave. Tests in air were performed under strain control with an axial extensometer; specimen displacement between the two locations used in the water tests was also recorded. Information from the air tests was used to determine the stroke required to maintain constant strain in the specimen gage length for tests in water; the stroke is gradually increased during the test to account for cyclic hardening of the material and to maintain constant strain in the specimen gage section. Accuracy of the procedure was checked with stroke–controlled tests in air where strain in the gage section of the specimen was monitored.

Figure 1 shows the loading strain that is actually applied to the specimen gage section (solid line) during a stroke–controlled tests with a sawtooth waveform (dashed line). During the cycle, the fraction of applied displacement that goes to the specimen gage section is not constant but varies with the loading strain. Consequently, the loading rate also varies during the fatigue cycle; it is lower than the applied strain rate at strain levels below the elastic limit and higher at larger strains.

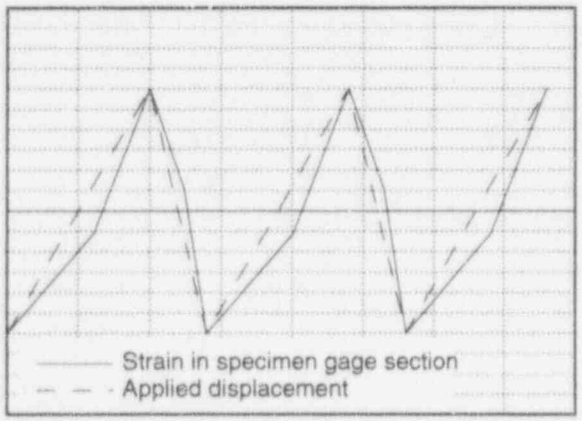

Figure 1.
Waveforms for applied displacement (dashed line) and strain in specimen gage section (solid line) during stroke–controlled test

2.2 Air Environment

Fatigue results on A106–Gr B and A533–Gr B steels in air and water environments at 288°C were presented in Ref. 15 and are summarized in Tables 3 and 4. Fatigue S–N curves for the two steels in air are shown in Fig. 2. Fatigue life is defined as the number of cycles N_{25} for tensile stress to drop 25% from its peak value; this corresponds to a ≈3–mm deep crack in the test specimen. Results from other investigations[7,18] on similar steels with comparable composition and the ASME Section III mean–data curve at room temperature are also included in the figures.

Table 3. Fatigue test results for A106–Gr B carbon steel at 288°C

Test Number	Environ -ment[a]	Dissolved Oxygen[b] (ppb)	pH at RT	Conducti- vity (μS/cm)	Tensile Rate (%/s)	Comp. Rate (%/s)	Stress Range (MPa)	Strain Range (%)	Life N_{25} (Cycles)
1498	Air	–	–	–	0.4	0.4	1001.4	1.004	1,048
1546	Air	–	–	–	0.4	0.4	975.7	0.916	1,365
1553	Air	–	–	–	0.4	0.4	921.1	0.757	3,253
1554	Air	–	–	–	0.4	0.4	896.8	0.730	3,753
1674[c]	Air	–	–	–	0.4	0.4	1003.6	0.764	6,275
1686[c]	Air	–	–	–	0.4	0.4	1017.2	0.804	2,592
1731	Air	–	–	–	0.4	0.004	1005.5	0.758	3,485
1615	Air	–	–	–	0.04	0.4	959.8	0.755	3,873
1609	Air	–	–	–	0.004	0.4	1026.0	0.756	3,721
1612	Air	–	–	–	0.004	0.4	1008.2	0.779	3,424
1673	Air	–	–	–	0.004	0.4	1003.6	0.759	6,275
1548	Air	–	–	–	0.4	0.4	831.9	0.545	10,632
1543	Air	–	–	–	0.4	0.4	818.2	0.502	14,525
1619	Air	–	–	–	0.4	0.4	741.7	0.401	37,142
1636[d]	Air	–	–	–	0.4	0.4	749.6	0.402	34,829
1621	Air	–	–	–	0.01	0.4	787.1	0.403	38,128
1638[e]	Air	–	–	–	0.4	0.4	800.0	0.436	26,728
1550	Air	–	–	–	0.4	0.4	681.7	0.353	66,768
1552	Air	–	–	–	0.4	0.4	680.6	0.352	93,322
1555	Air	–	–	–	0.4	0.4	676.3	0.343	98,456
1644	Air	–	–	–	0.004	0.4	702.0	0.364	>94,657
1738[f]	DI	1	6.5	0.09	0.004	0.4	976.2	0.777	1,350
1744[f]	DI	<1	6.5	0.08	0.4	0.4	760.5	0.414	19,860
1547	PWR	8	6.7	23.26	0.4	0.4	1010.9	0.987	692
1564	PWR	12	6.6	21.74	0.4	0.4	942.0	0.769	1,525
1676	PWR	2	6.5	20.83	0.4	0.4	926.7	0.741	2,230
1679	PWR	3	6.5	20.41	0.004	0.4	1005.8	0.763	2,141
1681	PWR	1	6.5	20.00	0.0004	0.4	1015.7	0.764	2,672
1549	PWR	8	6.7	25.64	0.4	0.4	827.0	0.533	9,396
1560	PWR	12	6.6	23.73	0.4	0.4	701.3	0.363	35,190
1556	PWR	8	6.6	22.73	0.4	0.4	710.9	0.360	38,632
1632	Hi DO	800	5.8	0.11	0.4	0.4	913.3	0.740	2,077
1705	Hi DO	650	5.9	0.15	0.4	0.4	947.9	0.767	1,756
1680[c]	Hi DO	700	6.0	0.08	0.4	0.4	999.6	0.818	1,007
1690[c]	Hi DO	700	6.0	0.08	0.4	0.4	1002.2	0.824	1,092
1687[g]	Hi DO	700	6.0	0.10	0.4	0.4	1020.0	0.809	840
1757	Hi DO	670	5.9	0.07	0.4	0.004	942.2	0.742	1,195
1693	Hi DO	650	6.0	0.10	0.04	0.4	920.0	0.737	1,125
1614	Hi DO	400	5.9	0.11	0.004	0.4	930.4	0.786	303
1682	Hi DO	700	6.0	0.09	0.004	0.4	921.1	0.746	469
1623	Hi DO	800	5.9	0.08	0.004	0.004	943.8	0.792	338
1616	Hi DO	800	5.8	0.08	0.0004	0.4	912.8	0.799	153
1620	Hi DO	900	5.9	0.11	0.00004	0.004	943.1	0.794	161
1706	Hi DO	600	5.9	0.07	0.4	0.4	825.2	0.528	7,858
1634	Hi DO	800	5.8	0.16	0.4	0.4	733.2	0.400	19,318
1637[e]	Hi DO	900	5.9	0.11	0.4	0.4	788.3	0.470	16,622
1624	Hi DO	800	5.9	0.10	0.004	0.4	775.7	0.456	2,276
1639	Hi DO	800	5.9	0.09	0.004	0.4	751.6	0.418	2,951
1643	Hi DO	800	6.0	0.11	0.004	0.4	698.5	0.363	>65,000

[a]DI = Deionized water and PWR = simulated PWR water with 2 ppm lithium and 1000 ppm boron.
[b]Represent DO levels in effluent water. DO levels in supply water were 150–350 ppb higher.
[c]Tested with 5–min hold period at peak tensile strain.
[d]Specimen preoxidized at 288°C in water with 600 ppb DO for 100 h.
[e]Prior to the test, specimen was fatigued for 570 cycles in high–DO water with sawtooth waveform.
[f]Prior to being tested in low–DO water, specimen preoxidized in water with 600 ppb DO for 30 h.
[g]Tested with 30–min hold period at peak tensile strain.

Table 4. Fatigue test results for A533–Gr B low–alloy steel at 288°C

Test Number	Environ –ment[a]	Dissolved Oxygen[b] (ppb)	pH at RT	Conducti– vity (μS/cm)	Tensile Rate (%/s)	Comp. Rate (%/s)	Stress Range (MPa)	Strain Range (%)	Life N_{25} (Cycles)
1508	Air	–	–	–	0.4	0.4	910.9	1.002	3,305
1524	Air	–	–	–	0.4	0.4	892.3	0.950	3,714
1523	Air	–	–	–	0.4	0.4	898.6	0.917	2,206
1521	Air	–	–	–	0.4	0.4	889.4	0.910	3,219
1522	Air	–	–	–	0.4	0.4	905.4	0.899	3,398
1515	Air	–	–	–	0.4	0.4	866.1	0.752	6,792
1749[c]	Air	–	–	–	0.4	0.4			6,372
1717	Air	–	–	–	0.4	0.004	884.6	0.758	6,217
1625	Air	–	–	–	0.004	0.4	887.7	0.757	4,592
1629[d]	Air	–	–	–	0.4	0.4	782.9	0.503	31,243
1590	Air	–	–	–	0.4	0.004	821.1	0.503	24,471
1576	Air	–	–	–	0.004	0.4	805.8	0.503	28,129
1505	Air	–	–	–	0.4	0.4	767.6	0.501	31,200
1525	Air	–	–	–	0.4	0.4	743.6	0.452	65,758
1640	Air	–	–	–	0.4	0.4	710.9	0.402	65,880
1538	Air	–	–	–	0.4	0.4	708.0	0.387	>1,000,000
1517	Air	–	–	–	0.4	0.4	692.5	0.353	2,053,295
1659	Air	–	–	–	0.004	0.4	656.2	0.343	>114,294
1526	DI	–	–	–	0.4	0.4	876.4	0.873	3,332
1527	DI	–	6.0	–	0.4	0.4	752.8	0.493	10,292
1528	DI	5	5.8	–	0.4	0.4	744.1	0.488	25,815
1743[e]	DI	<1	6.5	0.08	0.4	0.4	712.6	0.386	84,700
1530	PWR	3	6.9	41.67	0.4	0.4	885.5	0.894	1,355
1545	PWR	8	6.9	22.73	0.4	0.4	889.7	0.886	3,273
1533	PWR	4	6.9	45.45	0.004	0.4	916.0	0.774	3,416
1529	PWR	3	6.9	45.45	0.4	0.4	743.4	0.484	31,676
1605	PWR	9	6.5	23.81	0.4	0.004	785.2	0.460	>57,443
1588	PWR	6	6.5	23.26	0.004	0.4	828.7	0.514	15,321
1539	PWR	6	6.8	38.46	0.4	0.4	690.9	0.373	136,570
1542	PWR	6	6.6	27.03	0.4	0.4	631.8	0.354	>1,154,892
1645	Hi DO	800	6.1	0.07	0.4	0.4	831.1	0.721	2,736
1768	Hi DO	600	6.0	0.07	0.4	0.004	907.3	0.755	1,350
1626	Hi DO	900	5.9	0.13	0.004	0.4	910.1	0.788	247
1715	Hi DO	600	5.9	0.08	0.004	0.4	904.1	0.813	381
1711	Hi DO	630	5.8	0.31	0.4	0.4	772.1	0.542	5,850
1707	Hi DO	650	5.9	0.08	0.4	0.004	803.0	0.488	3,942
1709	Hi DO	650	5.9	0.11	0.4	0.004	805.1	0.501	3,510
1627	Hi DO	800	5.9	0.10	0.004	0.4	826.8	0.534	769
1641	Hi DO	800	5.9	0.09	0.4	0.4	693.0	0.385	17,367
1665	Hi DO	800	6.1	0.08	0.004	0.4	717.0	0.376	3,455
1666	Hi DO	750	6.1	0.09	0.0004	0.4	729.6	0.376	>7,380
1647	Hi DO	800	6.1	0.09	0.4	0.4	688.0	0.380	26,165
1660	Hi DO	750	6.1	0.11	0.004	0.4	689.6	0.360	>83,024
1649	Hi DO	700	6.3	0.08	0.4	0.4	673.4	0.352	28,710
1652	Hi DO	700	6.1	0.09	0.4	0.4	638.1	0.328	56,923
1655	Hi DO	750	6.1	0.10	0.4	0.4	567.6	0.289	>1,673,954

[a]DI = Deionized water and PWR = simulated PWR water containing 2 ppm lithium and 1000 ppm boron.
[b]Represent DO levels in effluent water. DO levels in supply water were 150–350 ppb higher.
[c]Tested with 5–min hold period at peak tensile strain.
[d]Specimen preoxidized in water with 600 ppb DO for 100 h at 288°C.
[e]Specimen preoxidized in water with 600 ppb DO for 30 h at 288°C.

The results indicate that fatigue life of low–alloy steels is greater than that of carbon steel. Strain rate has little or no effect on fatigue life of both A106–Gr B and A533–Gr B steels in air. The data for A106–Gr B steel are in good agreement with results obtained by Terrell[7] on A106–Gr B steel, but are lower by a factor of ≈5 than those obtained by Higuchi and Iida[18] on A333–

Gr 6 steel. Also, the data for A106–Gr B steel are below the ASME mean curve for carbon steel at high strain ranges (by a factor of 3). The results for A533–Gr B steel show good agreement with the ASME mean–data curve for low–alloy steel at room temperature and JNUFAD* data on A533–Gr B steel.

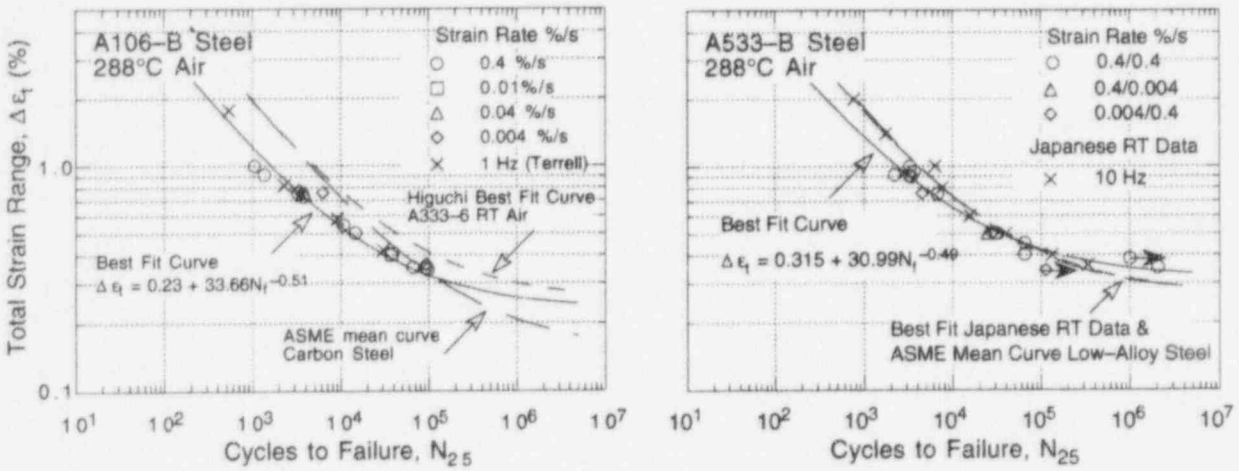

Figure 2. Total strain range vs. fatigue life data for A106–Gr B carbon steel and A533–Gr B low–alloy steel in air

Statistical models have been developed at ANL to estimate fatigue lives of carbon and low–alloy steels in air and LWR environments.[26,27] The fatigue life N_{25} of carbon steels is expressed as

$$\ln(N_{25}) = (6.570 - 0.384\, I_W) - 1.871 \ln(\varepsilon_a - 0.11) - 0.00133\, T\,(1 - I_W) + 0.554\, S^*\, T^*\, O^*\, \dot{\varepsilon}^*, \quad (1)$$

and that of low–alloy steels as

$$\ln(N_{25}) = (6.667 - 0.766\, I_W) - 1.687 \ln(\varepsilon_a - 0.15) - 0.00133\, T\,(1 - I_W) + 0.554\, S^*\, T^*\, O^*\, \dot{\varepsilon}^*, \quad (2)$$

where

ε_a = the applied strain amplitude in %,
T = the test temperature in °C,
I_W = 1 for water and 0 for air environment, and

S^*, T^*, O^*, and $\dot{\varepsilon}^*$ = transformed sulfur content, temperature, DO, and strain rate, respectively, defined as follows:

$S^* = S$ (0 < S ≤ 0.015 wt.%)
$S^* = 0.01$ (S >0.015 wt.%) (3a)

$T^* = 0$ (T <150°C)
$T^* = T - 150$ (T = 150–350°C) (3b)

$O^* = 0$ (DO <0.05 ppm)
$O^* = DO$ (0.05 ppm ≤DO ≤0.5 ppm)
$O^* = 0.5$ (DO >0.5 ppm) (3c)

$\dot{\varepsilon}^* = 0$ ($\dot{\varepsilon}$ >1 %/s)
$\dot{\varepsilon}^* = \ln(\dot{\varepsilon})$ (0.001 ≤$\dot{\varepsilon}$ ≤1 %/s)
$\dot{\varepsilon}^* = \ln(0.001)$ ($\dot{\varepsilon}$ <0.001 %/s) (3d)

*Private communication from M. Higuchi, Ishikawajima–Harima Heavy Industries Co., Japan, to M. Prager of the Pressure Vessel Research Council, 1992.

The fatigue lives of carbon and low-alloy steels in air at 288°C (Fig. 3) are compared with values estimated from Eqs. 1 and 2. Predicted fatigue lives show good agreement with the experimental results. The statistical model was based on 23 heats of carbon and low-alloy steels. The results indicate that A533- Gr B steel exhibits an average behavior, whereas the fatigue S-N curve for A106-Gr B steel is slightly lower than the average for carbon steels.

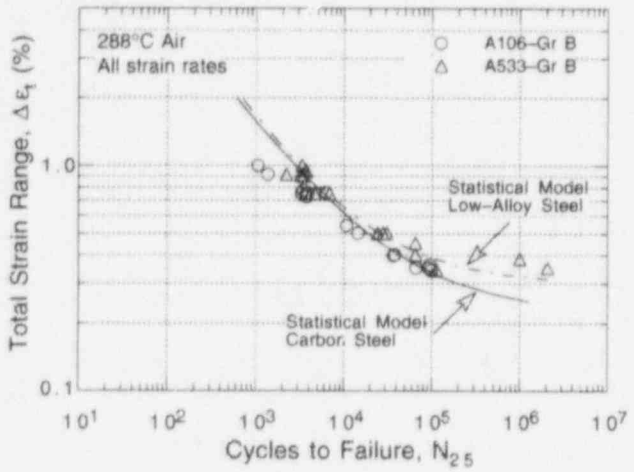

Figure 3.
Experimental and predicted fatigue lives of carbon steel and low-alloy steels in air at 288°C

2.3 LWR Environments

The fatigue data in LWR environments indicate only a marginal effect of low-DO PWR water on fatigue life of carbon and low-alloy steels. Fatigue lives of both steels in PWR water are lower than those in air by a factor of <2. A decrease in strain rate by three orders of magnitude does not cause an additional decrease in fatigue life of A106-Gr B and A533-Gr B steels. The results for A106-Gr B steel are consistent with data obtained by Terrell[8,9] in simulated PWR water where little or no effect of strain rate or environment on fatigue life was observed.

Environmental effects on fatigue life are significant at high DO levels, e.g., 0.5-0.8 ppm. Although the microstructures and cyclic-hardening behavior of A106-Gr B carbon steel and A533-Gr B low-alloy steel are differ significantly, there is little or no difference in environmental degradation of fatigue life of these steels. A minimum strain is required for environmentally assisted decrease in fatigue life. For the loading conditions in the present study, this threshold strain range appears to be ≈0.36% for the heats of carbon and low-alloy steels investigated. Fatigue life of carbon and low-alloy steels decreases rapidly with decreasing strain rate. For both steels, the effect of strain rate saturates at ≈0.001%/s. The results also indicate that a slow strain rate applied during the tensile-loading cycle is more effective in environmentally assisted reduction in fatigue life than when applied during the compressive-loading cycle. A slow strain rate applied during both the compressive- and the tensile-loading cycles does not cause further decrease in fatigue life.

The experimental values of fatigue life of A106-Gr B carbon steel and A533-Gr B low-alloy steel in PWR and high-DO water at 288°C and those predicted from Eqs. 1 and 2 are plotted in Figs. 4 and 5, respectively. For the various material, loading, and environmental conditions, the predicted fatigue lives are in good agreement with the experimental results.

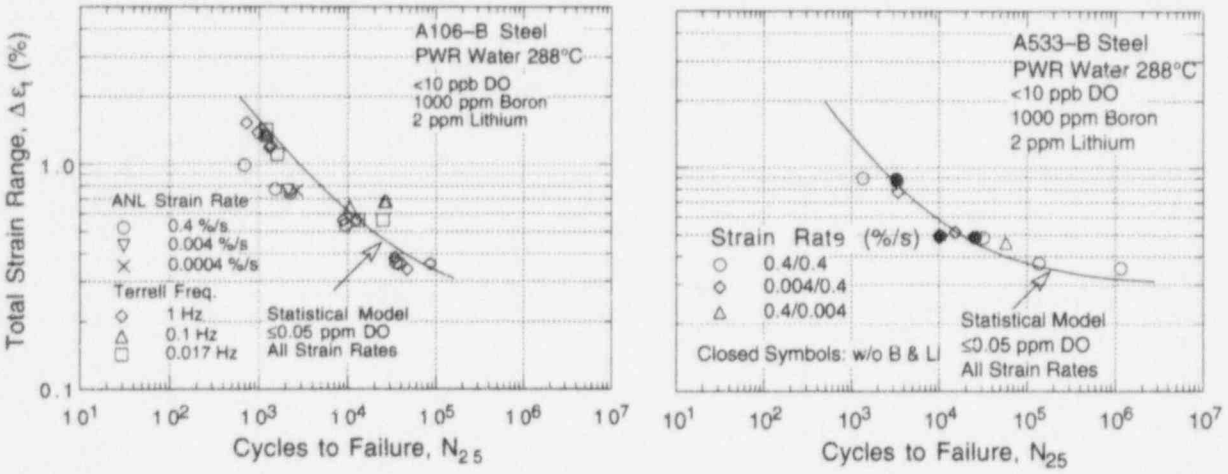

Figure 4. Fatigue S–N behavior for A106–Gr B and A533–Gr B steels estimated from the model and determined experimentally in PWR water at 288°C

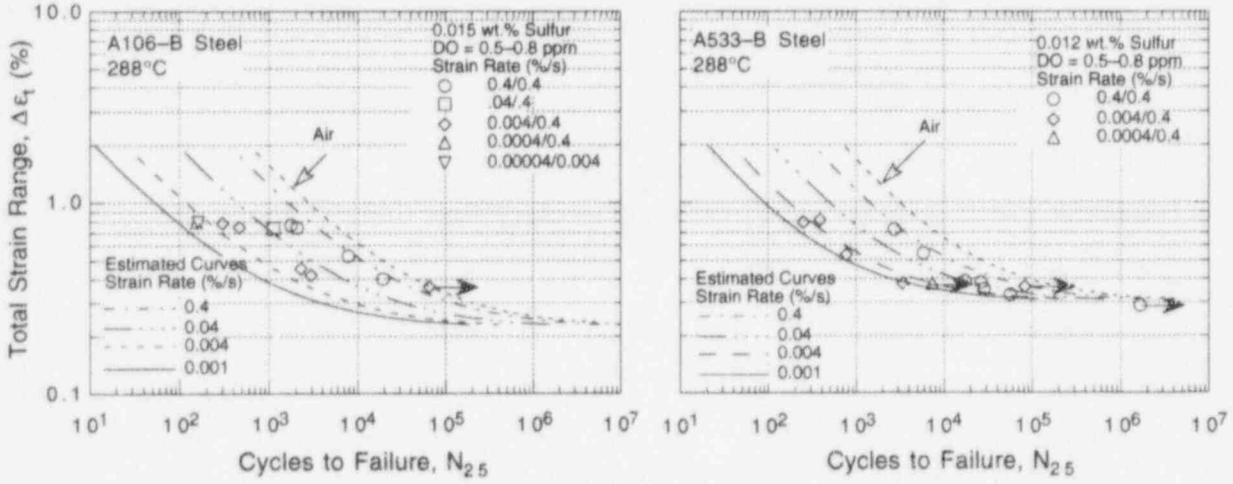

Figure 5. Fatigue S–N behavior for A106–Gr B and A533–Gr B steels estimated from the model and determined experimentally in high–DO water at 288°C

2.4 Room–Temperature Water

Fatigue tests were conducted on A106–Gr B and A533–Gr B steels in air and water environments at room temperature to study the possible effect of test temperature. The results are listed in Table 5; the fatigue S–N plots are shown in Fig. 6. At room temperature, life in water is 30–50% lower than in air. Estimates based on Eqs. 1 and 2 are also shown in Fig. 6; the results show good agreement with the experimental data.

The cyclic–hardening behaviors of the steels are significantly different at room temperature than at 288°C. Plots of cyclic stress range vs. fatigue cycles for A106–Gr B and A533–Gr B steels tested in air at room temperature and 288°C, ≈0.75% strain range, and 0.4%/s strain rate, are shown in Fig. 7. The steels show little or no cyclic hardening at room temperature. In fact, the low–alloy steel exhibits cyclic softening. For both steels, the cyclic stress at half life is significantly lower at room temperature than at 288°C.

Table 5. Fatigue test results for A106–Gr B and A533–Gr B steels in air and water environments at room temperature

Test Number	Environment	Dissolved Oxygen[a] (ppb)	pH at RT	Conductivity (μS/cm)	Tensile Rate (%/s)	Comp. Rate (%/s)	Stress Range (MPa)	Strain Range (%)	Life N_{25} (Cycles)
A106–Gr B Steel									
1700	Air	–	–	–	0.4	0.4	715.2	0.756	6,574
1766	Air	–	–	–	0.4	0.4	719.7	0.757	7,120
1770	Air	–	–	–	0.4	0.4	608.5	0.403	37,379
1699	Hi DO	850	6.0	0.07	0.4	0.4	728.7	0.746	4,794
1772	Hi DO	750	6.2	0.07	0.4	0.4	618.7	0.399	23,300
A533–Gr B Steel									
1727	Air	–	–	–	0.4	0.4	766.7	0.758	9,145
1729	Air	–	–	–	0.4	0.4	677.5	0.405	77,759
1759	Hi DO	610	6.1	0.07	0.4	0.4	774.7	0.753	6,250
1761	Hi DO	770	6.1	0.08	0.4	0.4	694.5	0.399	46,500

[a]Represent DO levels in effluent water. DO levels in supply water were 150–350 ppb higher.

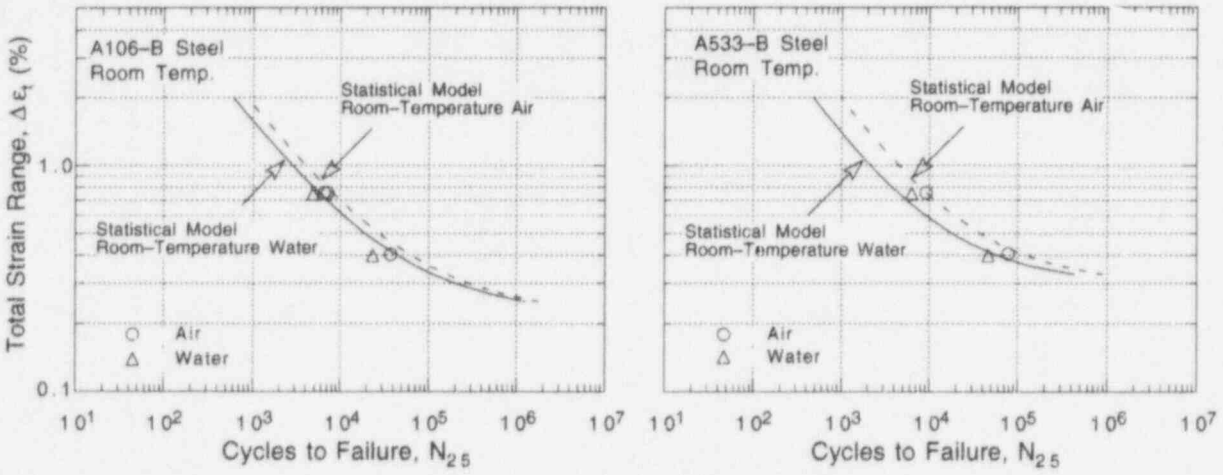

Figure 6. Experimental and predicted fatigue lives of A106–Gr B and A533–Gr B steels in air and water environments at room temperature

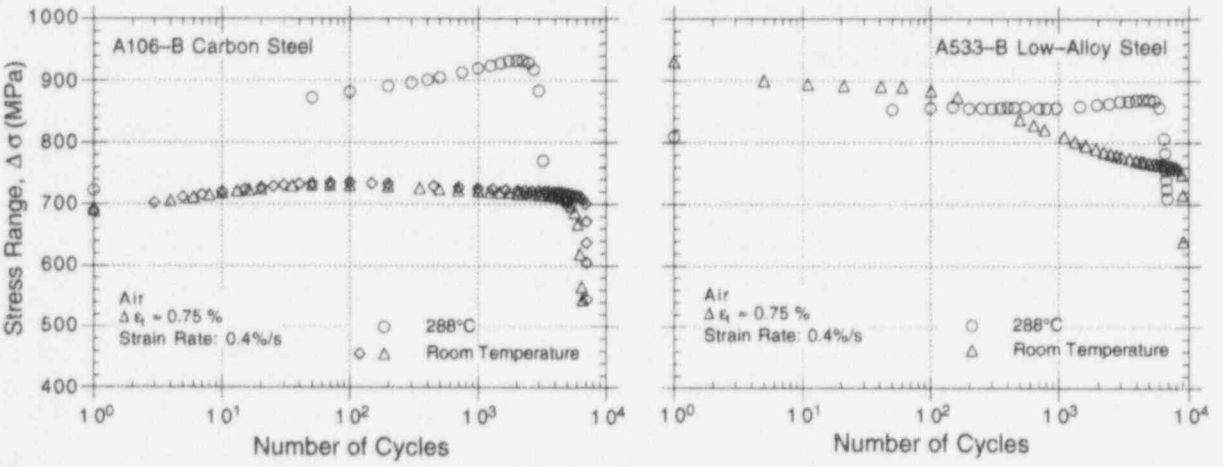

Figure 7. Effect of temperature on cyclic strain-hardening behavior of A106–Gr B and A533–Gr B steels in air at 0.75% strain range and 0.4%/s strain rate

Table 6. Fatigue test results for A302–Gr B low–alloy steel at 288°C

Test Number	Environment[a]	Dissolved Oxygen[b] (ppb)	pH at RT	Conductivity (μS/cm)	Tensile Rate (%/s)	Comp. Rate (%/s)	Stress Range (MPa)	Strain Range (%)	Life N_{25} (Cycles)
1697 (R)	Air	–	–	–	0.4	0.4	944.5	0.756	8,070
1701 (R)	Air	–	–	–	0.004	0.4	1021.4	0.757	4,936
1712 (R)	Air	–	–	–	0.0004[c]	0.4	1041.9	0.759	5,350
1789 (R)	Air	–	–	–	0.4	0.4	859.5	0.505	46,405
1783 (R)	Air	–	–	–	0.4	0.4	796.1	0.408	>1,050,000
1780 (T2)	Air	–	–	–	0.4	0.4	908.6	0.756	1,598
1781 (T2)	Air	–	–	–	0.004	0.4	952.4	0.755	375
1782 (T2)	Air	–	–	–	0.4	0.4	752.8	0.404	33,650
1787 (T2)	Air	–	–	–	0.4	0.4	667.5	0.342	431,150
1702 (R)	PWR	3	6.5	20.00	0.4	0.4	921.2	0.735	6,212
1704 (R)	PWR	3	6.5	19.23	0.004	0.4	1022.6	0.745	3,860
1716 (R)	PWR	5	6.5	19.23	0.0004[c]	0.4	1042.3	0.739	3,718
1777 (T)	PWR	1	6.4	19.23	0.4	0.4	913.8	0.765	4,366
1775 (T)	PWR	1	6.5	19.42	0.004	0.4	995.6	0.750	1,458
1776 (T2)	PWR	1	6.4	18.40	0.4	0.4	887.1	0.765	1,244
1774 (T2)	PWR	2	6.4	19.42	0.004	0.4	949.7	0.758	348
1788 (R)	Hi DO	650	5.9	0.10	0.004	0.4	957.0	0.754	317
1784 (T2)	Hi DO	510	6.0	0.07	0.004	0.4	937.6	0.783	111

[a]Simulated PWR water contains 2 ppm lithium and 1000 ppm boron.
[b]Represent DO levels in effluent water. DO levels in supply water were 150–350 ppb higher.
[c]Slow strain rate applied only during 1/8 cycle near peak tensile strain.

2.5 Material Orientation

Fatigue tests were conducted on A302–Gr B low–alloy steel in air and water to study the effects of orientation and strain rate on fatigue life of the steel and to verify whether current predictions of modest decreases of fatigue life in simulated PWR water are valid for high–sulfur heats that show enhanced CGRs in precracked specimens. Fatigue data for specimens in the rolling (R), transverse (T), and radial (T2) orientations are summarized in Table 6.

The results indicate strong effects of orientation, and also of strain rate. Note that the effect of strain rate was not observed for A106–Gr B carbon steel or A533–Gr B low–alloy steel. The material shows very poor fatigue properties in the transverse orientation; especially the orientation T2. Fatigue lives of A302–Gr B specimens oriented along the rolling (R) and radial (T2) directions are shown in Fig. 8. The endurance limit in the T2 orientation is lower than that in the R orientation. Also, fatigue life in the T2 orientation is nearly an order of magnitude lower than in the R orientation.

Fatigue lives for specimens with R and T2 orientations are compared with the fatigue S–N data for A533–Gr B steel in air and simulated PWR environments in Fig. 9. In both air and PWR environments, the fatigue lives for A302–Gr B steel in the rolling direction are in good agreement with data for A533–Gr B steel. The results indicate only a marginal effect of PWR water on fatigue life of A302–Gr B steel in either the R or T2 orientation. Fatigue life in PWR water is at most a factor of 1.3 lower than that in air. In PWR water, the effects of orientation and strain rate are similar to those in air. Relative to the R orientation, fatigue life of the steel in the T2 orientation is lower by factors of ≈5 and 12 at strain rates of 0.4 and 0.004%/s,

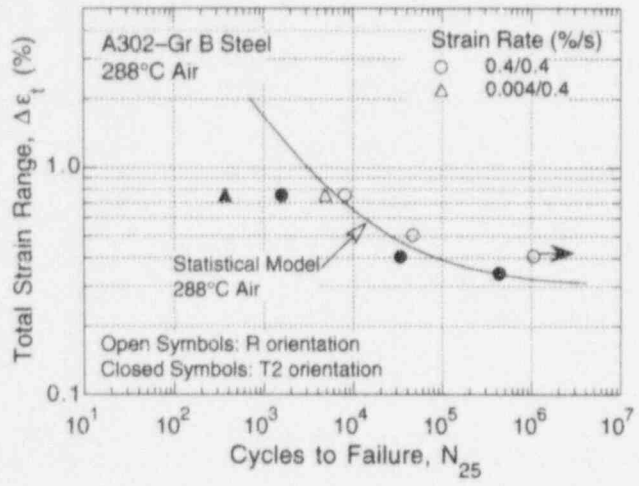

Figure 8.
Effect of material orientation on fatigue life of A302–Gr B low–alloy steel in air

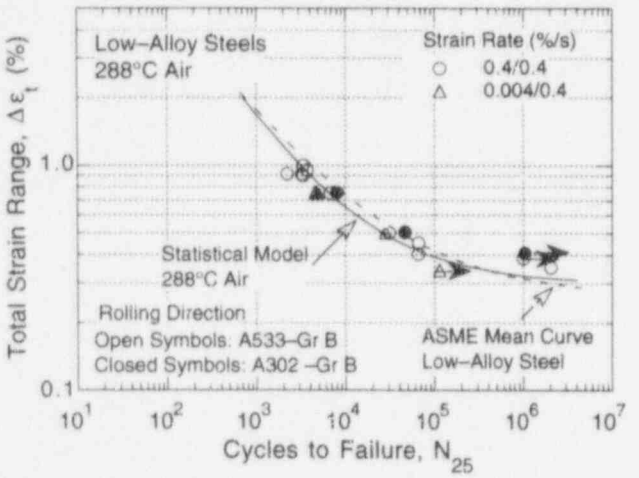

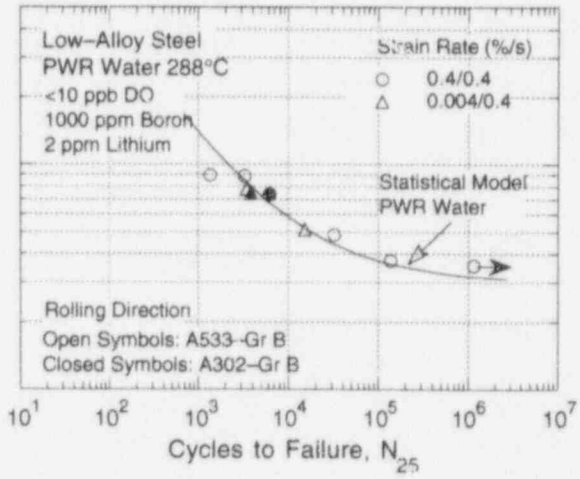

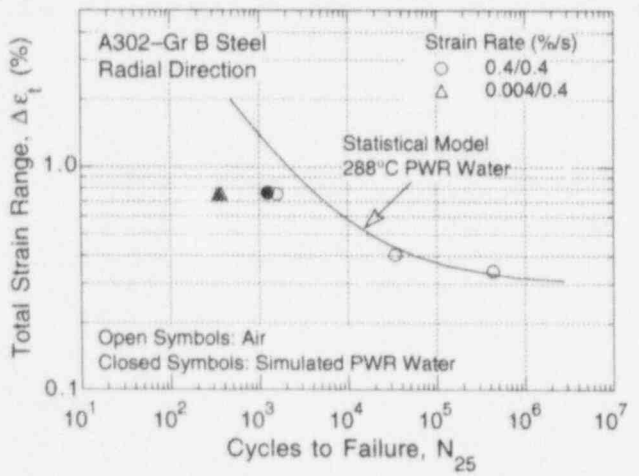

Figure 9.
Total strain range vs. fatigue life data for A302–Gr B and A533–Gr B low–alloy steels in air and simulated PWR environments at 288°C

respectively. Both in air and in PWR water, fatigue life decreases by at most a factor of ≈4 when strain rate decreases from 0.4 to 0.004%/s. The data suggest that even very–high–sulfur steels suffer only modest decreases of fatigue life in simulated PWR water.

In Fig. 10, the fatigue lives of A302–Gr B steel in high–DO water at 288°C are compared with data for A533–Gr B steel . The results indicate that the relative decrease in fatigue life in

high–DO water is not the same for all orientations. The decrease is small for steels with poor fatigue life in air (e.g., T2 orientation) and is large for steels that show good resistance to fatigue cracking in air (e.g., R orientation). While environmental effects on fatigue life are usually characterized in terms of a relative value compared to life in air, it appears that effects do saturate. The various heats of carbon and low–alloy steels listed in Table 1 (with 0.012–0.015 wt.% sulfur) all have a fatigue life of ≈350 cycles in water with >0.5 ppm DO at 288°C, a strain range of ≈0.75%, and a strain rate (in tension) of 0.004 %/s. However, decreases in life in water relative to those in air are ≈11 for A106–Gr B, ≈20 for A533–Gr B, ≈14 for A302–Gr B in the R orientation, and ≈2 for A302–Gr B in the T2 orientation.

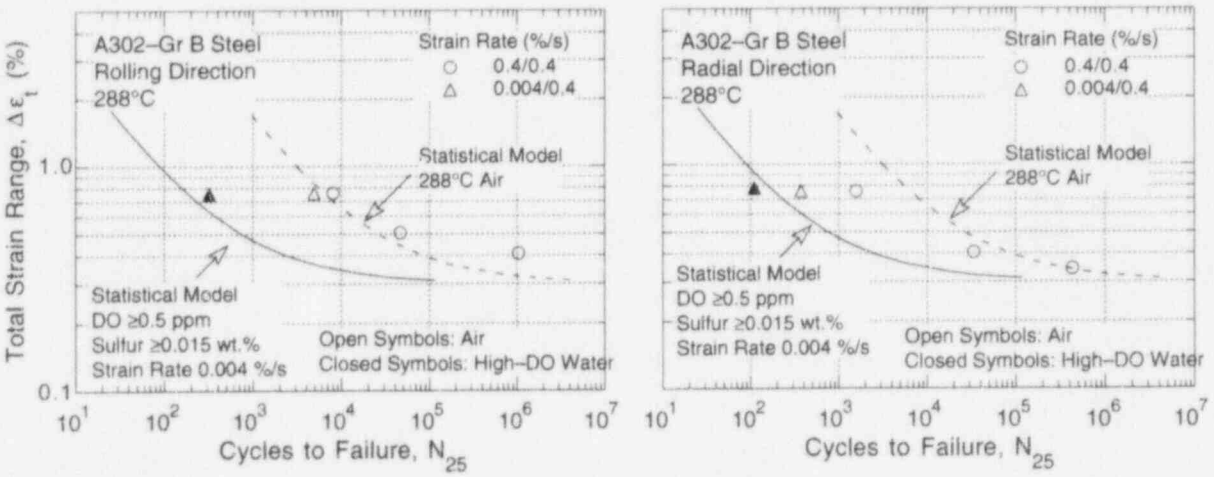

Figure 10. Total strain range vs. fatigue life data for A302–Gr B and A533–Gr B low–alloy steels in high–DO water at 288°C

Metallographic examination of the specimens indicates that structural factors are responsible for poor fatigue properties of transverse orientations. The fracture surface and longitudinal section of a A302–Gr B specimen in the T2 orientation tested in PWR water at 288°C, ≈0.75% strain range, and slow/fast waveform are shown in Fig. 11. The longitudinal section of the specimen shows an abundance of cracks that connect the sulfide stringers. These cracks are present through out the specimen away from the fracture surface. A fatigue crack propagates preferentially along these sulfide stringers; the fracture surface contains several fractured sulfide stringers.

2.6 Loading Waveform

Several exploratory tests were conducted on A106–Gr B and A533–Gr B steels in which a slow strain rate is applied during only a portion of the tensile–loading cycle to check whether each portion of the tensile cycle is equally effective in decreasing fatigue life in high–DO water. The results are presented in Table 7. The loading waveforms and corresponding fatigue lives for tests on A106–Gr B steel at ≈0.75% strain range are summarized in Fig. 12. The change in fatigue life of A106–Gr B and A533–Gr B steels with fraction of loading strain at slow strain rate is plotted in Fig. 13; results from tests conducted at IHI on the ANL heat of A106–Gr B steel are also included in the figure. Results are shown for slow portions applied near peak tensile strain (open symbols) or near peak compressive strain (closed symbols). In stroke–controlled tests, the fraction of loading strain that is actually applied to the specimen gage section is not constant but varies during the cycle. Consequently, for waveforms E and F,

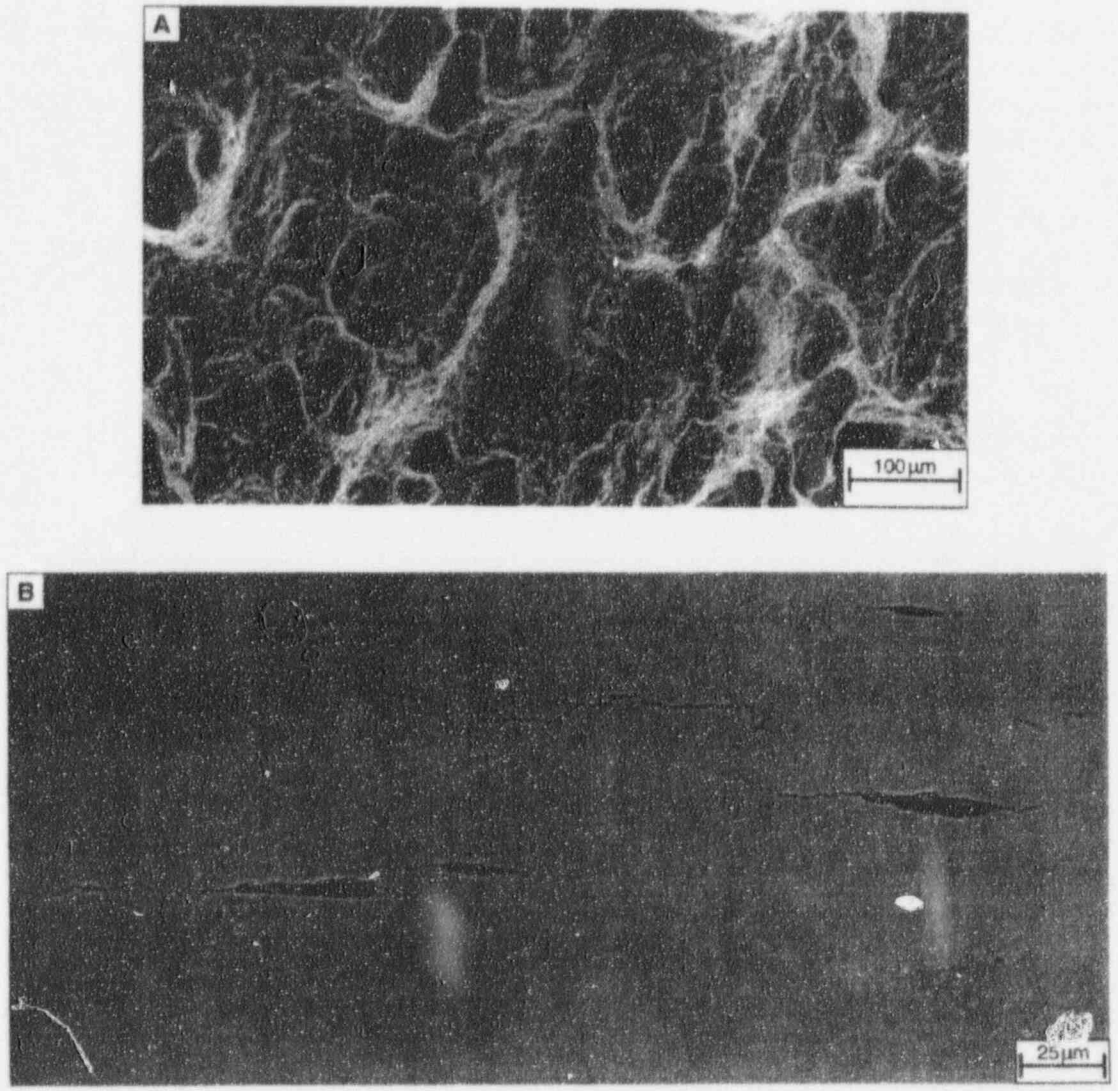

Figure 11. SEM photomicrograph of fracture surface (A) and longitudinal section (B) of A302-Gr B steel specimen in T2 orientation tested in PWR water at 288°C, ≈0.75% strain range, and slow/fast waveform

although 0.5 of the applied displacement is at a slow rate, the fractions of strain at slow rate in the specimen gage section are 0.666 and 0.334, respectively. The fraction of loading strain that is actually at a slow rate for the various waveforms is given in Table 7 and Fig. 12.

The results to date indicate that a slow strain rate applied during each portion of the loading cycle above the threshold strain is equally effective in decreasing fatigue life.[15-17] At 288°C and a strain range of ≈0.75%, the average fatigue life of A106-Gr B steel in air is ≈4000 cycles. Relative to air, the fatigue lives in simulated PWR water at all strain rates or in high-DO water at high strain rates (i.e., fast/fast tests) are lower by ≈50%. If each portion of the tensile-loading cycle was equally effective in reducing fatigue life, the life should decrease linearly from A to C along the chain-dot line in Fig. 13 and a slow strain rate near peak compressive strain (waveforms F, H, or K) should be as equally damaging as a slow strain rate near peak tensile strain (waveforms E, G, or H). The results show that a slow strain rate near peak compressive strain causes little or no reduction in fatigue life.

Table 7. Results of exploratory fatigue tests in which a slow strain rate is applied during only a portion of tensile-loading cycle

Test Number	Environment	Dissolved Oxygen[a] (ppb)	pH at RT	Conductivity (μS/cm)	Waveform[b]	Fraction of strain at slow rate	Stress Range (MPa)	Strain Range (%)	Life N_{25} (Cycles)
A106-Gr B Steel									
1760	Air	–	–	–	C	0.75	1042.8	0.756	3,893
1762	Air	–	–	–	D	0.75	1027.5	0.758	4,356
1667	Air	–	–	–	E	0.50	999.2	0.758	5,261
1668	Air	–	–	–	G	0.25	998.5	0.758	5,139
1695	Air	–	–	–	I	0.25	993.4	0.756	5,240
1722	Air	–	–	–	H	0.25	955.8	0.758	4,087
1734	Air	–	–	–	J	0.125	970.0	0.757	4,122
1737	Air	–	–	–	K	0.125	963.7	0.757	4,105
1763	Hi DO	620	5.9	0.07	C	0.830	974.9	0.848	340
1765	Hi DO	590	6.0	0.07	D	0.650	977.3	0.806	615
1677	Hi DO	800	6.0	0.11	E	0.666	926.5	0.762	545
1684	Hi DO	700	6.0	0.09	F	0.334	964.0	0.762	1,935
1753	Hi DO	670	5.9	0.07	F	0.334	982.6	0.777	1,831
1678	Hi DO	700	5.9	0.14	G	0.347	944.4	0.780	615
1703	Hi DO	650	5.9	0.13	G	0.347	942.4	0.760	553
1692[b]	Hi DO	700	6.0	0.10	G	0.347	936.4	0.764	261
1728	Hi DO	700	5.9	0.07	H	0.167	969.3	0.740	1,649
1732	Hi DO	600	5.9	0.08	H	0.167	954.5	0.734	2,080
1698	Hi DO	600	6.1	0.08	I	0.319	909.1	0.756	1,306
1741	Hi DO	600	6.0	0.09	J	0.170	896.8	0.785	888
1742	Hi DO	520	6.0	0.09	K	0.084	948.0	0.783	2,093
A533-Gr B Steel									
1708	Air	–	–	–	E	0.50	898.2	0.754	5,355
1710	Air	–	–	–	G	0.25	885.6	0.753	3,630
1767	Air	–	–	–	I	0.25	886.3	0.752	7,502
1713	Hi DO	670	5.9	0.07	E	0.666	890.8	0.761	426
1714	Hi DO	570	5.9	0.08	G	0.347	886.1	0.748	578
1769	Hi DO	630	6.0	0.07	I	0.319	877.2	0.729	976

[a]Represent DO levels in effluent water. DO levels in supply water were 150–350 ppb higher.
[b]A slow strain rate of 0.0004%/s was used for this test.

The results to date indicate that a slow strain rate applied during each portion of the loading cycle above the threshold strain is equally effective in decreasing fatigue life.[15–17] At 288°C and a strain range of ≈0.75%, the average fatigue life of A106–Gr B steel in air is ≈4000 cycles. Relative to air, the fatigue lives in simulated PWR water at all strain rates or in high-DO water at high strain rates (i.e., fast/fast tests) are lower by ≈50%. If each portion of the tensile-loading cycle is equally effective in reducing fatigue life, the life should decrease linearly from A to C along the chain-dot line in Fig. 13 and a slow strain rate near peak compressive strain (waveforms F, H, or K) should be as equally damaging as a slow strain rate near peak tensile strain (waveforms E, G, or H). The results show that a slow strain rate near peak compressive strain causes little or no reduction in fatigue life.

As discussed in Section 2.2, the results of the present study indicate that a minimum strain is required for environmentally assisted decrease in fatigue life. This threshold strain may vary with material and loading conditions such as steel type, temperature, DO, strain ratio, mean stress, etc. For the present study, the threshold strain may vary with material and loading conditions such as steel type, temperature, DO, strain ratio, mean stress, etc. For the present study, the threshold strain range for both A106–Gr B carbon steel and A533–Gr B low-alloy steel is ≈0.36%. If each portion of the loading cycle above the threshold strain is equally damaging, the decrease in fatigue life should follow line ABC when a slow rate is applied near peak tensile strain and line ADC when it is applied near

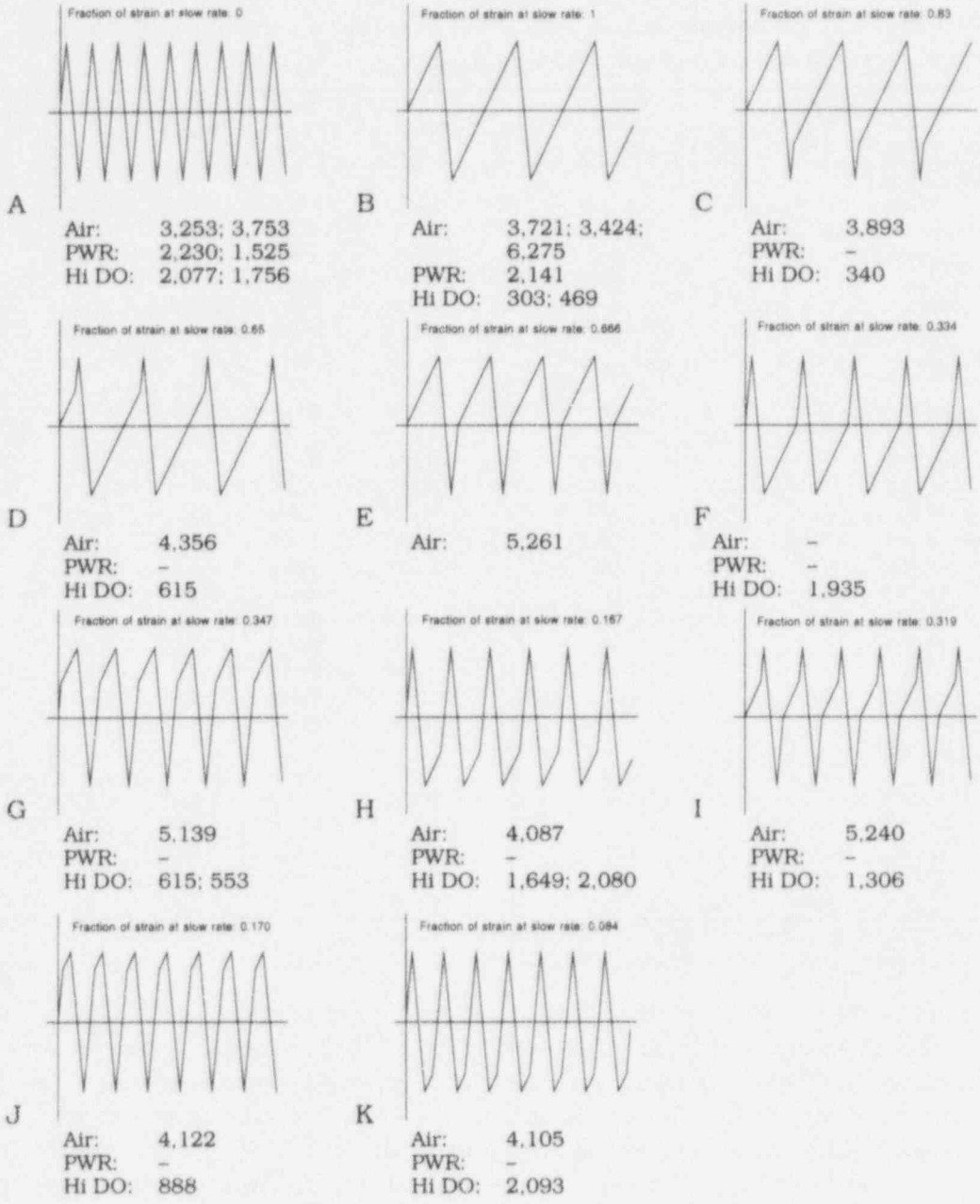

Figure 12. Fatigue life of A106–Gr B carbon steel at 288°C and 0.75% strain range in air and water under different loading waveforms

peak compressive strain. The results are in agreement with this behavior, i.e., a slow strain rate applied during each portion of the loading cycle above the threshold strain is equally effective in decreasing fatigue life. Tests on A533–Gr B steel also exhibit a similar trend.

This behavior is consistent with the slip–dissolution model for crack propagation;[29] applied strain must exceed a threshold value to rupture the passive surface film in order for environmental effects to occur. This does not mean that the observed threshold strain is the actual film rupture strain. Film rupture occurs at the crack tip and is controlled by crack tip strain. The threshold strain measured in smooth–specimen tests is a surrogate that in essence controls crack tip strain, but no numerical equality between the two need be implied.

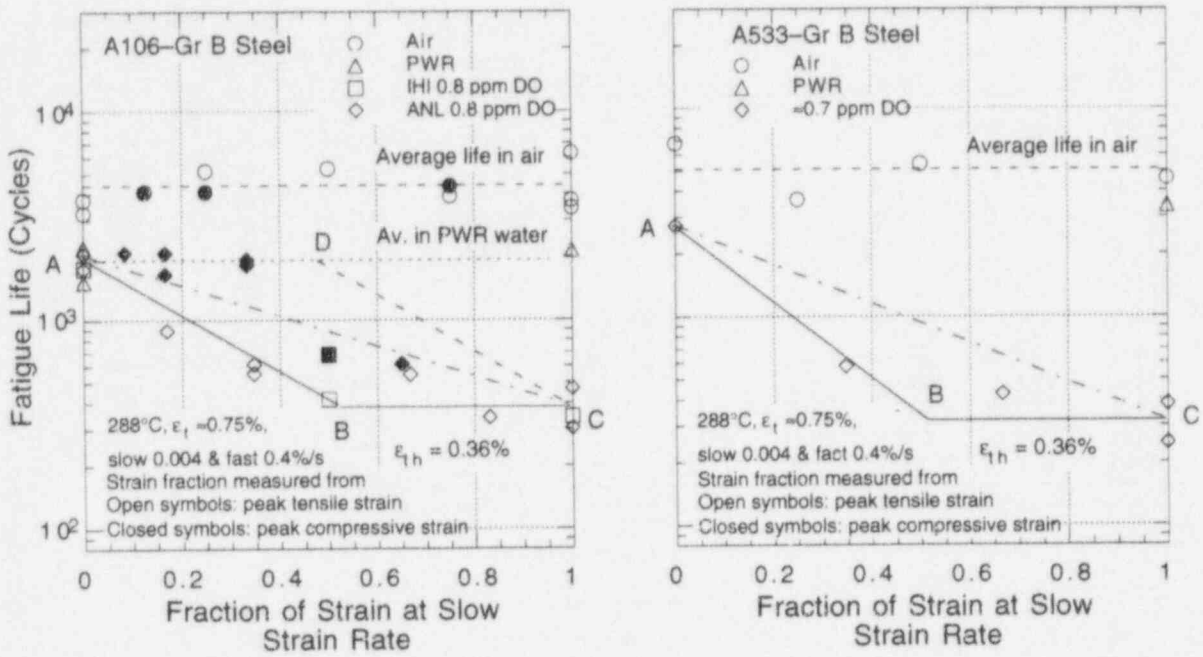

Figure 13. Fatigue life of A106–Gr B and A533–Gr B steels tested with loading waveforms where slow strain rate is applied during a fraction of tensile loading cycle

However, results from studies at the IHI Co. of Japan* indicate that all portions of the tensile loading cycle are equally damaging, even the portion of the loading cycle that has only elastic strain. Consequently, fatigue tests have been conducted on an IHI heat of A333–Gr 6 steel to validate the ANL results. The chemical composition of the steel is given in Table 1. The results of exploratory tests on A333–Gr 6 steel are summarized in Table 8. The loading waveforms and corresponding fatigue lives for tests at ≈0.80% strain range are shown in Fig. 14. The change in fatigue life of A333–Gr 6 steel with fraction of loading strain at slow strain rate is shown in Fig. 15. The tests conducted at IHI in water containing 8 or 0.8 ppm DO are also included in the figure.

The ANL and IHI results are in complete agreement. However, the data for tests in water with either F or K waveforms appear to have a different trend than that for A106–Gr B steel. The results indicate that a slow strain rate near peak compressive strain causes a significant reduction in fatigue life. In high-DO water, fatigue lives for specimens with waveforms F or K are lower by a factor of ≈2 than those for the fast/fast tests (waveform A). For A106–Gr B steel, fatigue lives for tests with waveforms A, F, or K are ≈1900 cycles. This apparent disagreement may be attributed to the effect of strain rate. Both A302–Gr B low-alloy steel and A333–Gr 6 carbon steel exhibit a strain rate effect, e.g., fatigue life of the steel in air decreased ≈20% when the strain rate decreases from 0.4 to 0.004 %/s. In Fig. 15, the decrease in fatigue life from A to A′ is most likely caused by the effect of strain rate. If each portion of the loading cycle above the threshold strain is equally damaging, the decrease in fatigue life due to environmental effects should follow line A′BC when a slow rate is applied near peak tensile strain and line A′DC when it is applied near peak compressive strain.

*Progress Report on Experimental Research on Fatigue Life in LWR Environment, May 1993 to September 1994, prepared by Japanese EFD Committee, Thermal and Nuclear Power Engineering Society, presented at the Pressure Vessel Research Council meetings in New York, October 10–13, 1994.

Table 8. Fatigue test results for A333–Gr 6 carbon steel at 288°C

Test Number	Environment	Dissolved Oxygen[a] (ppb)	pH at RT	Conductivity (μS/cm)	Waveform[b]	Fraction of strain at slow rate	Stress Range (MPa)	Strain Range (%)	Life N_{25} (Cycles)
1739	Air	–	–	–	A	0.0	882.9	0.809	9,483
1740	Air	–	–	–	B	1.0	936.8	0.808	7,665
1756	Air	–	–	–	E	0.500	967.4	0.808	10,156
1754	Air	–	–	–	F	0.500	963.2	0.806	6,696
1745	Air	–	–	–	J	0.125	961.3	0.808	8,519
1747	Air	–	–	–	K	0.125	964.6	0.810	6,537
1746	Hi DO	715	6.1	0.09	A	0.0	788.3	0.829	3,550
1748	Hi DO	645	6.0	0.10	B	1.0	881.3	0.794	555
1755	Hi DO	660	5.9	0.07	F	0.334	933.5	0.803	1,670
1758	Hi DO	560	5.8	0.07	E	0.666	892.3	0.799	620
1750	Hi DO	680	5.9	0.10	J	0.170	886.7	0.811	1,235
1751	Hi DO	590	5.9	0.07	K	0.084	913.1	0.808	2,325

[a]Represent DO levels in effluent water. DO levels in supply water were 150–350 ppb higher.

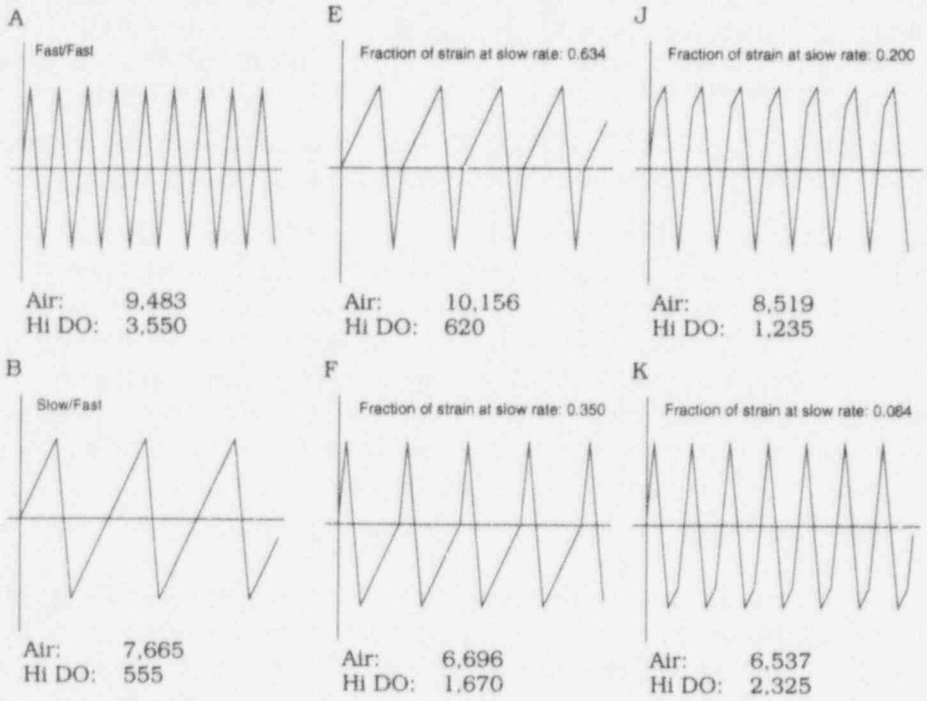

Figure 14. Fatigue life of A106–Gr B carbon steel at 288°C and 0.75% strain range in air and water environments under different loading waveforms

The cyclic–hardening behavior of the steel is quite different than that of the ANL heat of A106–Gr B carbon steel. Plots of cyclic stress range vs. fatigue cycles for A106–Gr B and A333–Gr 6 carbon steels tested in air at 288°C, total strain range of 0.75 or 0.80%, and strain rates of 0.4 and 0.004 %/s are shown in Fig. 16. The A333–Gr 6 steel has a very low yield stress and shows significant cyclic hardening during the entire test. The A106–Gr B steel has a higher yield stress and exhibits a rapid cyclic hardening only during the initial 100 cycles. The latter also shows some dynamic strain aging at slow strain rates. The microstructural differences in the two steels caused by different waveforms may explain strain rate effects in A333–Gr B steel.

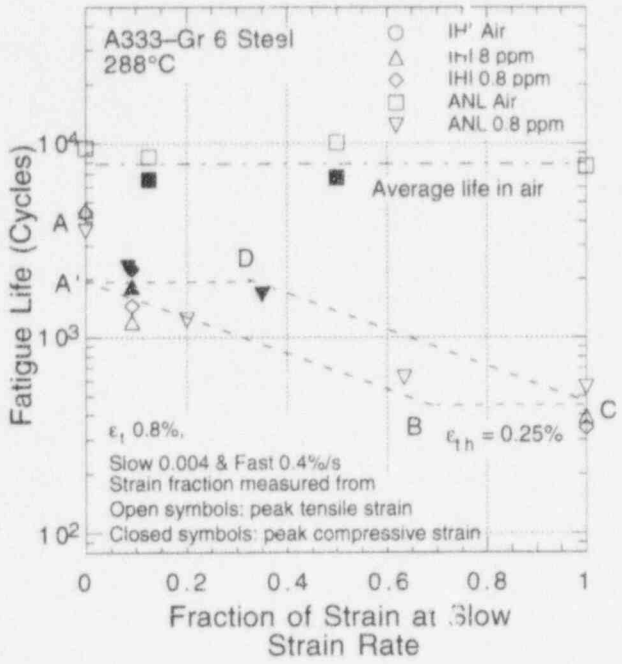

Figure 15.
Fatigue life of A333–Gr 6 carbon steel tested in air and water with loading waveforms where slow strain rate is applied during a fraction of the tensile cycle

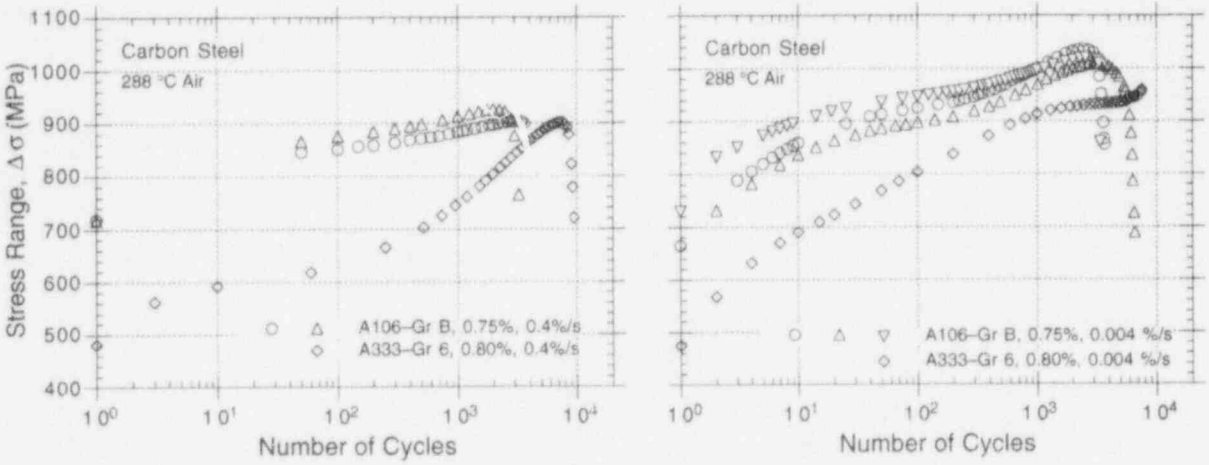

Figure 16. Effect of strain rate on cyclic strain-hardening behavior of A106–Gr B and A333–Gr 6 steels in air at 288°C and 0.75% strain range

3 Environmentally Assisted Cracking of Alloys 600 and 690 in Simulated LWR Water

The objective of this work is to evaluate resistance of Alloys 600 and 690 to environmentally assisted cracking (EAC) in simulated light-water-reactor (LWR) coolant environments. High-nickel alloys have experienced general corrosion (tube wall thinning) and localized intergranular attack (IGA) and stress corrosion cracking (SCC) in LWRs. Secondary-side IGA* and axial and circumferential SCC** have occurred in Alloy 600 tubes at tube support plates in many steam generators. Primary-water stress-corrosion cracking (PWSCC) of Alloy 600 steam generator tubes in pressurized water reactors (PWRs) at roll transitions and U-bends and in tube plugs*** is a widespread problem that has been studied intensively. Cracking has also occurred in Alloy 600 and other high-nickel alloys (e.g., Inconel-82 and -182 and Alloy X750) used for applications such as (a) instrument nozzles and heater thermal sleeves in the pressurizer† and penetrations for control-rod-drive mechanisms in reactor vessel closure heads in the primary system of PWRs†† and (b) in dissimilar-metal weldments between SS piping and low-alloy steel nozzles, in jet pump hold-down beams,††† and in shroud-support-access-hole covers§ in BWRs. Alloy 600, in general, undergoes different thermomechanical processing for applications other than those used for steam generator tubes. Because environmental degradation of the alloys in many cases is very sensitive to processing, further evaluation is needed even for SCC. In addition, experience strongly suggests that materials that are susceptible to SCC are also susceptible to environmental degradation of fatigue life and fatigue-crack-growth properties.

In this investigation, we have obtained preliminary information on the effect of temperature, load ratio, and stress intensity on EAC of Alloys 600 and 690 in simulated BWR and PWR water. CGRs of these materials have been compared with those of Type 316NG and sensitized Type 304 SS under conditions where EAC occurs in all materials.[30]

3.1 Technical Progress (W. E. Ruther, W. K. Soppet, D. J. Gavenda, and T. F. Kassner)

During this reporting period, microstructures and tensile properties of several heats of Alloys 600 and 690 were determined. Compact-tension specimens were fabricated from the various materials for fracture-mechanics CGR tests in simulated LWR environments.

*USNRC Information Notice No. 91-67, "Problems with the Reliable Detection of Intergranular Attack (IGA) of Steam Generator Tubing," Oct. 1991.

**USNRC Information Notice No. 90-49, "Stress Corrosion Cracking in PWR Steam Generator Tubes," Aug. 1990; Notice No. 91-43, "Recent Incidents Involving Rapid Increases in Primary-to-Secondary Leak Rate," July 1991; Notice No. 92-80, "Operation with Steam Generator Tubes Seriously Degraded," Dec. 1992; Notice No. 94-05, "Potential Failure of Steam Generator Tubes with Kinetically Welded Sleeves," Jan.1994.

***USNRC Information Notice No. 89-33, "Potential Failure of Westinghouse Steam Generator Tube Mechanical Plugs," March 1989; Notice No. 89-65, "Potential for Stress Corrosion Cracking in Steam Generator Tube Plugs Supplied by Babcock and Wilcox," Sept. 1989; Notice No. 94-87, "Unanticipated Crack in a Particular Heat of Alloy 600 Used for Westinghouse Mechanical Plugs for Steam Generator Tubes," Dec. 1994.

†USNRC Information Notice No. 90-10, "Primary Water Stress Corrosion Cracking (PWSCC) of Inconel 600," Feb. 1990.

††INPO Document SER 20-93 "Intergranular Stress Corrosion Cracking of Control Rod Drive Mechanism Penetrations," Sept.1993.

†††USNRC Information Notice No. 93-101, "Jet Pump Hold-Down Beam Failure," Dec. 1993.

§USNRC Information Notice No. 92-57, "Radial Cracking of Shroud Support Access Hole Cover Welds," Aug. 1992.

3.1.1 Material Characterization

Characterization of the various heats of Alloys 600 and 690 obtained for corrosion-fatigue testing was completed. The heat identification numbers, product form, and source of materials for fabrication of 1T-compact tension specimens are given in Table 9.

Table 9. Product form and source of Alloys 600 and 690

Material	Heat No.	Material Condition	Product Form	Source
600	NX8844B-33	Annealed 872°C/1 h	1.0-in.-thick plate	EPRI[a]
600	J422	Mill Annealed	1T-CT specimens	Metal Samples Co.
600	NX8197	Mill Annealed	1.0-in.-thick plate	A. M. Castle & Co.
600	NX8844J-26	Annealed 1038°C/1 h	1.0-in.-thick plate	EPRI
600	NX8844G-3	Hot Worked 982°C, 20% Reduction	1.0-in.-thick plate	EPRI
690	NX8662HG-33	Annealed + 715°C/5 h	1.34-in.-thick plate	INCO Alloys Intl., Inc.
690	NX8625HG-21	Annealed + 715°C/5 h	1.34-in.-thick plate	EPRI
690	NX8244HK-1A	Annealed 982°C/1 h	1.0-in.-thick plate	EPRI
690	NX8244HK-1B	Annealed 1093°C/1 h	1.0-in.-thick plate	EPRI

[a]Numerous heats of Alloys 600 and 690 were fabricated by INCO Alloys International, Inc., Huntington, WV, for the Electric Power Research Institute (EPRI), Palo Alto, CA, which provided materials for this study.

The chemical composition of the materials is given in Tables 10 and 11. The tensile properties of cylindrical specimens in air at 25, 290, and 320°C and a strain rate of 1.0×10^{-4} s^{-1} were determined in accordance with ASTM Standard E8. Vickers hardness was measured at room temperature, and average grain size of the various heats of Alloys 600 and 690 was determined following the procedure in ASTM Standard E112. The results for Alloy 600 and 690 are given in Tables 12 and 13, respectively. Properties obtained from certified material test reports (CMTRs) supplied by the vendors or documentation obtained from the EPRI are also included in Tables 12 and 13. Data for annealed specimens tend to follow a Petch relation, i.e., $\sigma_y = \sigma_i + k \cdot d^{-1/2}$, where σ_y is the yield stress, d the grain diameter, k an empirical constant, and σ_i the "friction" stress, which is a measure of intrinsic resistance of the material to dislocation motion. The dependence of yield stress of annealed Alloy 600 (Heat NX8844) and 690 (Heat NX8244HK) specimens at 25, 290, and 320°C on average grain size is shown in Fig. 17. Photomicrographs that were used to determine the grain size of the various heats of Alloys 600 and 690 are shown in Figs. 18 and 19, respectively.

A small section of each material was used to prepare metallographic specimens to determine qualitatively the degree of grain boundary carbide coverage by optical metallography. Specimens were polished to a 0.25-μm diamond finish with Struers DP-Spray, and a Vickers hardness indentation was made to provide a reference point for subsequent examination to reveal the carbide distribution and grain boundaries after different chemical etching methods. The specimens were electroetched in a 10% H_3PO_4 solution at ≈10 V for ≈25 s, rinsed in ethanol, and air dried. Photomicrographs that primarily reveal carbides present in the material were obtained at a magnification of 500X. The specimens were

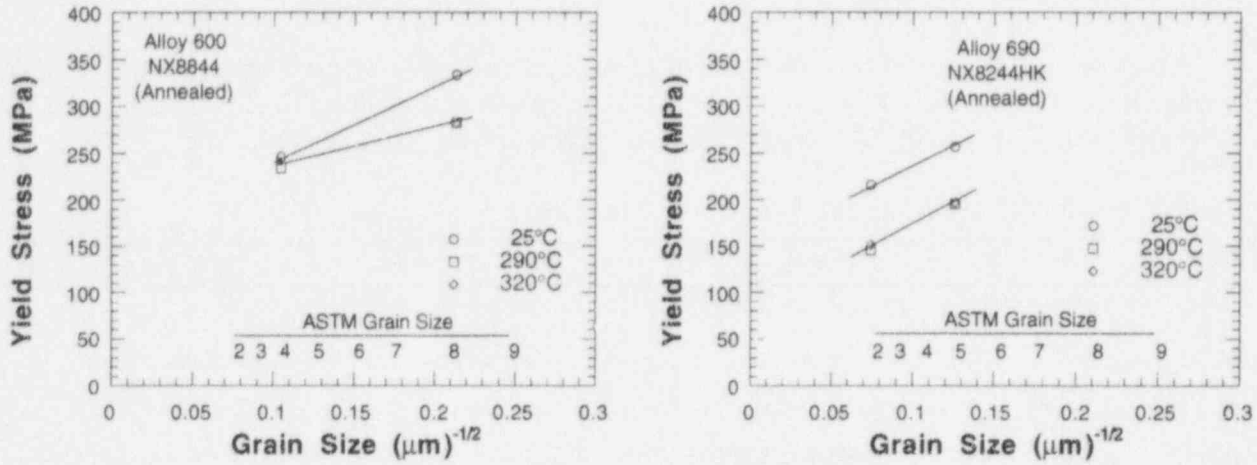

Figure 17. Dependence of 0.2% yield stress at 25, 290, and 320°C on grain size of annealed Alloy 600 and 690 specimens

repolished with 1.0 and 0.25-μm diamond spray, electroetched in a 5% nital solution (5 mL of HNO_3 in 100 mL ethanol) at ≈10 V for ≈35 s, rinsed in ethanol, and air dried. The specimens were photographed once again at a magnification of 500X in the same location with the aid of the hardness indentation to better reveal grain boundaries and obtain a qualitative estimate of the extent of carbide precipitation thereon.

Photomicrographs of the five heats of Alloy 600 (≈0.06 wt.% carbon) in Figs. 20–24 indicate either semicontinuous or continuous carbide precipitation at the grain boundaries plus a significant amount of intragranular carbide. Photomicrographs of the four heats of Alloy 690 (≈0.03 wt.% carbon) in Figs. 25–28 reveal continuous precipitation of carbides at the grain boundaries with relatively few intragranular carbides. The precipitate phases present in Alloys 600 and 690 are Cr-rich M_7C_3 and $M_{23}C_6$ carbides and TiN. In general, the microstructures are consistent with the thermomechanical processing histories and carbon concentrations vis-a`-vis the solubility of carbon in the materials[1] (Fig. 29). Namely, according to these carbon solubility data, none of the materials was annealed at a temperature high enough to dissolve all of the carbon in the grain matrix (Alloy 690, >1200°C and Alloy 600, >1080°C); consequently, carbides are present on grain boundaries as well as within the grains, in particular, Alloy 600 which contains ≈0.06 wt.% carbon.

3.1.2 CGRs of Mill-Annealed Alloy 600 and Thermally Treated Alloy 690 in HP Water at 289 and 320°C

Corrosion-fatigue experiments are being conducted on mill-annealed Alloy 600 (Heat No. NX8197) and mill-annealed plus thermally treated Alloy 690 (NX8662HG-33) specimens in HP water to investigate the effects of dissolved oxygen and hydrogen in water and temperature on CGRs of these materials. These specimens have a similar grain size (Figs. 18c and 19a) and both have a continuous carbide distribution along grain boundaries (Figs. 22 and 25), although Alloy 690 contains few intragranular carbides. At 290–320°C, the ultimate tensile and yield strengths of these heats of Alloy 600 and 690 are ≈660 and 321 and 600 and 235 MPa, respectively.

Table 10. Chemical composition of Alloy 600 for corrosion fatigue tests

Material	Heat No.	Analysis	Composition (wt.%) Cr	Mo	Ni	Fe	Mn	Si	C	N	P	S	B	Cu	Ti	Al	Co	Nb+Ta
Alloy 600	J422	Vendor	15.36	–	75.72	7.51	0.21	0.32	0.080	–	0.008	<0.001	–	0.15	0.24	0.28	0.05	0.07
		ANL	15.37	0.23	76.36	7.27	0.20	0.32	0.080	0.0145	0.016	0.004	0.002	0.15	0.16	0.27	0.05	0.06
Alloy 600	NX8197	Vendor	15.88	–	75.05	7.76	0.22	0.23	0.080	–	0.006	0.002	–	0.12	0.27	0.26	0.05	0.07
		ANL	15.43	0.58	73.82	9.20	0.20	0.27	0.080	0.0099	0.016	0.002	0.002	0.11	0.18	0.24	0.06	0.05
Alloy 600	NX8844	Vendor	14.97	0.15	75.21	8.26	0.26	0.24	0.069	0.01	0.009	<0.001	0.004	0.22	0.29	0.27	0.04	–
	NX8844B-33	ANL	15.03	0.17	75.16	7.93	0.24	0.27	0.080	0.0146	0.019	0.001	0.003	0.22	0.21	0.28	0.04	0.04
	NX8844J-26	ANL	15.00	0.16	74.94	8.14	0.23	0.32	0.060	0.0155	0.014	0.002	0.004	0.22	0.24	0.24	0.03	0.03
	NX8844G-3	ANL	15.14	0.16	74.78	8.28	0.23	0.35	0.070	0.0145	0.015	0.002	0.005	0.22	0.25	0.25	0.04	0.04

Table 11. Chemical composition of Alloy 690 for corrosion fatigue tests

Material	Heat No.	Analysis	Composition (wt.%) Cr	Mo	Ni	Fe	Mn	Si	C	N	P	S	B	Cu	Ti	Al	Co	Nb+Ta
Alloy 690	NX8662HG-33	Vendor	30.25	–	59.31	9.54	0.10	0.16	0.030	0.050	0.008	<0.001	0.004	0.04	0.28	0.33	0.022	–
		ANL	30.46	0.04	58.88	9.22	0.11	0.16	0.030	0.047	0.017	0.001	0.003	0.05	0.25	0.32	0.020	0.01
Alloy 690	NX8625HG-21	Vendor	30.28	–	58.56	10.00	0.11	0.26	0.027	0.030	0.009	<0.001	0.004	0.06	0.32	0.44	0.036	–
		ANL	30.64	0.02	58.10	9.84	0.12	0.32	0.030	0.029	0.009	0.002	0.004	0.01	0.28	0.39	0.030	<0.01
Alloy 690	NX8244HK	Vendor	30.03	–	59.85	9.20	0.20	0.14	0.018	0.01	0.004	<0.001	0.002	<0.01	0.20	0.36	0.003	–
	NX8244HK-1A	ANL	30.66	<0.01	59.09	9.22	0.20	0.18	0.024	0.010	0.004	0.002	0.002	<0.01	0.20	0.31	<0.01	<0.01
	NX8244HK-1B	ANL	30.64	<0.01	59.20	9.19	0.21	0.18	0.023	0.011	0.005	0.002	0.002	<0.01	0.19	0.32	<0.01	<0.01

Table 12. Tensile properties of Alloy 600 in various heat-treatment conditions

Alloy 600 Heat No.	Material Condition	Test No.	Spec. No.	Temp. (°C)	σ_u (MPa)	σ_y (MPa)	ε_t (%)	RA (%)	Hardness[a] (VN)	Hardness (R_b)	ASTM Grain Size
NX8844B-33	Annealed 872°C/1 h	–[b]	–[b]	25	748.8	339.9	35.5	–	–	90	7.5
NX8844B-33	Annealed 872°C/1 h	T19	B33-05[c]	25	714.9	333.2	39.6	66.9	91	–	8
NX8844B-33	Annealed 872°C/1 h	T8	B33-03[c]	290	686.1	282.6	38.6	61.1	–	–	–
NX8844B-33	Annealed 872°C/1 h	T10	B33-04[c]	320	680.6	282.6	39.1	55.5	–	–	–
J422	Mill Annealed	–[b]	–[b]	25	722.6	273.0	40.0	–	–	87	–
J422	Mill Annealed	T20	IN-05[c]	25	732.8	370.7	39.2	64.5	93	–	7
J422	Mill Annealed	T9	IN-03[c]	290	699.4	313.7	40.1	53.5	–	–	–
J422	Mill Annealed	T11	IN-04[c]	320	697.9	311.3	39.0	53.9	–	–	–
NX8197	Mill Annealed	–[b]	–[b]	25	683.3	256.5	42.0	–	–	81	–
NX8197	Mill Annealed	T7	197-04[c]	25	683.9	373.6	42.2	64.4	90	–	6
NX8197	Mill Annealed	T12	197-05[c]	25	685.4	392.8	41.6	64.9	–	–	–
NX8197	Mill Annealed	T3	197-02[c]	290	668.1	316.9	46.8	62.2	–	–	–
NX8197	Mill Annealed	T5	197-03[c]	320	656.8	327.4	42.4	60.5	–	–	–
NX8844J-26	Annealed 1038°C/1 h	–[b]	–[b]	25	694.3	298.6	41.0	–	–	86	4
NX8844J-26	Annealed 1038°C/1 h	T21	J26-05[c]	25	653.5	245.5	49.2	61.1	87	–	4
NX8844J-26	Annealed 1038°C/1 h	T23	J26-06[c]	290	637.8	234.0	45.2	53.3	–	–	–
NX8844J-26	Annealed 1038°C/1 h	T25	J26-07[c]	320	639.4	246.8	45.8	48.9	–	–	–
NX8844G-3	Hot Worked 982°C, 20% Reduction	–[b]	–[b]	25	697.8	355.1	38.5	–	–	85	2.5
NX8844G-3	Hot Worked 982°C, 20% Reduction	T13	G3-05[c]	25	666.4	335.3	43.5	56.9	90	–	2
NX8844G-3	Hot Worked 982°C, 20% Reduction	T15	G3-06[c]	290	630.1	292.2	44.1	53.5	–	–	–
NX8844G-3	Hot Worked 982°C, 20% Reduction	T17	G3-07[c]	320	630.3	297.0	44.9	54.9	–	–	–

[a]Vickers hardness at room temperature, 500 gf, 15 s.
[b]Results from vendor (EPRI document or certified material test reports).
[c]Tensile tests conducted in air at a strain rate of 1.0×10^{-4} s^{-1}.

Table 13. Tensile properties of Alloy 690 in various heat-treatment conditions

Alloy 690 Heat No.	Material Condition	Test No.	Spec. No.	Temp. (°C)	σ_u (MPa)	σ_y (MPa)	ε_t (%)	RA (%)	Hardness[a] (VN)	Hardness (R_b)	ASTM Grain Size
NX8662HG-33	Annealed + 715°C/5 h	–[b]	–[b]	25	670.2	291.7	43.5	–	–	82	5
NX8662HG-33	Annealed + 715°C/5 h	T6	HG-03[c]	25	683.8	292.1	48.7	63.2	96	–	5
NX8662HG-33	Annealed + 715°C/5 h	T2	HG-01[c]	290	601.2	237.1	49.7	61.6	–	–	–
NX8662HG-33	Annealed + 715°C/5 h	T4	HG-02[c]	320	598.8	232.3	50.7	62.8	–	–	–
NX8625HG-21	Annealed + 715°C/5 h	–[b]	–[b]	25	660.5	268.9	48.0	–	–	82	4
NX8625HG-21	Annealed + 715°C/5 h	T27	G21-03[c]	25	641.8	297.0	56.4	75.2	86	–	5
NX8625HG-21	Annealed + 715°C/5 h	T28	G21-04[c]	290	570.9	225.2	56.0	58.8	–	–	–
NX8625HG-21	Annealed + 715°C/5 h	T29	G21-06[c]	320	567.8	220.4	56.9	61.3	–	–	–
NX8244HK-1A	Annealed 982°C/1 h	–[b]	–[b]	25	665.0	245.2	51.0	–	–	78	–
NX8244HK-1A	Annealed 982°C/1 h	T14	K1A-03[c]	25	647.7	256.3	56.9	75.2	82	–	5
NX8244HK-1A	Annealed 982°C/1 h	T16	K1A-04[c]	290	569.8	195.4	58.5	71.8	–	–	–
NX8244HK-1A	Annealed 982°C/1 h	T18	K1A-05[c]	320	572.2	196.4	58.2	71.7	–	–	–
NX8244HK-1B	Annealed 1093°C/1 h	–[b]	–[b]	25	602.8	212.3	59.0	–	–	70	–
NX8244HK-1B	Annealed 1093°C/1 h	T22	K1B-05[c]	25	592.2	215.6	70.5	71.6	80	–	2
NX8244HK-1B	Annealed 1093°C/1 h	T24	K1B-06[c]	290	504.9	145.2	70.6	68.1	–	–	–
NX8244HK-1B	Annealed 1093°C/1 h	T26	K1B-07[c]	320	499.4	150.9	67.1	67.3	–	–	–

[a]Vickers hardness at room temperature, 500 gf, 15 s.
[b]Results from vendor (EPRI document).
[c]Tensile tests conducted in air at a strain rate of 1.0×10^{-4} s^{-1}.

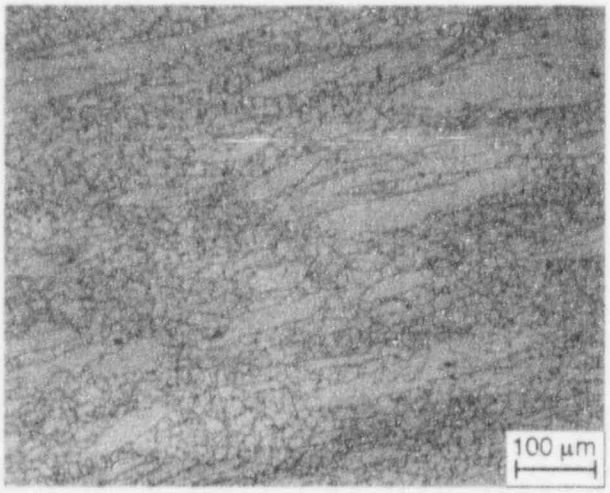

(a) Heat NX8844B-33, annealed at 872°C for 1 h, ASTM grain size 8

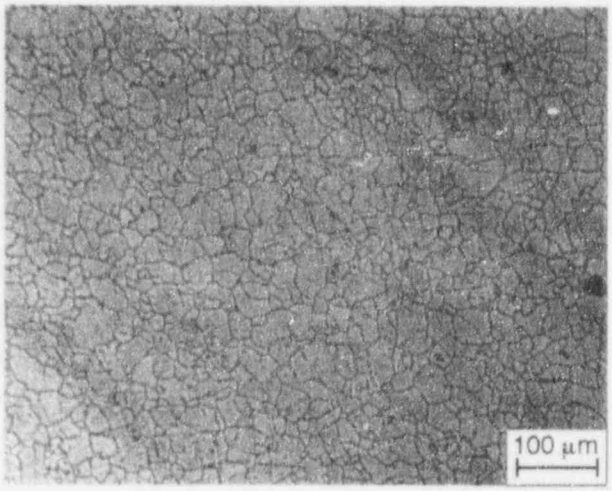

(b) Heat J422, mill annealed, ASTM grain size 7

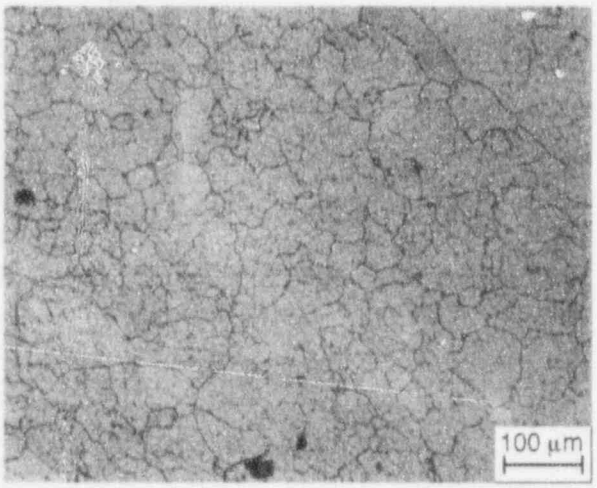

(c) Heat NX8197, mill annealed, ASTM grain size 6

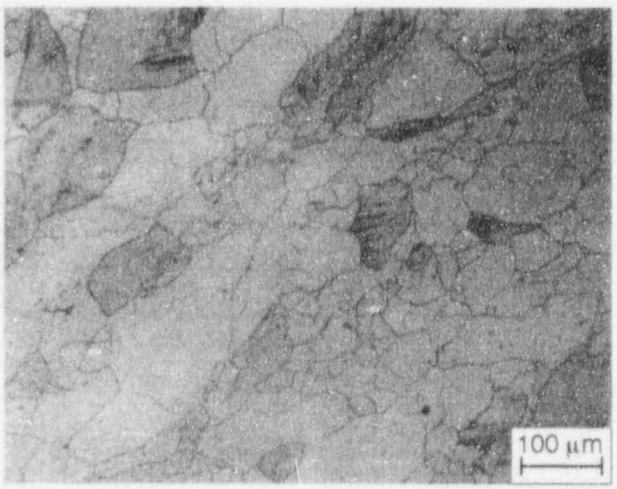

(d) Heat NX8844J-26, annealed at 1038°C for 1 h, ASTM grain size 4

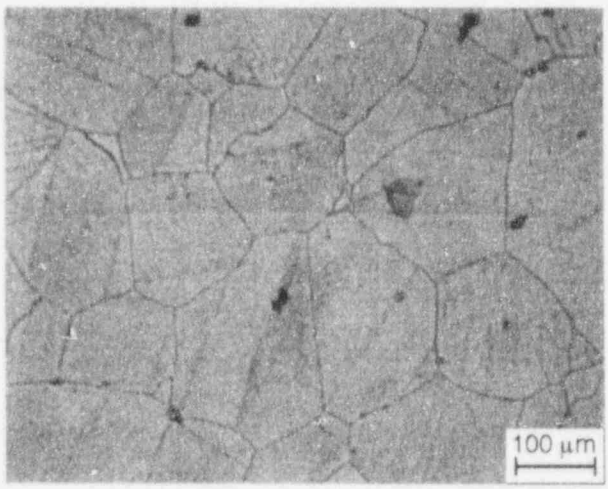

(e) NX8844G-3, hot-worked at 982°C 20% reduction, ASTM grain size 2

Figure 18. Microstructures of Alloy 600 heats for corrosion-fatigue tests in simulated reactor coolant environments after different thermomechanical processing

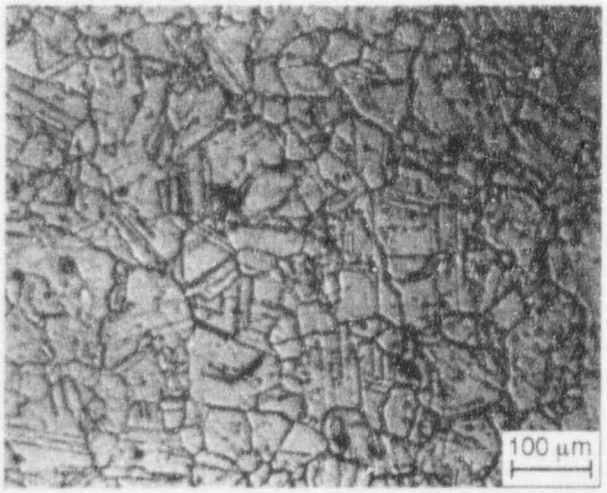

(a) Heat NX8662HG–33, annealed plus thermally treated at 715°C for 5 h, ASTM grain size 5

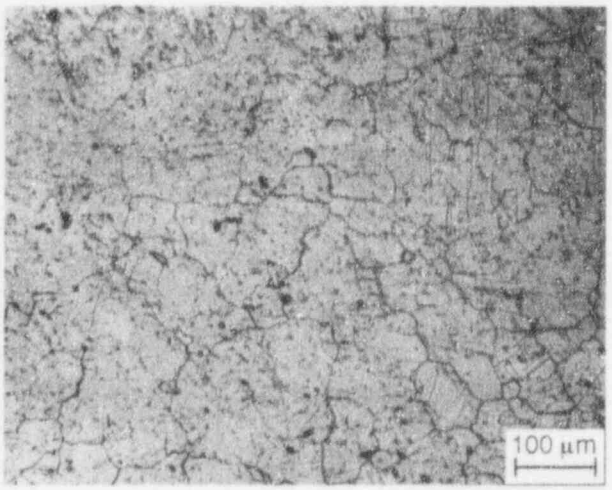

(b) Heat NX8625HG–21, annealed plus thermally treated at 715°C for 5 h, ASTM grain size 5

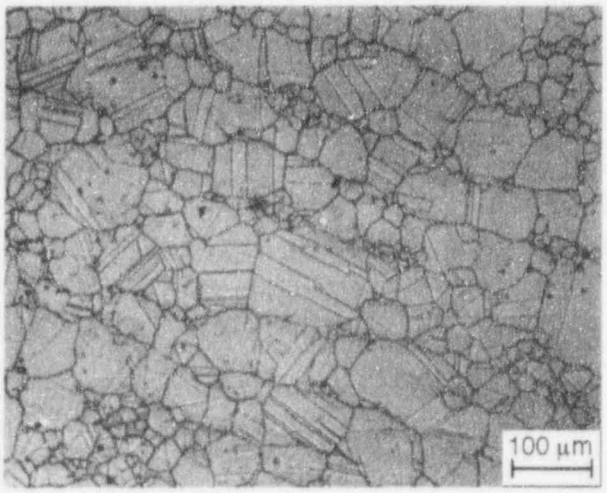

(c) Heat NX8244HK–1A, annealed at 982°C for 1 h, ASTM grain size 5

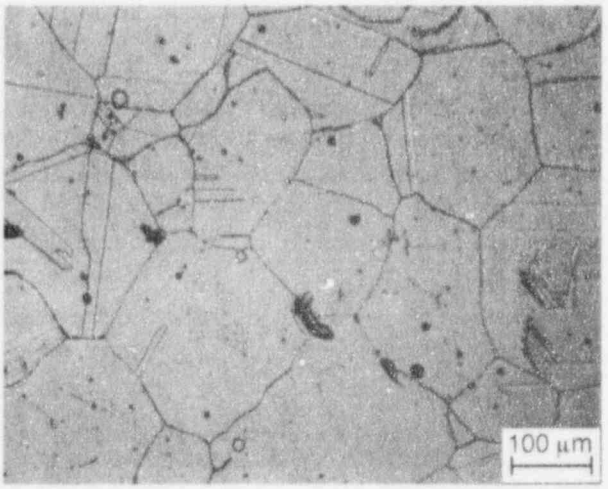

(d) Heat NX8244HK–1B, annealed at 1093°C for 1 h, ASTM grain size 2

Figure 19. Microstructures of Alloy 690 heats for corrosion–fatigue tests in simulated reactor coolant environments after different thermomechanical processing

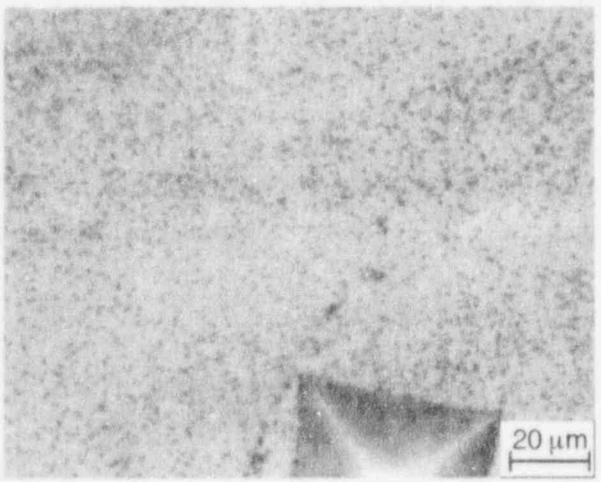

(a) Electroetched in 10% phosphoric acid solution

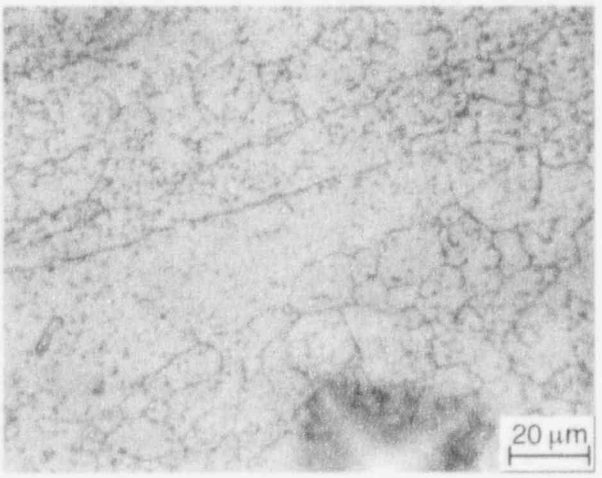

(b) Repolished and electroetched in 5% nital solution

Figure 20. Microstructures of Alloy 600, Heat NX8844B–33, that show a uniform distribution of intergranular and intragranular carbides

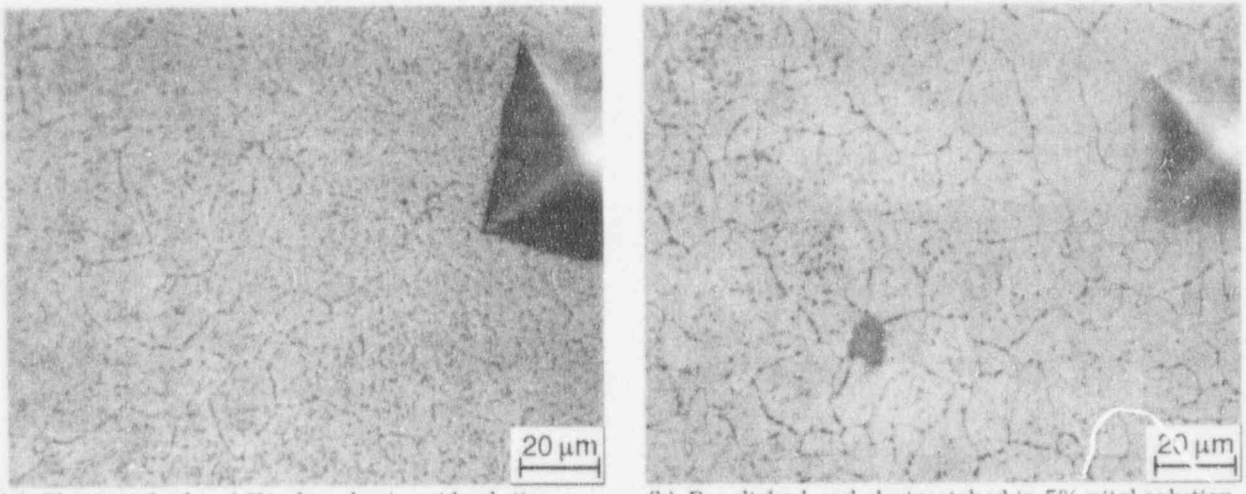

(a) Electroetched in 10% phosphoric acid solution (b) Repolished and electroetched in 5% nital solution

Figure 21. Microstructures of Alloy 600, Heat J422, that show semicontinuous intergranular plus intragranular carbides

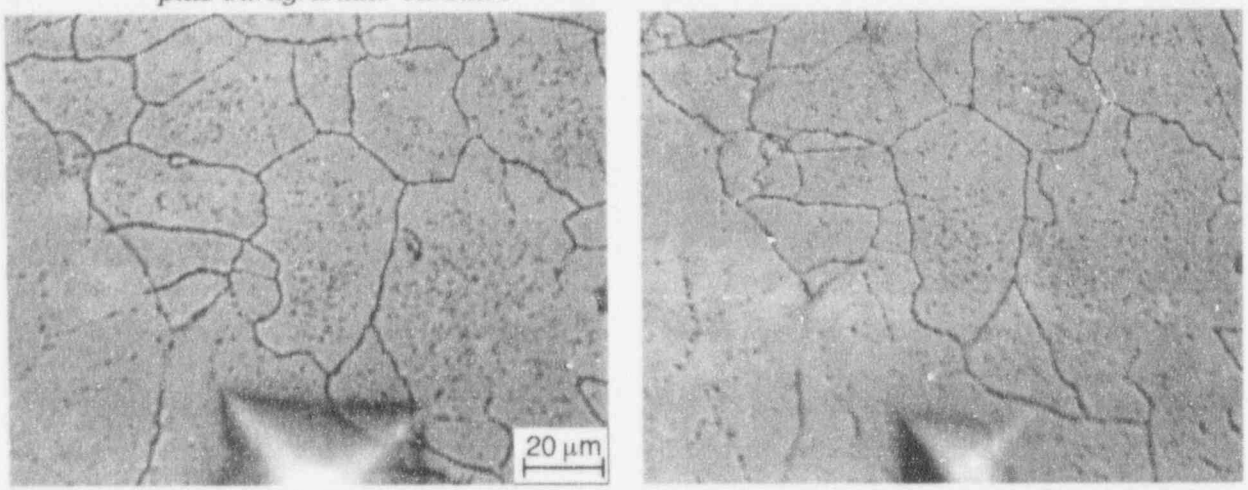

(a) Electroetched in 10% phosphoric acid solution (b) Repolished and electroetched in 5% nital solution

Figure 22. Microstructures of Alloy 600, Heat NX8197, that show continuous intergranular plus intragranular carbides

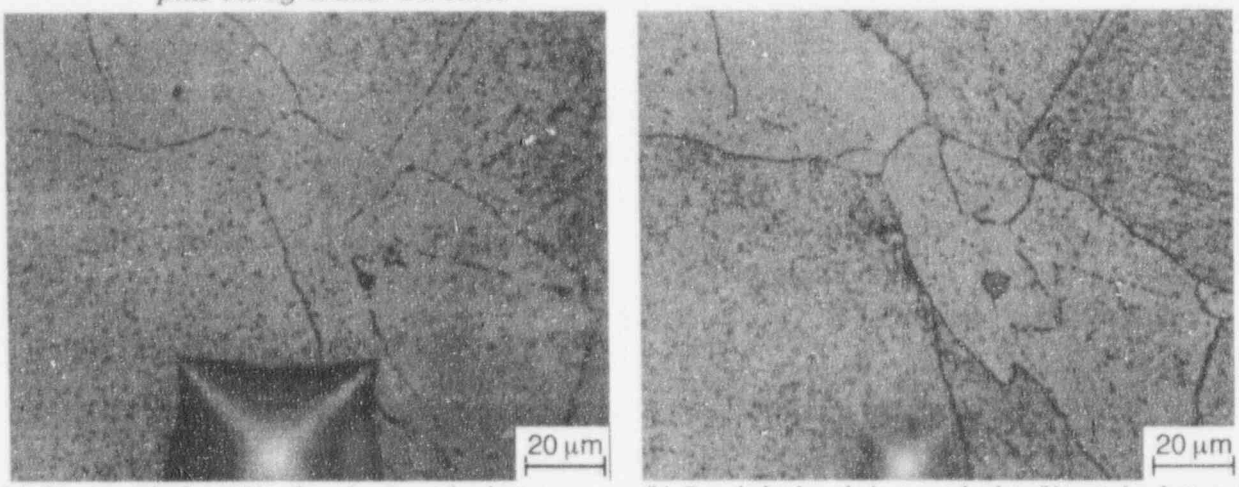

(a) Electroetched in 10% phosphoric acid solution (b) Repolished and electroetched in 5% nital solution

Figure 23. Microstructures of Alloy 600, Heat NX8844J-26, that show semicontinuous intergranular plus intragranular carbides

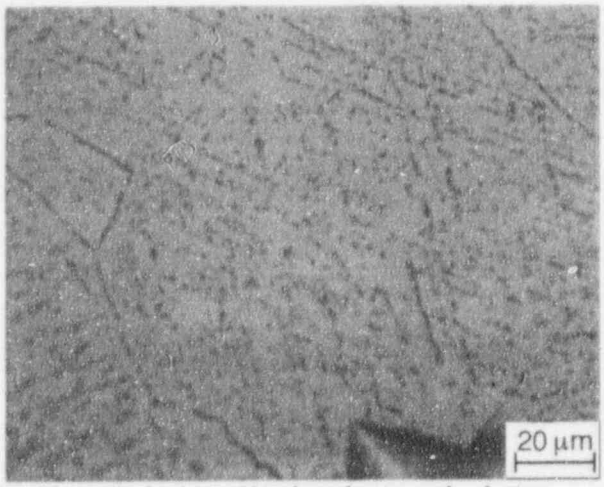

(a) Electroetched in 10% phosphoric acid solution

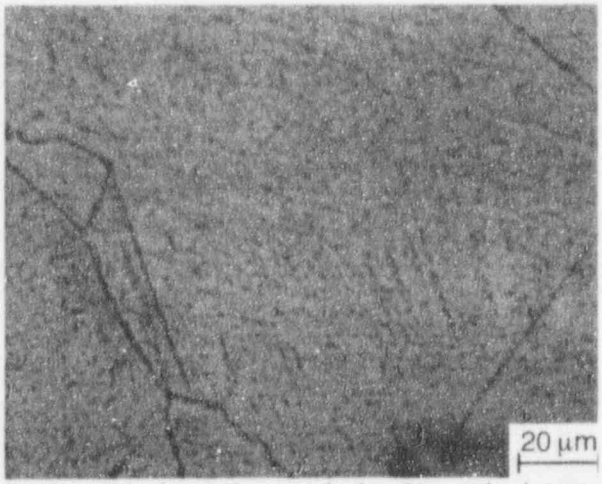

(b) Repolished and electroetched in 5% nital solution

Figure 24. Microstructures of Alloy 600, Heat NX8844G–3, that show semicontinuous intergranular plus intragranular carbides along slip lines

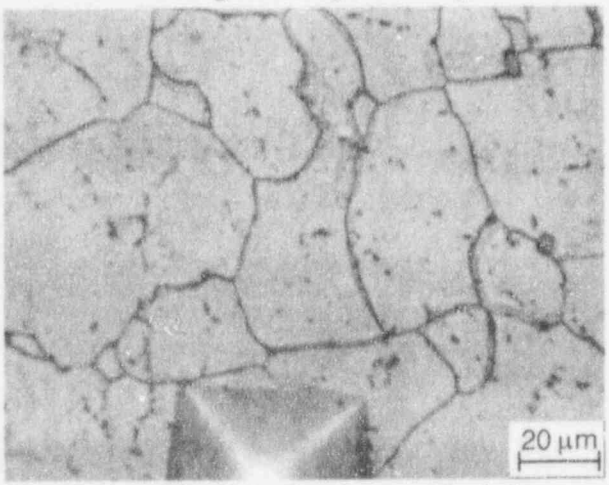

(a) Electroetched in 10% phosphoric acid solution

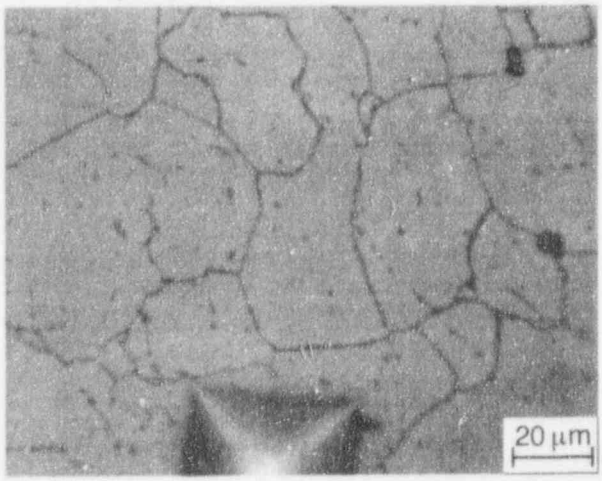

(b) Repolished and electroetched in 5% nital solution

Figure 25. Microstructures of Alloy 690, Heat NX8662HG–33, that show continuous intergranular plus relatively few intragranular carbides

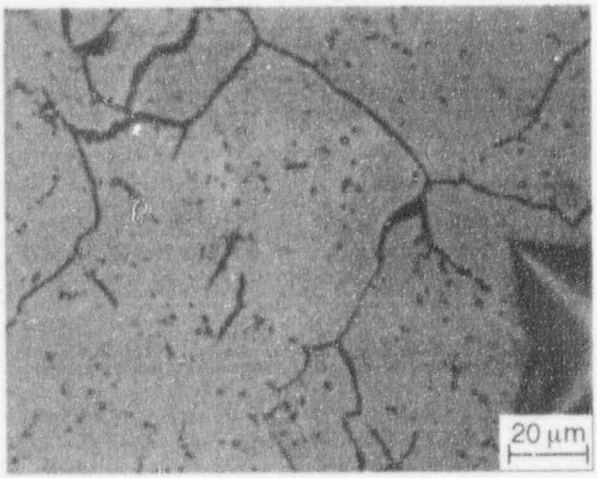

(a) Electroetched in 10% phosphoric acid solution

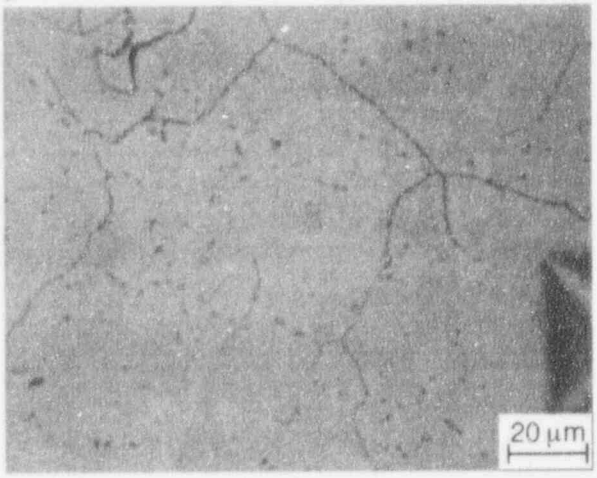

(b) Repolished and electroetched in 5% nital solution

Figure 26. Microstructures of Alloy 690, Heat NX8625HG–21, that show continuous intergranular plus some intragranular carbides

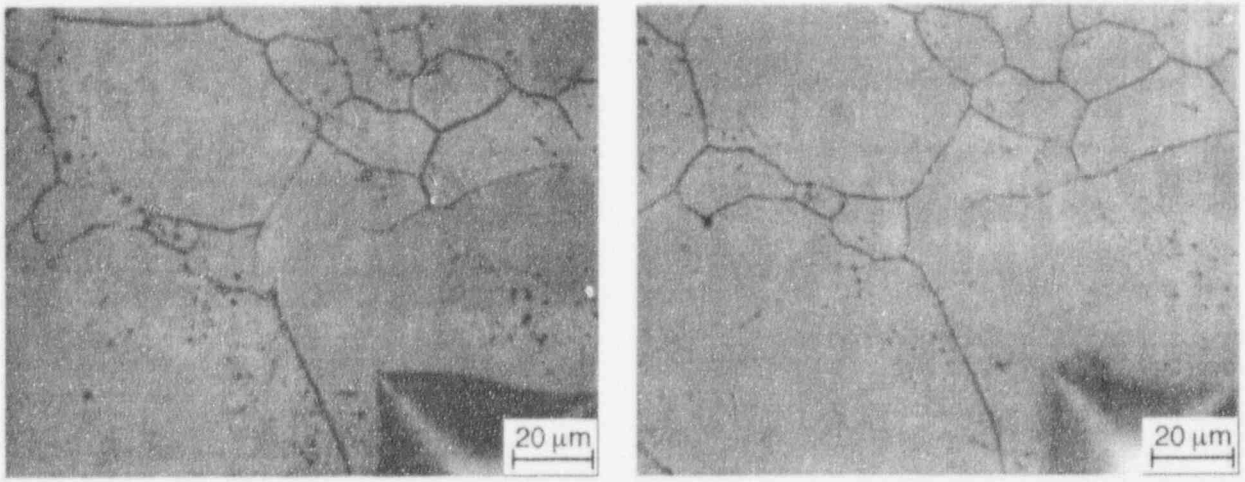

(a) Electroetched in 10% phosphoric acid solution (b) Repolished and electroetched in 5% nital solution

Figure 27. Microstructures of Alloy 690, Heat NX8244HK-1A, that show continuous intergranular but few intragranular carbides

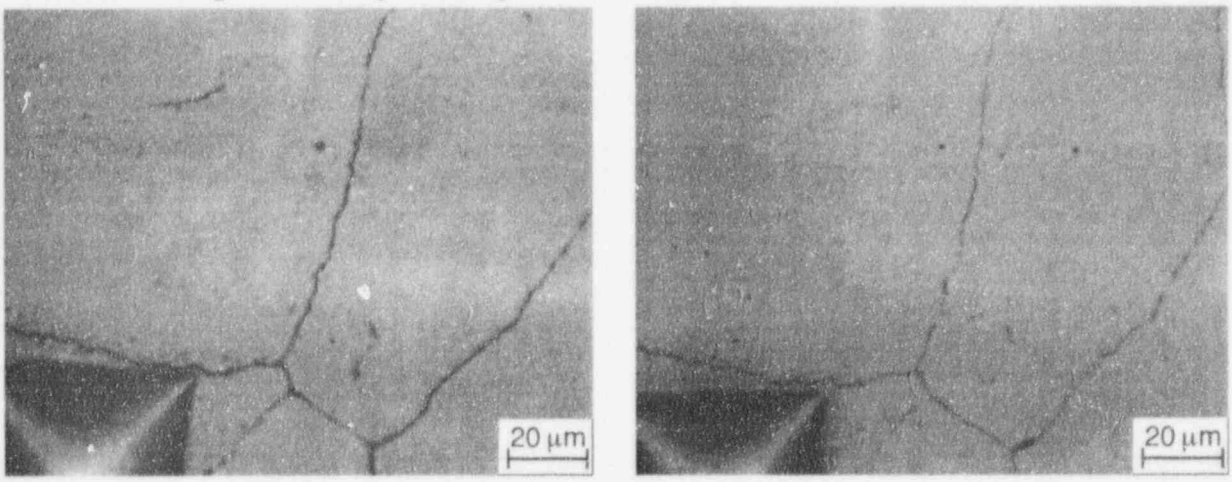

(a) Electroetched in 10% phosphoric acid solution (b) Repolished and electroetched in 5% nital solution

Figure 28. Microstructures of Alloy 690, Heat NX8844HK-1B, that show continuous intergranular but few intragranular carbides

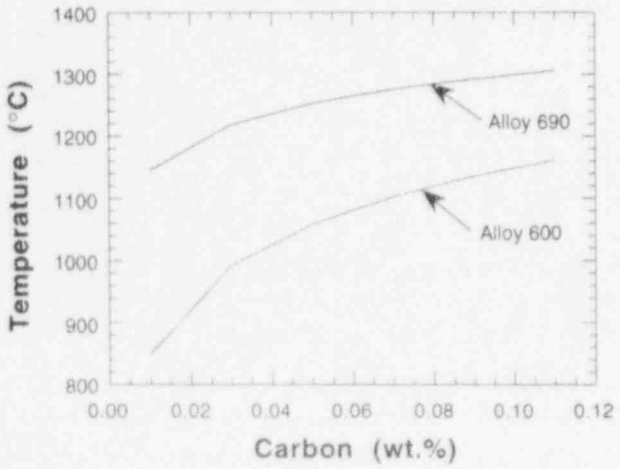

Figure 29. Solubility of carbon in Alloys 690 and 600 versus temperature, from Ref. 31

4 Irradiation-Assisted SCC of Austenitic SSs

In recent years, failures of reactor-core internal components in both BWRs and PWRs have increased after accumulation of relatively high fluence (>5 x 10^{20} n·cm^{-2}, E >1 MeV). The general pattern of the observed failures indicates that as nuclear plants age and neutron fluence increases, various apparently nonsensitized austenitic SSs become susceptible to intergranular failure. Some components (e.g., BWR control blade handle and sheath) are known to have cracked under minimal applied stress. Although most failed components can be replaced, some safety-significant structural components (e.g., BWR top guide, shroud, and core plate) would be very difficult or impractical to replace. Therefore, the structural integrity of these components after accumulation of high fluence has been a subject of concern, and extensive research has been conducted to provide an understanding of this type of degradation, which is commonly known as irradiation-assisted stress corrosion cracking (IASCC).

In the mid-1960s, investigators began to implicate impurities such as Si, P, and S in IASCC failure of components fabricated from solution-annealed nonsensitized austenitic SS. However, in direct contradiction of the earlier beliefs and initially encouraging test results obtained from high-purity (HP) Type 348 austenitic SSs, investigators in recent years have found that resistance of HP heats of Type 304 and 348 SS (low in Si, C, P, and S contents) to IASCC failure is no better than that of commercial-purity (CP) materials, based on results from SSRT and in-reactor tests. Thus, the mechanisms of IASCC appear to be far from established.

In general, heat-to-heat variation in susceptibility to IASCC has been observed to be very significant regardless of material grade, even among similar HP materials containing virtually identical chemical compositions. This seems to cast serious doubt not only on the role of grain-boundary segregation of impurities (i.e., Si, P, or S) but also on the premise that Cr depletion is the only important mechanism of IASCC. Although significant grain-boundary Cr depletion is believed by most investigators to play a role, it has been suspected that other important process of IASCC of solution-annealed materials may be associated with other impurity elements (e.g., trace impurities) that are not specified in the ASTM specifications and that have been overlooked by most investigators. Trace elements are typically associated with iron- and steelmaking processes and with fabrication and welding of actual reactor components. Some investigators suspect that hydrogen plays an important role through a yet-to-be-identified synergism in the process of IASCC, and other investigators suspect that degree of metastability of various heats of austenitic SS plays an important role via a yet-to-be-identified process.

In the present reporting period, our primary effort has been focused on determining the effects of water chemistry on susceptibility to IASCC of BWR components irradiated in several BWRs. Effects of DO over the range <0.002 to ≈8 ppm in simulated BWR water at 289°C on IASCC were determined in slow-strain-rate-tensile (SSRT) tests on several heats of HP and CP Type 304 SS specimens from neutron-absorber rod tubes and a control-blade sheath irradiated to fluences to 2.4 x 10^{21} n·cm^{-2} (E > 1 MeV). The dependence of intergranular stress corrosion cracking (IGSCC) on DO was somewhat different for the HP and CP materials. Percent IGSCC on the fracture surface of HP heats was less influenced by DO and was higher than that of CP material for all DO and fluence levels. IGSCC of CP material was negligible for a DO <0.01 ppm or an ECP <-140 mV SHE. Grain-boundary compositions of alloying and

impurity elements determined by Auger electron spectroscopy (AES) were correlated with susceptibility of the BWR components to IASCC.

4.1 Effects of Water Chemistry on IGSCC of Irradiated Austenitic SSs

(H. M. Chung, W. E. Ruther, and A. G. Hins)

4.1.1 Introduction

The observation that IGSCC of nonirradiated thermally sensitized material and irradiated solution-annealed material exhibit a similar dependence on DO (e.g., see Ref. 32) has convinced many investigators that grain-boundary Cr-depletion is the dominant mechanism for IASCC. However, the data base for effects of water chemistry on IASCC is sparse; in particular for BWR-irradiated components fabricated from CP-grade Type 304 SS.[33-35] Results from a limited number of SSRT tests suggest that the threshold electrochemical potential (ECP) and DO to protect against IASCC are <-140 mV SHE[33] and <0.01 ppm,[34,35] respectively, for CP-grade Type 304 SS components. Threshold values obtained from uniaxial constant-load tests[36] were consistent with the SSRT results.

However, results of SSRT tests on BWR-irradiated rod-shape tensile specimens fabricated from numerous CP and HP heats of Types 304 and 316 SS indicate significant heat-to-heat variations in not only susceptibility to IASCC but also in its dependence on water chemistry.[37] We have also reported a strong heat-to-heat variation in IGSCC susceptibility of BWR components fabricated from several HP and CP heats of Type 304 SS at a single water chemistry, i.e., DO of ≈0.3 ppm and ECP of ≈60-150 mV SHE.[38,39] In this study, the effects of water chemistry were investigated for a wider range of DO (≈0.001 to ≈8 ppm) and ECP (-600 to +300 mV SHE). The objective was twofold: (1) to better define the effects of water chemistry on susceptibility of HP and CP Type 304 SS BWR components to IASCC, and thereby provide an independent confirmation of the protection potential, and (2) to provide insight into the origin of significant heat-to-heat variation in susceptibility to IASCC. Initial results of the investigation were reported previously.[40] Additional SSRT results and a correlation of IGSCC susceptibility with grain-boundary microchemistry are presented.

4.1.2 Experimental Procedures

Materials and Irradiation

A description and procedures for hot-cell SSRT tests were given in a previous report.[40] Cylindrical SSRT specimens of 89-mm length were sectioned from top-, middle-, and bottom-axial positions of the BWR neutron absorber rods listed in Table 14. Boron carbide was removed with an impact/rotary drill. The fast neutron fluence and chemical composition of the three HP and two CP heats of Type 304 SS are also given in Table 14. The fast (E > 1 MeV) neutron fluence of the HP and CP heat neutron-absorber tube specimens irradiated in four different BWRs ranged from 0.2-2.6 x 10^{21} n·cm^{-2}.

SSRT Tests

SSRT tests were conducted in air (Table 15) and in simulated BWR water containing DO of ≈8 ppm (Table 16), ≈0.3 ppm (Table 17), ≈0.02 ppm (Table 18), and <0.003 ppm (Table 19) at 289°C at a fixed strain rate of 1.65 x 10^{-7} s^{-1}. Dissolved-oxygen content in water was

Table 14. Chemical composition (in wt.%) and fluence of HP and CP Type 304 SS BWR components

Heat ID No.	Cr	Ni	Mn	C	N	B	Si	P	S	Source Code	Service Reactor	Fluence (10^{21} n·cm^{-2})
HP304-A	18.50	9.45	1.53	0.018	0.100	<0.001	<0.03	0.005	0.003	NAT[a]	BWR-B	0.2-1.4
HP304-B	18.30	9.75	1.32	0.015	0.080	<0.001	0.05	0.005	0.005	NAT[a]	BWR-B	0.2-1.4
HP304-CD	18.58	9.44	1.22	0.017	0.037	0.001	0.02	0.002	0.003	NAT[a]	BWR-B	0.2-1.4
HP304-CD	18.58	9.44	1.22	0.017	0.037	0.001	0.02	0.002	0.003	NAT[a]	BWR-QC	2.0
CP304-A	16.80	8.77	1.65	0.08[b]	0.052	-	1.55	0.045[b]	0.030[b]	NAT[c]	BWR-Y	0.2-2.0
CP304-B	18-20	8-10.5	2.00[b]	0.08[b]	-	-	1.00[b]	0.045[b]	0.030[b]	CBS[d]	BWR-LC	0.5-2.6

[a]High-purity neutron absorber tubes, OD = 4.78 mm, wall thickness = 0.63 mm, composition before irradiation.
[b]Represents maximum value in the specification; actual value not measured.
[c]Commercial-purity absorber tubes, OD = 4.78 mm, wall thickness = 0.79 mm, composition after irradiation.
[d]Commercial-purity control blade sheath, thickness 1.22 mm, actual composition not measured.

controlled by purging deaerated feedwater with a mixture of nitrogen and oxygen gases and was measured at the effluent side by the Chemetric™ color-matching technique. Effluent ECP values were determined by sequential measurements on working electrodes of nonirradiated Type 304 SS and platinum. The reference electrode located at the outlet of the autoclave was 0.1M KCl/AgCl/Ag. When the stainless steel ECP was stabilized, then SSRT test was initiated. During the test, ECP was measured periodically until the specimen fractured. For most of the tests, ECP remained fairly constant; however, a gradual increase in ECP by as much as ≈30% was observed in some tests. For each SSRT test, average ECP and DO, conductivity, and pH of the feedwater are listed in Tables 16–19.

Table 15. Results of tensile tests[a] in air on irradiated Type 304 SS BWR core-internal components at 289°C

Source Heat[b] Ident. No.	Fast-Neutron Fluence (n·cm^{-2})	Hot Cell Ident. No.	Specimen Ident. No.	SSRT No.	Tensile Properties: Failure Time (h)	Max. Stress (MPa)	Yield Stress (MPa)	Total Elong. (%)	IG (%)
CP304-A	2.0×10^{21}	389E3A	BL-BWR-2H	IR-9	228	631	595	13.5	0
CP304-A	0.6×10^{21}	389E2D	BL-BWR-2M	IR-3	580	465	221	34.8	0
CP304-A	0.2×10^{21}	389E1A	BL-BWR-2L	IR-2	260	390	184	15.6	0
HP304-A	1.4×10^{21}	406A1F	VH-A7A-L2	IR-5	93	786	702	5.6	0
HP304-CD	0.7×10^{21}	406C3	VM-D5B-L2	IR-6	405	684	591	24.2	0
HP304-A	0.2×10^{21}	406B3	VL-A4C-L2	IR-10	231	607	460	13.7	0
CP304-B	2.45×10^{21}	LSC-1	C71U	IR-15	123	830	820	7.3	0
CP304-B	2.54×10^{21}	LCS-4	C72T	IR-13	121	876	815	7.2	0
CP304-B	1.59×10^{21}	LSC-7	C7T1T	IR-19	203	792	666	12.0	0
CP304-B	1.17×10^{21}	LCS-9	C7T1M7	IR-21	136	777	736	7.5	0
CP304-B	0.53×10^{21}	LSC-11	C7M2K	IR-23	361	644	570	21.4	0
CP304-B	0.23×10^{21}	LCS-5	C7B1W	IR-17	574	577	360	34.1	0

[a]Tests in air at 289°C and strain rate of 1.65×10^{-7} s^{-1}.

Post-Test Examination

The fracture surfaces of SSRT specimens were analyzed by scanning electron microscopy (SEM) to determine quantitatively the fraction of intergranular (IG) fracture morphology

Table 16. SSRT[a] test results on irradiated HP and CP Type 304 SS BWR neutron-absorber tubes in HP water containing ≈8 ppm DO at 289°C

Source Heat Ident. No.	Fast-Neutron Fluence ($n \cdot cm^{-2}$)	α-γ hot cell Ident. No.	Swagelok Ident. No.	SSRT No.	Feedwater Chemistry: Oxygen Conc. (ppm)	Feedwater Chemistry: Average ECP (mV SHE)	Feedwater Chemistry: Cond. at 25°C ($\mu S \cdot cm^{-1}$)	Feedwater Chemistry: pH at 25°C	SSRT Parameters: Failure Time (h)	SSRT Parameters: Max. Stress (MPa)	SSRT Parameters: Total Elong. (%)	SSRT Parameters: TGSCC (%)	SSRT Parameters: IGSCC (%)
HP304-A	1.4×10^{21}	A6A2-1	32	IR-41	8.3	+156	0.120	6.35	31.9	414	1.90	2	56
HP304-A	1.4×10^{21}	A6A2-2	33	IR-42	8.2	+267	0.118	6.48	31.9	372	1.89	3	68
HP304-B	1.4×10^{21}	473A-1	47	IR-43	8.9	+165	0.118	6.49	31.8	453	1.88	0	59
HP304-CD	1.4×10^{21}	473C-1	42	IR-44	8.2	+122	0.084	6.80	29.2	360	1.73	3	62
HP304-B	0.7×10^{21}	473D-1	38	IR-53	8.2	+155	0.119	6.49	55.8	445	3.3	–	–
CP304-A	0.2×10^{21}	389C1-1	28	IR-51	8.0	+164	0.098	6.09	153.0	310	9.1	47	0
CP304-A	0.6×10^{21}	389C2-1	20	IR-45	8.2	+131	0.083	6.80	154.3	359	9.2	55	2
CP304-A	2.0×10^{21}	389C3-2	27	IR-52	7.9	+178	0.066	7.06	43.5	390	2.6	3	52

[a]Strain rate of $1.65 \times 10^{-7}\ s^{-1}$.

Table 17. SSRT[a] test results on irradiated Type 304 SS BWR core-internal components in simulated BWR water containing ≈0.3 ppm DO at 289°C

Source Heat Ident. No.	Fast-Neutron Fluence ($n \cdot cm^{-2}$)	α-γ Hot Cell Ident. No.	Specimen Ident. No.	SSRT No.	Feedwater Chemistry: Oxygen Conc. (ppb)	Feedwater Chemistry: Average ECP (mV SHE)	Feedwater Chemistry: Cond. at 25°C ($\mu S \cdot cm^{-1}$)	Feedwater Chemistry: pH at 25°C	SSRT Parameters: Failure Time (h)	SSRT Parameters: Max. Stress (MPa)	SSRT Parameters: Total Elong. (%)	SSRT Parameters: TGSCC (%)	SSRT Parameters: IGSCC (%)
CP304-A	2.0×10^{21}	389E3D	BL-BWR-2H	IR-12	300	90	0.13	6.27	21	415	1.2	8	28
CP304-A	0.6×10^{21}	389E2A	BL-BWR-2M	IR-8	290	76	0.15	6.32	140	359	8.3	55	0
CP304-A	0.2×10^{21}	389E1D	BL-BWR-2L	IR-1	280	115	0.13	6.23	107	337	6.7	43	0
HP304-A	1.4×10^{21}	406A1E	VH-A7A-L1	IR-4	280	106	0.10	6.28	11	417	0.6	2	58
HP304-CD	0.7×10^{21}	406C2	VM-D5B-L1	IR-7	280	148	0.12	6.26	31	552	1.8	8	34
HP304-A	0.2×10^{21}	406B2	VL-A4C-L1	IR-11	330	88	0.14	6.33	77	520	4.6	47	14
CP304-B	2.26×10^{21}	LSC-2	C71X	IR-16	310	–	0.12	6.23	74	841	4.2	2	3
CP304-B	2.64×10^{21}	LCS-3	C72S	IR-14	320	–	0.11	6.25	84	843	5.0	2	4
CP304-B	1.53×10^{21}	LCS-8	C7T1J	IR-20	360	–	0.11	6.22	101	872	6.1	3	6
CP304-B	1.15×10^{21}	LSC-10	C7T1M8	IR-22	360	–	0.11	6.28	79	815	4.7	5	4
CP304-B	0.50×10^{21}	LCS-12	C7M2L	IR-24	325	–	0.08	6.38	290	657	18.1	0	0
CP304-B	0.20×10^{21}	LSC-6	C7B1X	IR-18	310	–	0.11	6.24	457	572	27.1	8	0

[a]Strain rate of $1.65 \times 10^{-7}\ s^{-1}$.

Table 18. SSRT[a] test results on irradiated HP and CP Type 304 SS BWR neutron-absorber tubes in HP water containing ≈0.02 ppm DO at 289°C

Source Heat Ident. No.	Fast-Neutron Fluence ($n \cdot cm^{-2}$)	α-γ Hot Cell Ident. No.	Swagelok Ident. No.	SSRT No.	Feedwater Chemistry: Oxygen Conc. (ppm)	Feedwater Chemistry: Average ECP (mV SHE)	Feedwater Chemistry: Cond. at 25°C ($\mu S \cdot cm^{-1}$)	SSRT Parameters: pH at 25°C	SSRT Parameters: Failure Time (h)	SSRT Parameters: Max. Stress (MPa)	SSRT Parameters: TGSCC (%)	SSRT Parameters: IGSCC (%)
HP304-B	1.4×10^{21}	B6A2-3	49	IR-59	0.023	-28	0.063	7.06	71.6	833	–	–
CP304-A	2.0×10^{21}	389D3-1	24	IR-58	0.015	-265	0.063	7.06	89.1	607	7	2

[a]Strain rate of 1.65×10^{-7} s^{-1}.

Table 19. SSRT[a] test results on irradiated HP and CP Type 304 SS BWR neutron-absorber tubes in HP water containing <0.003 ppm DO at 289°C

Source Heat Ident. No.	Fast Neutron Fluence ($n \cdot cm^{-2}$)	α-γ Hot Cell Ident. No.	Swagelok Ident. No.	SSRT No.	Feedwater Chemistry: Oxygen Conc. (ppm)	Feedwater Chemistry: Average ECP (mV SHE)	Feedwater Chemistry: Cond. at 25°C ($\mu S \cdot cm^{-1}$)	Feedwater Chemistry: pH at 25°C	SSRT Parameters: Failure Time (h)	SSRT Parameters: Max. Stress (MPa)	SSRT Parameters: Total Elong. (%)	SSRT Parameters: TGSCC (%)	SSRT Parameters: IGSCC (%)
HP304-CD	1.4×10^{21}	473C-2	43	IR-55	0.001	-413	0.062	7.20	95.2	725	5.7	10	7
HP304-B	1.4×10^{21}	473A-2	48	IR-54	0.001	-567	0.062	7.20	103.1	757	6.1	8	6
HP304-CD	1.4×10^{21}	473B-1	44	IR-56	<0.003	-319	0.061	7.47	66.4	703	3.9	7	18
CP304-A	2.0×10^{21}	389F3-1	40	IR-57	<0.002	-409	0.062	7.47	115.5	654	6.9	8	2
CP304-A	2.0×10^{21}	389F3-2	39	IR-510	0.001	-395	0.062	7.01	97.4	661	5.8	–	–

[a]Strain rate of 1.65×10^{-7} s^{-1}.

(percent IGSCC). Fractography by SEM was conducted at a magnification of ≈125X, and an entire fracture-surface composite was constructed for each specimen to determine the fractions of IG, transgranular (TG), and ductile failure. Stereo fractographs at a magnification of 300–500X were obtained from several regions of IG fracture to determine three-dimensional topography of the fracture surface. Grain-boundary microchemistry was analyzed with a JEOL Company JAMP-10 Model scanning Auger microscope (SAM) on specimens charged with hydrogen and fractured in-situ in the ultrahigh vacuum of SAM.[38,39] Regions of IG fracture in several SSRT specimens were selected and sputtered with Ar ions to conduct depth-profile analyses of impurities beneath the IG fracture surface.

4.1.3 Results

Susceptibility to IGSCC

In Fig. 30, effects of DO on percent IGSCC are shown for HP (HP304-A, B, and CD) and CP (CP304-A) neutron-absorber tubes irradiated to ≈1.4–2.0 x 10^{21} n·cm^{-2}. Percent IGSCC vs. DO (≈0.02–32 ppm) for CP Type 304 SS dry tubes, reported by Kodama et al.,[34,35] are also shown in Fig. 30 for comparison. The results for two types of BWR tubes fabricated from CP Type 304 SS and irradiated to ≈1.3–2.0 x 10^{21} n·cm^{-2}, i.e., neutron-absorber tubes in this study and dry tubes in the work of Kodama et al., appear to be quite similar. A strong effect of water chemistry is evident for all types of BWR components shown in Fig. 30.

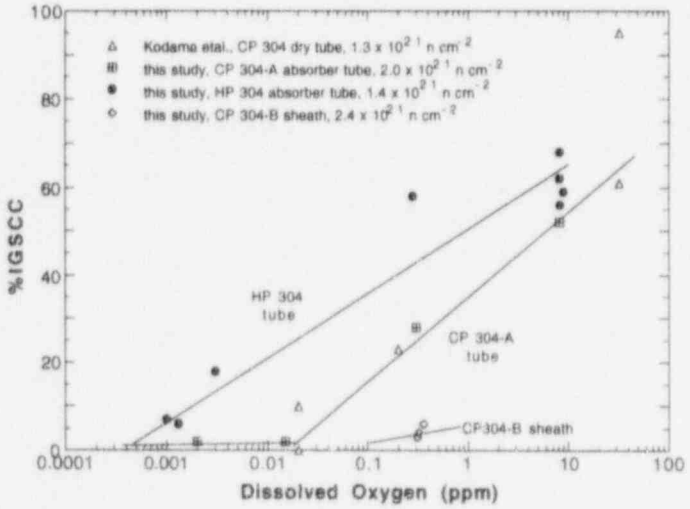

Figure 30.
Percent IGSCC vs. DO for HP and CP Type 304 SS neutron-absorber tubes (this study) and CP Type 304 SS dry tubes (Kodama et al.). Three distinct trends in DO dependence are evident.

However, the dependence of percent IGSCC on DO for neutron-absorber tubes fabricated from HP heats appears to be different from those of the tubes fabricated from CP materials in several aspects. Namely, for a comparable fluence level, susceptibility of the HP absorber tubes to IGSCC seems to be less dependent on DO than the CP tubes; however, IGSCC susceptibility of the HP absorber tubes seems to be significantly higher than for the CP absorber tubes regardless of DO and fluence levels.

Similar trends are also obvious from Fig. 31, in which the dependence of percent IGSCC on ECP is shown for data obtained from BWR components irradiated to fluences of ≈1.4–2.4 x 10^{21} n·cm^{-2}. In the figure, results obtained for CP 304 SS by Indig et al.[33] (BWR sheet, fluence ≈1.9 x 10^{21} n·cm^{-2}) and in the present investigation (BWR absorber tube, fluence

≈2.0 x 10^{21} n·cm^{-2}) appear to be comparable, whereas the degree of IG cracking of HP 304 SS absorber tubes does not decrease as rapidly with a decrease in ECP as for the CP materials.

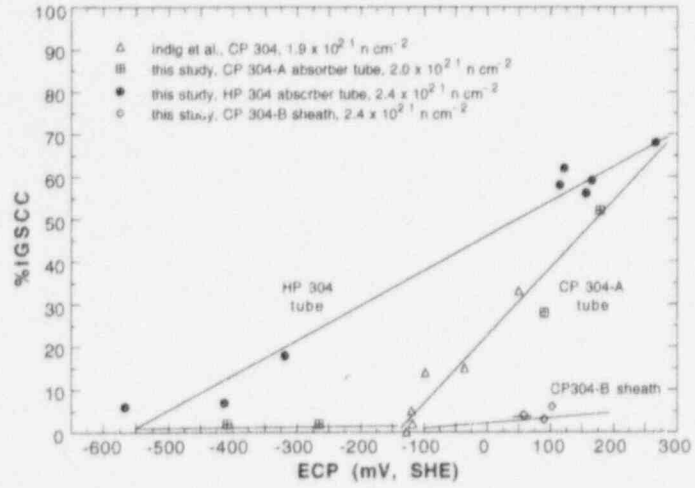

Figure 31.
Percent IGSCC vs. ECP of HP and CP Type 304 SS neutron-absorber tubes (this study) and CP Type 304 SS BWR sheet material (Indig et al.)

Figure 32 shows the dependence of ECP of a Type 304 SS versus an 0.1M KCl/AgCl/Ag electrode located at the effluent of a small SSRT autoclave on DO concentration in the simulated BWR water. The present data lie within the two lines in the figure that encompass similar results from tests on nonirradiated Type 304 SS.

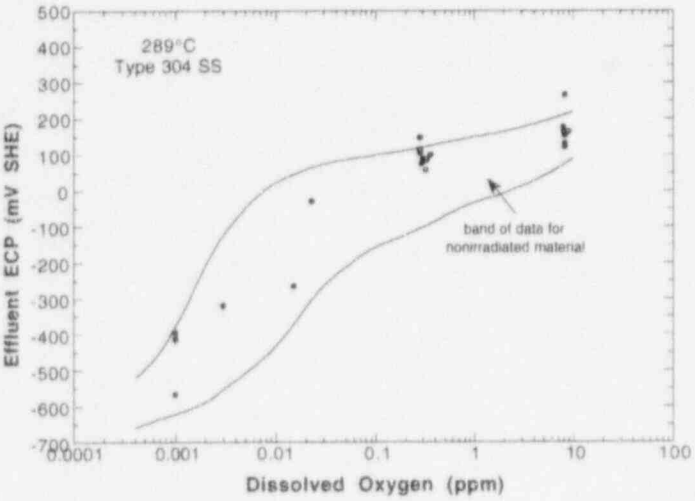

Figure 32.
ECP vs. DO measured in this study. Band of similar data reported from tests of non-irradiated sensitized materials is shown for comparison.

Approximate Crack Growth Rate

An intergranular CGR was estimated from the SSRT data by a procedure similar to that of Jenssen and Ljungberg.[37] In the present study, the rate was estimated only for neutron-absorber tube specimens in which a through-wall IG crack had been confirmed by SEM fractography. For such specimens, the depth and time of IG crack propagation can be determined fairly accurately from the fracture-surface map and load-elongation curve, respectively. CGRs determined by this method are listed in Table 20 and plotted as a function of ECP in Fig. 33. Values determined from SSRT data of Jenssen and Ljungberg[37] and Kodama et al.,[34,35] and constant-load data of Katsura et al.[36] are also shown in the figure.

Table 20. Intergranular CGR from SSRT tests on irradiated Type 304 and 316 SS BWR core-internal components in simulated BWR water at 289°C

Source Heat Ident. No.	Fast Neutron Fluence ($n \cdot cm^{-2}$)	SSRT No.	Feedwater Chemistry: Oxygen Conc. (ppm)	Feedwater Chemistry: Ave. ECP (mV SHE)	SSRT Parameters: Failure Time (h)	SSRT Parameters: IGSCC (%)	SSRT Parameters: Max. IGSCC Penetration (%)	SSRT Parameters: IGSCC Depth (mm)	SSRT Parameters: Intergranular CGR (10^{-8} m·s^{-1})
CP304-A[a]	2.0×10^{21}	IR-12	0.30	90	21.0	28	100	0.79	1.04
CP304-A	2.0×10^{21}	IR-52	7.9	178	43.5	52	100	0.79	0.51
HP304-A[b]	1.4×10^{21}	IR-4	0.28	106	11.2	58	100	0.63	1.56
HP304-CD	0.7×10^{21}	IR-7	0.28	148	31.0	34	100	0.63	0.56
HP304-A	1.4×10^{21}	IR-41	8.3	156	31.9	56	100	0.63	0.55
HP304-A	1.4×10^{21}	IR-42	8.2	267	31.9	68	100	0.63	0.55
HP304-B	1.4×10^{21}	IR-43	8.9	165	31.8	59	100	0.63	0.54
HP304-CD	1.4×10^{21}	IR-44	8.2	122	29.2	62	100	0.63	0.60

[a]Commercial-purity Type 304 SS, wall thickness 0.63 mm, tested at a strain rate of 1.65×10^{-7} s^{-1}.
[b]High-purity Type 304 SS, wall thickness 0.79 mm, tested at a strain rate of 1.65×10^{-7} s^{-1}.

Results in Fig. 33 indicate that intergranular CGRs estimated from SSRT and constant-load tests on BWR components are similar ($\approx 1 \times 10^{-8}$ m·s^{-1}) for a similar range of fluence and ECP. In the work of Indig et al.,[33] the exact depth of IG penetration in the specimens was not reported; consequently, estimates of CGRs similar to those in Table 20 cannot be made. A CGR of $\approx 1 \times 10^{-8}$ m·s^{-1} was estimated based on SSRT data given in Ref. 33. However, the CGRs obtained from SSRT data of Jenssen and Ljungberg for BWR-irradiated rod-shape specimens[37] are lower by more than an order of magnitude than those estimated from specimens sectioned from BWR components.

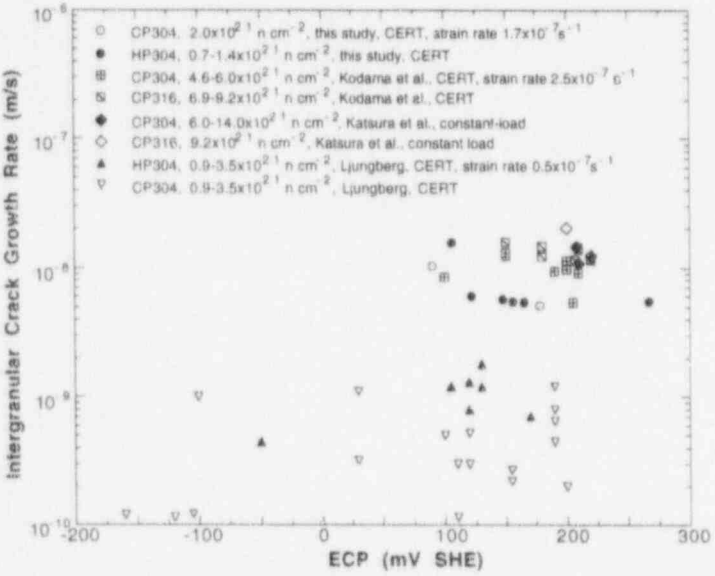

Figure 33. Intergranular crack growth rate vs. ECP determined from SSRT and constant-load tests on BWR tube components and rod-tensile specimens irradiated in BWR

The strain rate in the investigation of Jenssen and Ljungberg[37] was significantly lower (i.e., 5×10^{-8} s^{-1}) than in the work of Kodama et al. (2.5×10^{-7} s^{-1}) and in the present investigation (1.7×10^{-7} s^{-1}). According to a correlation between CGR and crack-tip strain rate for nonirradiated sensitized Type 304 SS developed by Andresen and Ford,[32] this increase in strain rate would produce higher CGRs by factors of ≈1.5–2. Indig et al.[33] reported minimal effects of strain rate (3.7×10^{-7} – 1.8×10^{-7} s^{-1}) on IASCC of irradiated BWR components

(percent IGSCC vs. ECP shown in Fig. 31). Therefore, we believe that strain rate alone cannot account for the large difference in CGRs shown in Fig. 33.

However, the effect of stress intensity on CGRs of nonirradiated sensitized Type 304 SS has been reported to be far more significant.[32] At this time, it is not clear whether CGRs of reactor component materials are more dependent on component fabrication variables and differences in irradiation conditions than on factors such as stress intensity and strain rate. Stress intensity is not likely to have been comparable in these tests, and a more accurate comparison would be possible if CGRs were obtained under conditions of constant stress intensity.

4.1.4 Discussion

Threshold ECP

A threshold ECP of <–140 mV SHE to suppress IASCC in the CP material is consistent with the results of Indig et al.[33] However, the contrasting dependence of IGSCC of HP and CP materials on water chemistry (DO and ECP) was unexpected. To obtain a better understanding of the peculiar behavior of HP neutron-absorber tubes, grain-boundary microchemistry determined by AES was correlated with the IGSCC susceptibility of material irradiated to 1.4–2.4 x 10^{21} n·cm^{-2} and tested in simulated BWR water containing ≈0.3 and 8 ppm DO (Tables 17 and 16, respectively). The results, some of which have been reported elsewhere,[38,39,41] are summarized in Figs. 34–39.

Role of Cr Depletion

The HP-grade neutron absorber tubes are characterized by more pronounced grain-boundary Cr depletion than that in the CP-grade absorber tubes or sheath. This is shown in Fig. 34 in which the percent IGSCC of three BWR components, irradiated to a comparable fluence level (1.4–2.4 x 10^{21} n·cm^{-2}), is plotted as a function of grain-boundary Cr concentration. We believe the lower grain-boundary Cr concentration in HP materials is associated with a higher susceptibility to IASCC. However, it is difficult to explain the contrasting behavior of HP and CP materials to water chemistry solely on the basis of grain-boundary Cr depletion. Likewise, it is also difficult to explain certain important and well-known characteristics of IASCC on the basis that grain-boundary depletion of Cr plays a primary role, e.g., a strong heat-to-heat variation in susceptibility among heats of virtually identical chemical composition[42] and the significant cracking susceptibility observed after irradiation at lower temperatures of ≈50[43] and ≈200°C.[44]

Role of Ni

A higher Ni concentration on grain boundaries appears to be conducive to suppression of IASCC (Fig. 35). This is qualitatively consistent with an observation reported by Cookson et al.[44] It seems that a lower Ni concentration tends to increase metastability of grain boundaries in austenitic SSs.

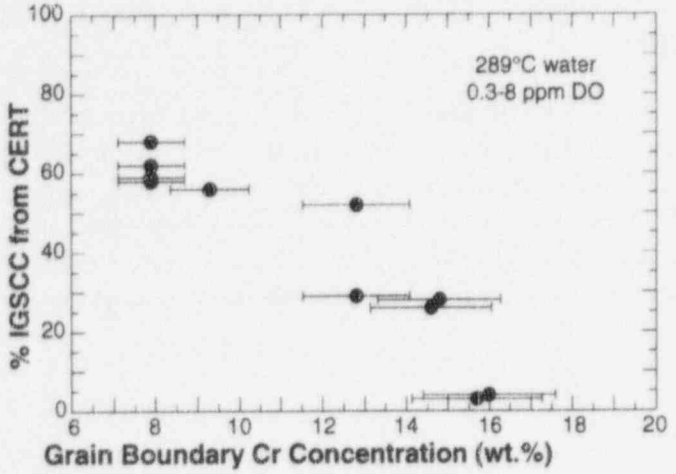

Figure 34.
Percent IGSCC at ≈0.3–8 ppm DO vs. grain-boundary Cr concentration determined by AES for HP and CP Type 304 SS BWR components irradiated to 1.4–2.4 x 10^{21} n·cm^{-2} (E > 1 MeV)

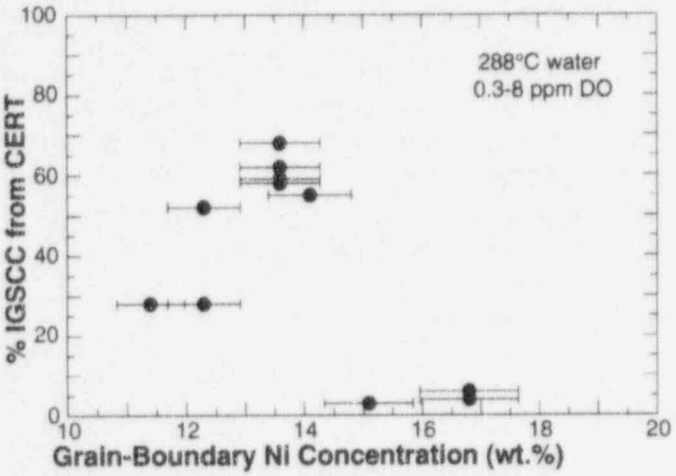

Figure 35.
Percent IGSCC vs. grain-boundary concentration of Ni

Role of Li and B

The results in Fig. 36 suggest that resistance to IASCC correlates well with intensities of Auger electrons that give rise to a characteristic peak at 58 eV (i.e., secondary peaks of Ni and Li). The origin of the peak, which exhibited a characteristic shape similar to that of Li but different from that of Ni, was examined extensively in a previous report.[39] From the examination, it was concluded that at least some portion of the peak height was produced by Li impurity contained in the irradiated BWR materials. Therefore, the results in Figs. 35 and 36 indicate that higher concentrations of Ni and Li, and hence B (which produces Li by transmutation by thermal neutrons), are beneficial in suppressing IASCC.

Role of N

We have reported evidence of grain-boundary segregation of N in neutron-absorber tubes fabricated from two heats of HP material (i.e., HP304-A and -CD) that were tested in this study.[39] In Fig. 37, susceptibility to IGSCC is plotted as a function of grain-boundary concentration of N in BWR-irradiated materials investigated in this study. Based on the figure, a higher concentration of N on grain boundaries seems to be deleterious to resistance to IASCC, a finding consistent with that reported by Kasahara et al.[45]

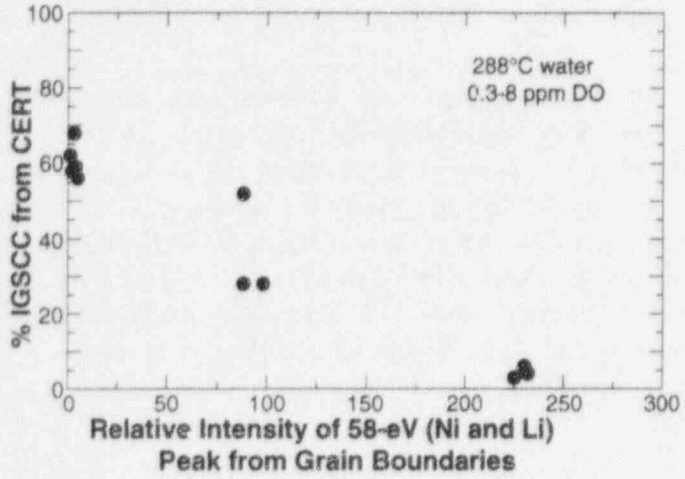

Figure 36.
Percent IGSCC vs. relative intensity of 58-eV peak of AES spectra (Li plus Ni) from grain boundaries

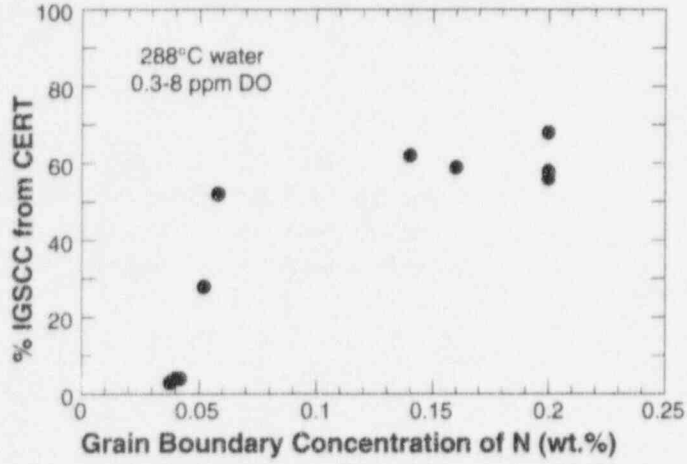

Figure 37.
Percent IGSCC vs. grain-boundary concentration of N

Role of V

Evidence of a correlation between IGSCC and V has been reported previously.[46] Figure 38 shows percent IGSCC of BWR materials investigated in this study as a function of relative concentration of V on grain boundaries. The figure indicates that a higher concentration of V on grain boundaries decreases resistance to IASCC.

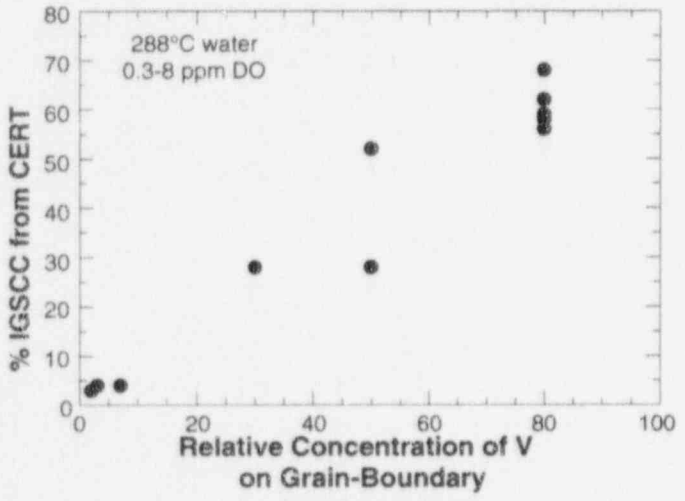

Figure 38.
Percent IGSCC vs. relative grain-boundary concentration of V

Role of F

The results in Fig. 39 indicate that a higher level of F on grain boundaries in HP absorber tubes (higher than in the CP tubes or sheath) is associated with higher susceptibility to IASCC.[41] Inadvertent contamination of reactor components by fluorine could occur during pickling (in a solution containing HF) in the case of tubular components such as neutron-absorber-rod tubes, and by an F-containing weld flux in the case of large welded components such as BWR core shrouds and certain older top guides. The deleterious effect of F on SCC appears to be consistent with the presence of F ions in water. Ward et al.[47] reported that F ions at concentrations of ≤1 ppm in water produced IG cracking to varying degrees in nonirradiated sensitized Types 304, 316, and 348 SS.

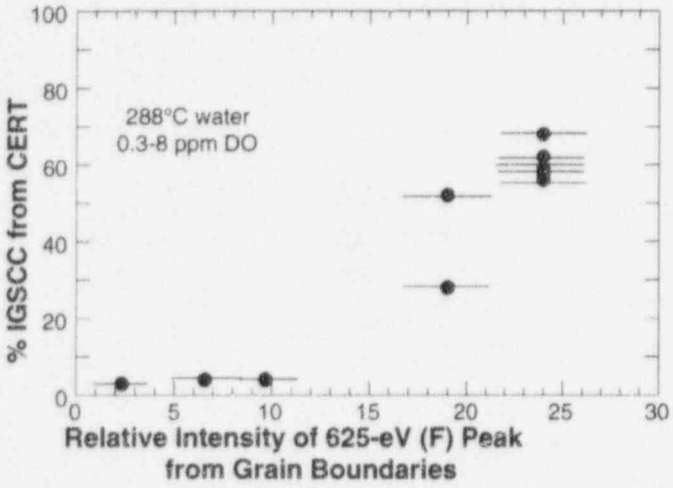

Figure 39.
Percent IGSCC vs. average intensity of fluorine signal from grain boundaries of HP and CP Type 304 SS BWR components

The HP absorber specimen that exhibited a surprisingly high susceptibility to IGSCC of ≈18% at a very low DO of ≈0.002 ppm (Fig. 30) and ECP of ≈–320 mV SHE (Fig. 31) was examined in detail by AES. The distribution of IG fracture-surface morphology of this specimen is shown schematically in Fig. 40. An IG region on the specimen (Spot D5 in the figure) was sputtered to a depth of ≈60 nm, and AES spectra were obtained as a function of depth from the IG fracture surface that was produced in 289°C water during an exposure period of ≈60 h. From the AES spectra, unexpected distributions of F, Ca, B, Zn, and Al were noticed (Fig. 41). The following can be deduced from the element distributions shown in the figure: (1) Al was used as a deoxidizer during melting of the HP-grade SS and Ca could have originated from CaF_2 that may have been used as flux in melting HP SS, (2) F is present intermittently near the IG fracture surface covered with ≈15-nm-thick oxide layer, (3) F, Ca, and Al near the fracture surface dissolved in water at 289°C, (4) the IG fracture surface picked up B and Zn from the water, and (5) there is no indication of clustering or interaction among the above elements. The observation of F in the region close to the IG fracture surface of Fig. 40 seems to be consistent at least with the results of Fig. 39.

DO and ECP Dependence of HP Tubes

Ward et al.[47] reported accelerated IGSCC of nonirradiated thermally sensitized bend specimens or weldments of CP-grade Type 304 SS that were contaminated with F. F-assisted IGSCC was less sensitive to DO than was classical IGSCC of thermally sensitized F-free specimens, which is similar to the IGSCC dependence of HP neutron-absorber tubes on DO

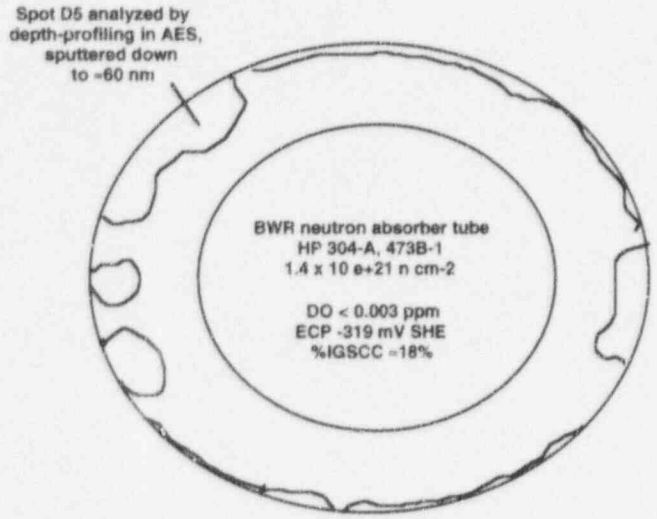

Figure 40.
Distribution of IG fracture in HP absorber tube irradiated to fluence of 1.4 x 10^{21} n·cm^{-2} after SSRT test at low DO and ECP of ≈0.002 ppm and −320 mV SHE, respectively

and ECP observed in the present investigation. In view of this similarity and the results of Fig. 39, the behavior of the HP absorber tubes can be best explained on the premise that in the case of a low DO and ECP, the concentration of Cr ions dissolved in water would be very low or negligible, and the catalytic role of F promotes anodic dissolution of Fe at the crack tip.[40] Under conditions of high DO and ECP, the concentration of Cr ions dissolved in water would be relatively high, and the catalytic effect of F could be suppressed because F ions in water will be trapped by formation of the nonlabile ligand complex $CrF(H_2O)_5$.[40]

Role of Inclusions

On fresh fracture surfaces produced in-situ in hydrogen-charged HP absorber-tube specimens in the ultrahigh vacuum environment of the scanning Auger microscope, numerous spherical inclusions ≈500 nm in diameter were observed, as shown in Fig. 42. Results of analysis by AES revealed two types of inclusions; MnS and CuS. The former was rich in V and F [(MnV)(SF)-type], and the latter was rich in Mo, V, Ca, F, C, and N [CuMoVCa)(SFCN)-type]. These sulfide inclusions, which apparently formed during the steelmaking process, seem to trap F in the material. This is shown more quantitatively in Fig. 43. Minor impurities that have low solubility (e.g., S and F) tend to segregate to grain boundaries or are scavenged by inclusions. Therefore, inclusions seem to play an important but indirect role by trapping both beneficial and detrimental impurities.

Numerous shallow cracks were observed perpendicular to the direction of tensile stress on the outer surface of the tube shown in Figs. 40 and 41 (Fig. 44A). At higher magnification mostly transgranular fracture was observed on the crack surface (Fig. 44B). Frequently, relatively large inclusions were also observed on surfaces of shallow cracks, indicating that initiation of brittle shallow cracks was promoted by inclusions. Analysis by AES showed that these inclusions are oxycarbides rich in Fe, Al, Ca, and S (Table 21). In some instances, a transition from transgranular to intergranular fracture occurs.

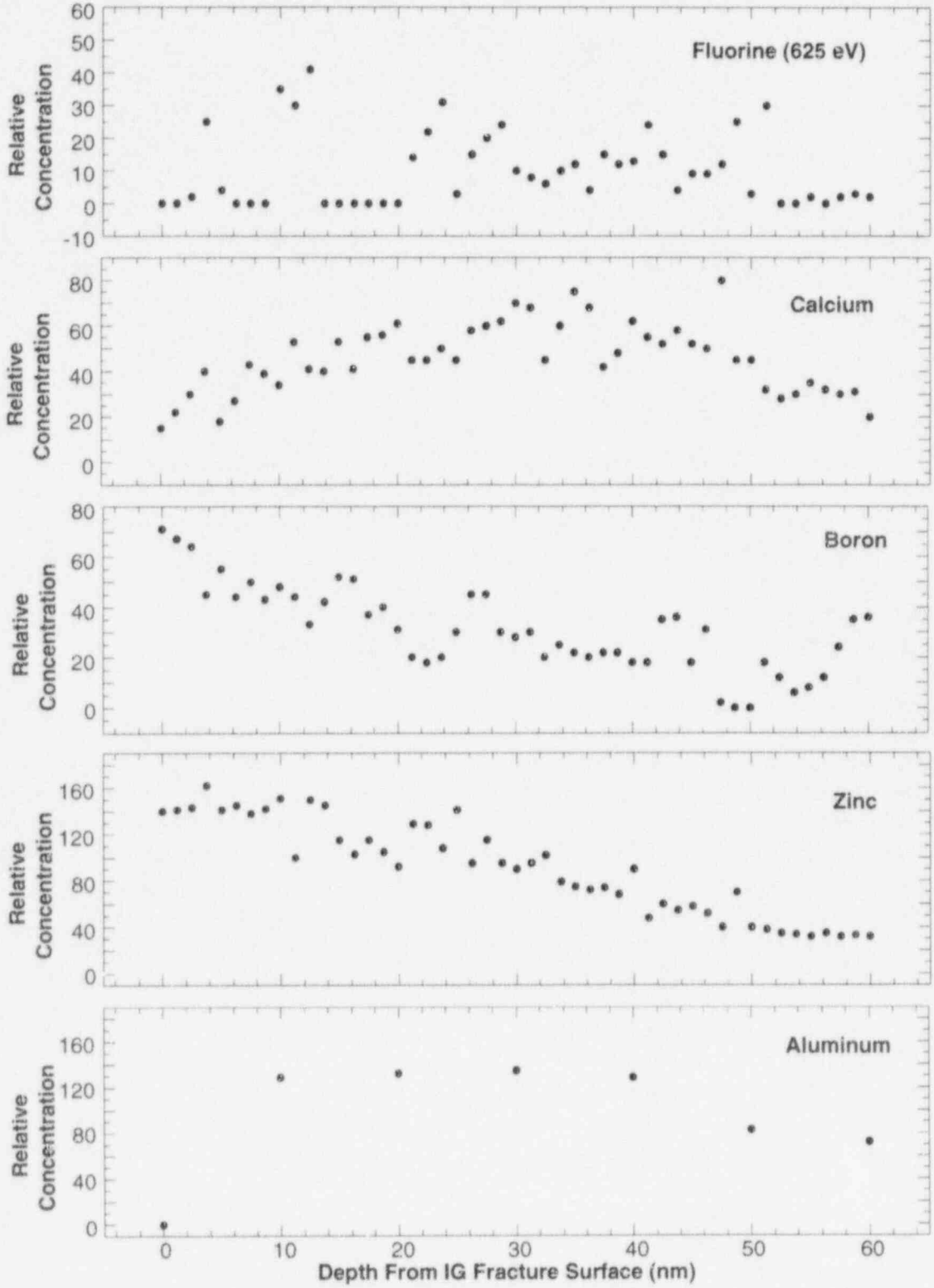

Figure 41. Distribution (from the top) of F, Ca, B, Zn, and Al as function of depth beneath IG fracture surface (Spot D5, Fig. 40) produced in HP Type 304 SS BWR absorber tube (473B-1, Table 19) during SSRT test in water containing ≈0.002 ppm DO at 289°C (IGSCC ≈18%)

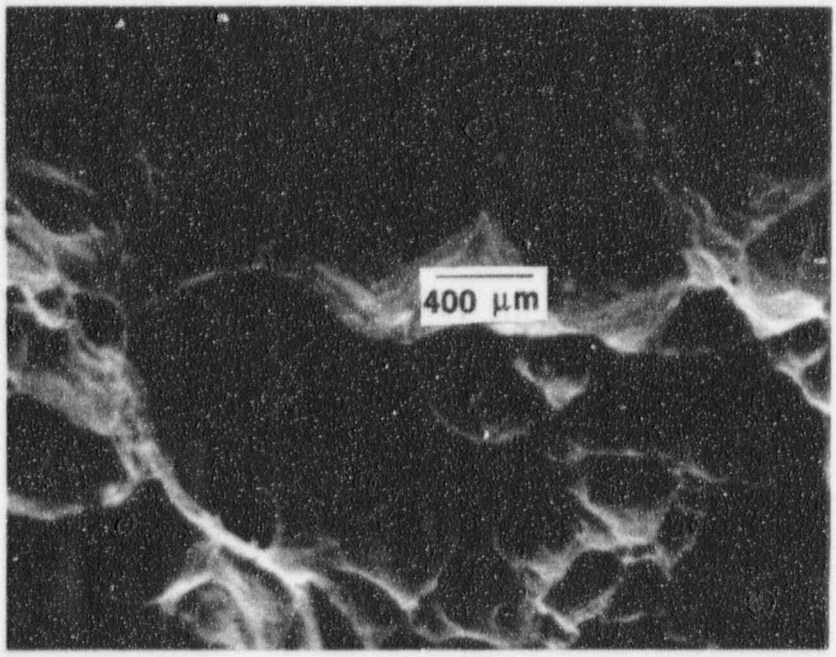

Figure 42. Spherical sulfide inclusions observed in HP absorber tubes irradiated to 1.4 x 10^{21} n·cm^{-2}

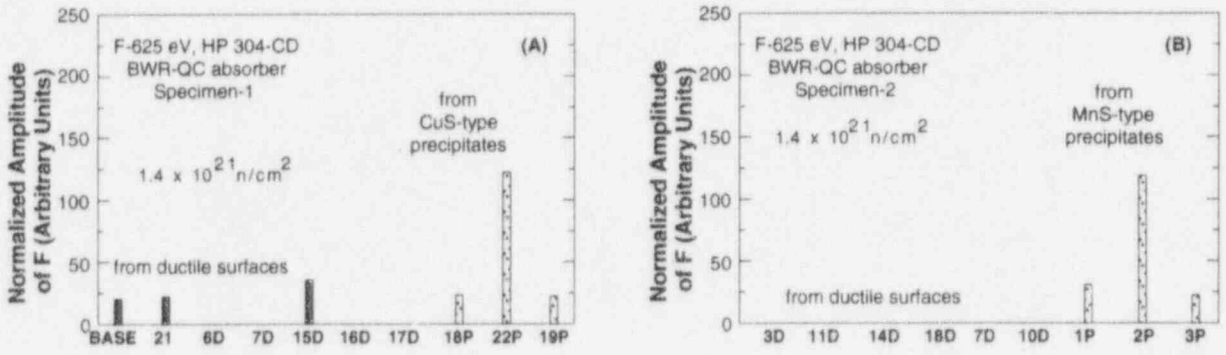

Figure 43. Relative concentrations of F from ductile fracture surfaces and from CuS (A) and MnS (B) type sulfides in HP absorber tubes irradiated to 1.4 x 10^{21} n·cm^{-2}

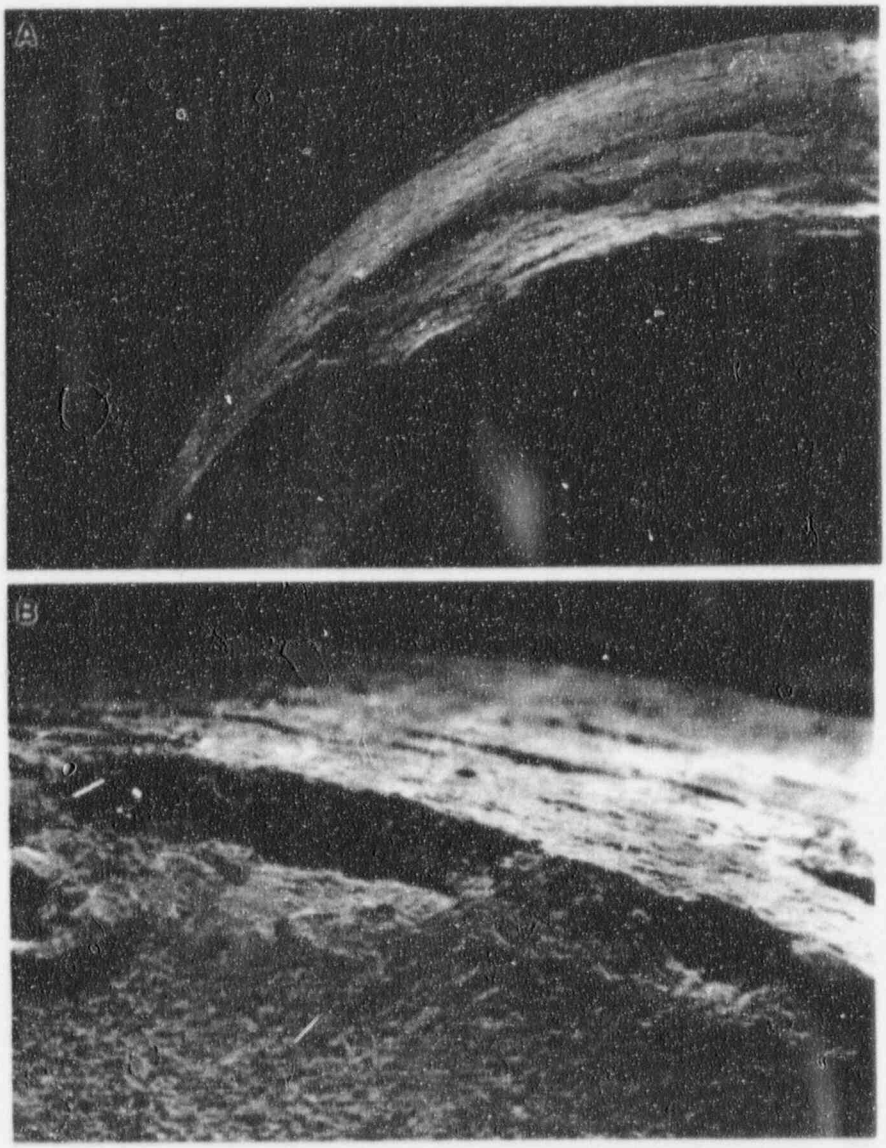

Figure 44. (A) Morphology of shallow cracks on outer surface of HP absorber tubes irradiated to 1.4 x 10^{21} n·cm^{-2} and tested in water containing ≈0.002 ppm DO and (B) inclusions associated with shallow outer surface cracks

Table 21. Composition (in at.%) determined by AES of inclusions in association with shallow outer surface cracks in Fig. 44(B)

Inclusion	S	C	Ca	O	Cr	Fe	Ni	Al
L1 before sputter	2	57	4	15	–	10	–	12
L1 after sputter	1	58	3	13	–	6	–	18
L4A	4	49	2	15		15	2	14
L4B	3	37	2	14	2	28	5	11
L4C	4	48	2	14	–	18	5	10
M1	4	34	1	12	4	23	7	16
M2	1	20	2	23		3	1	51

5 Summary of Results

5.1 Fatigue of Ferritic Steels

Fatigue behavior of A106–Gr B carbon steel and A533–Gr B and A302–Gr B low–alloy steels has been investigated in air and water environments. The results confirm the significant reduction in fatigue life in high–DO water and a strong dependence on strain rate. The results show that although the structure and cyclic–hardening behavior of carbon and low–alloy steels are distinctly different, there is little or no difference in susceptibility to environmental degradation of fatigue life of these steels, when sulfur levels are comparable. The A106–Gr B and A302–Gr B steels exhibit dynamic strain–aging, whereas strain–aging effects are modest in A533–Gr B low–alloy steel.

In air environment, fatigue life of carbon and low–alloy steels depends on temperature, strain rate, and sulfide morphology. Fatigue life in room–temperature air is either comparable to or slightly longer than in air at 288°C. Some heats exhibit an effect of strain rate; life decreases with decreasing strain rate. The A302–Gr B steel showed a strong effect of material orientation; relative to rolling direction, fatigue life in the transverse orientation is lower by a factor of ≈5 at 0.4%/s and a factor of ≈12 at 0.004%/s strain rate.

Environmental effects on fatigue life are significant when five conditions are satisfied simultaneously, viz., applied strain range is above a minimum threshold level, strain rate <1%/s, temperature ≥150°C, DO ≥0.05 ppm, and sulfur content in steel >0.003 wt.%. For both carbon and low–alloy steels, the results indicate only a marginal effect of simulated PWR environment on fatigue life, e.g., fatigue life is lower by a factor of ≤2 than that in air. Furthermore, fatigue life is independent of strain rate; a three–order–of–magnitude decrease in strain rate does not cause an additional decrease in life. The results also indicate that modest decreases of fatigue life in simulated PWR water are valid for high–sulfur steels (e.g., A302–Gr B steel with 0.027 wt.% S) that exhibit enhanced crack growth rates in precracked specimens. At room temperature, life in water is 30–50% lower than in air.

For high–DO water (0.5–0.8 ppm) the effects of various loading and environmental parameters on fatigue life of carbon and low–alloy steels are summarized below.

(i) A slow strain rate applied during the tensile–loading cycle is more effective in environmentally assisted reduction in fatigue life than when applied during the compressive–loading cycle. Also, a slow strain rate applied during both tensile– and compressive–loading cycles does not cause a further decrease in fatigue life.

(ii) Fatigue life decreases rapidly with decreasing strain rate. For the ANL heats of A106–Gr B and A533–Gr B steels, the effect of strain rate saturates at ≈0.001%/s.

(iii) A minimum strain is required for environmentally assisted decrease in fatigue life. For the loading conditions used in the present study, this threshold strain range appears to be ≈0.36% for the heats of carbon and low–alloy steels investigated.

(iv) The results also indicate that a slow strain rate applied during each portion of the tensile–loading cycle above the threshold strain is equally effective in decreasing fatigue life.

(v) A detailed metallographic examination of the test specimens and exploratory tests indicate that the reduction in fatigue life in high-DO water is primarily due to environmental effects on fatigue crack propagation. Environment appears to have little or no effect on crack nucleation. Although all specimens tested in water show surface micropitting, there is no indication that these micropits enhance crack nucleation. Irrespective of environment, cracks in carbon and low-alloy steels nucleate either along slip bands, at carbide particles, or on ferrite/pearlite phase boundaries.

5.2 Environmentally Assisted Cracking of Alloys 600 and 690 in Simulated LWR Water

Several heats of Alloy 600 and 690 were characterized for corrosion-fatigue testing. Tensile properties of cylindrical specimens were determined in air at 25, 290, and 320°C and Vickers hardness and average grains size were measured at room temperature. In general, the tensile properties at 25°C were consistent with those in certified material test reports supplied by vendors and documentation obtained from the Electric Power Research Institute, Palo Alto, CA, who provided 1-in.-thick plates of several heats for fabrication of compact-tension specimens. The dependence of yield stress of annealed Alloy 600 and 690 specimens on average grain size tends to follow a Petch relation, i.e., $\sigma_y = \sigma_i + k \cdot d^{-1/2}$, where σ_y is the yield stress, d the grain diameter, k an empirical constant, and σ_i the "friction" stress, which is a measure of intrinsic resistance of the material to dislocation motion.

Metallographic specimens were prepared to determine qualitatively the degree of grain-boundary carbide coverage by optical metallography. Specimens were polished to a diamond finish, and a Vickers hardness indentation was made to provide a reference point for subsequent examination after different chemical etching methods. Polished specimens were electroetched in a 10% H_3PO_4 solution and photographed at 500X to reveal carbides present in the material. Then the specimens were repolished and electroetched in a 5% nital solution and photographed at the same magnification and in the same location with the aid of the hardness indentation, primarily to reveal grain boundaries. The two microphotographs of each specimen provided a qualitative estimate of the extent of inter- and intragranular carbide precipitation. Five heats of Alloy 600 exhibited either semicontinuous or continuous carbide precipitation at grain boundaries plus a significant amount of intragranular carbide. Four heats of Alloy 690 revealed continuous precipitation of carbides at grain boundaries and relatively few intragranular carbides. According to published information, precipitate phases in Alloy 600 and 690 are Cr-rich M_7C_3 and $M_{23}C_6$ carbides and TiN.

Fracture-mechanics crack-growth-rate tests are being conducted at 289 and 320°C on compact-tension specimens of mill-annealed Alloy 600 and thermally treated Alloy 690 in oxygenated water and in deaerated water containing B, Li, and dissolved H_2 at low concentrations.

5.3 Irradiation-Assisted SCC of Type 304 SS

Effects of dissolved oxygen (DO) in water and electrochemical potential (ECP) on susceptibility of commercial-purity (CP) Type 304 SS BWR neutron-absorber tubes to IASCC in slow-strain-rate-tensile (SSRT) tests in simulated BWR water at 289°C were similar to those of other CP-grade Type 304 SS BWR components reported in a previous investigation.

Threshold values of DO and ECP to mitigate IASCC of CP-grade materials were confirmed, namely, <0.01 ppm and <-140 mV SHE, respectively.

Susceptibility to IASCC in SSRT tests on high-purity (HP) specimens of Type 304 SS fabricated from BWR components differed from that of CP materials. Namely, the susceptibility of HP heats was less dependent on water chemistry (DO and ECP). This can be explained best by the premise that at low DO and ECP, where the concentration of Cr ions dissolved in water should be negligible, the catalytic role of F promotes anodic dissolution of Fe at the crack tip. HP-grade neutron-absorber tubes were considerably more susceptible to IASCC than were CP tubes or control-blade sheaths; HP materials were characterized by lower concentrations of Cr, Ni, and Li and higher concentrations of F, V, and N on grain boundaries than those of CP-grade components, indicating that higher levels of Cr, Ni, and B and lower levels of F, V, and N in these steels tend to suppress IASCC. Inclusions in the materials formed during the steelmaking process can play an indirect but important role by trapping detrimental and beneficial impurities or by promoting crack initiation at surfaces in contact with water.

Intergranular crack growth rates estimated from our SSRT and constant-load tests on BWR-irradiated component materials are similar to those obtained at other laboratories, but the rates are significantly higher than those estimated from SSRT data on test specimens irradiated in BWRs. The origin of this discrepancy is not clear at present, although differences in stress intensity levels in the specimens may be an important factor.

References

1. K. Iida, *A Review of Fatigue Failures in LWR Plants in Japan*, Nucl. Eng. Des. **138**, 297–312 (1992).

2. *ASME Boiler and Pressure Vessel Code Section III – Rules for Construction of Nuclear Power Plant Components*, The American Society of Mechanical Engineers, 345 East 47th Street, New York, NY 10017, 1992 Ed.

3. D. A. Hale, S. A. Wilson, E. Kiss, and A. J. Gianuzzi, *Low Cycle Fatigue Evaluation of Primary Piping Materials in a BWR Environment*, GEAP–20244, U.S. Nuclear Regulatory Commission (Sept. 1977).

4. D. A. Hale, S. A. Wilson, J. N. Kass, and E. Kiss, *Low Cycle Fatigue Behavior of Commercial Piping Materials in a BWR Environment*, J. Eng. Mater. Technol. **103**, 15–25 (1981).

5. S. Ranganath, J. N. Kass, and J. D. Heald, *Fatigue Behavior of Carbon Steel Components in High–Temperature Water Environments*, in Low–Cycle Fatigue and Life Prediction, ASTM STP 770, C. Amzallag, B. N. Leis, and P. Rabbe, eds., American Society for Testing and Materials, Philadelphia, PA, pp. 436–459 (1982).

6. S. Ranganath, J. N. Kass, and J. D. Heald, *Fatigue Behavior of Carbon Steel Components in High–Temperature Water Environments*, in BWR Environmental Cracking Margins for Carbon Steel Piping, EPRI NP–2406, Electric Power Research Institute, Palo Alto, CA, Appendix 3 (May 1982).

7. J. B. Terrell, *Fatigue Life Characterization of Smooth and Notched Piping Steel Specimens in 288°C Air Environments*, NUREG/CR–5013, EM–2232 Materials Engineering Associates, Inc., Lanham, MD (May 1988).

8. J. B. Terrell, *Fatigue Strength of Smooth and Notched Specimens of ASME SA 106–B Steel in PWR Environments*, NUREG/CR–5136, MEA–2289, Materials Engineering Associates, Inc., Lanham, MD (Sept. 1988).

9. J. B. Terrell, *Effect of Cyclic Frequency on the Fatigue Life of ASME SA–106–B Piping Steel in PWR Environments*, J. Mater. Eng. **10**, 193–203 (1988).

10. P. D. Hicks, in *Environmentally Assisted Cracking in Light Water Reactors: Semiannual Report October 1990—March 1991*, NUREG/CR–4667 Vol. 12, ANL–91/24, pp. 3–18 (Aug. 1991).

11. P. D. Hicks and W. J. Shack, in *Environmentally Assisted Cracking in Light Water Reactors, Semiannual Report, April–September 1991*, NUREG/CR–4667 Vol. 13, ANL–92/6, pp. 3–8 (March 1992).

12. O. K. Chopra, W. F. Michaud, and W. J. Shack, in *Environmentally Assisted Cracking in Light Water Reactors, Semiannual Report, October 1992–March 1993*, NUREG/CR–4667 Vol. 16, ANL–93/27, pp. 3–19 (Sept. 1993).

13. O. K. Chopra, W. F. Michaud, W. J. Shack, and W. K. Soppet, in *Environmentally Assisted Cracking in Light Water Reactors, Semiannual Report, April–September 1993*, NUREG/CR–4667 Vol. 17, ANL–94/16, pp. 1–22 (June 1994).

14. O. K. Chopra, W. F. Michaud, and W. J. Shack, in *Environmentally Assisted Cracking in Light Water Reactors, Semiannual Report, October 1993—March 1994*, NUREG/CR-4667 Vol. 18, ANL-95/2, pp. 3-10 (March 1995).

15. O. K. Chopra, W. F. Michaud, and W. J. Shack, in *Environmentally Assisted Cracking in Light Water Reactors, Semiannual Report, April-September 1994*, NUREG/CR-4667 Vol. 19, ANL-95/25, pp. 3-18 (Sept. 1995).

16. O. K. Chopra and W. J. Shack, *Effects of LWR Environments on Fatigue Life of Carbon and Low-Alloy Steels*, in Fatigue and Crack Growth: Environmental Effects, Modeling Studies, and Design Considerations, PVP Vol. 306, S. Yukawa, ed., American Society of Mechanical Engineers, New York, pp. 95-109 (1995).

17. O. K. Chopra and W. J. Shack, *Effects of Material and Loading Variables on Fatigue Life of Carbon and Low-Alloy Steels in LWR Environments*, in Transactions of the 13th Int. Conf. on Structural Mechanics in Reactor Technology (SMiRT 13), Vol. II, M. M. Rocha and J. D. Riera, eds., Escola de Engenharia - Universidade Federal do Rio Grande do Sul, Porto Alegre, Brazil, pp. 551-562 (1995).

18. M. Higuchi and K. Iida, *Fatigue Strength Correction Factors for Carbon and Low-Alloy Steels in Oxygen-Containing High-Temperature Water*, Nucl. Eng. Des. **129**, 293-306 (1991).

19. K. Iida, H. Kobayashi, and M. Higuchi, *Predictive Method of Low Cycle Fatigue Life of Carbon and Low Alloy Steels in High Temperature Water Environments*, NUREG/CP-0067, MEA-2090, Vol. 2, Materials Engineering Associates, Inc., Lanham, MD (April 1986).

20. N. Nagata, S. Sato, and Y. Katada, *Low-Cycle Fatigue Behavior of Low-Alloy Steels in High-Temperature Pressurized Water*, in Transactions 10th Int. Conf. on Structural Mechanics in Reactor Technology, F. A. H. Hadjian, ed., American Assn. for Structural Mechanics in Reactor Technology, Anaheim, CA (1989).

21. M. Higuchi, K. Iida, and Y. Asada, *Effects of Strain Rate Change on Fatigue Life of Carbon Steel in High-Temperature Water*, in Fatigue and Crack Growth: Environmental Effects, Modeling Studies, and Design Considerations, PVP Vol. 306, S. Yukawa, ed., American Society of Mechanical Engineers, New York, pp. 111-116 (1995).

22. H. Kanasaki, M. Hayashi, K. Iida, and Y. Asada, *Effects of Temperature Change on Fatigue Life of Carbon Steel in High Temperature Water*, in Fatigue and Crack Growth: Environmental Effects, Modeling Studies, and Design Considerations, PVP Vol. 306, S. Yukawa, ed., American Society of Mechanical Engineers, New York, pp. 117-122 (1995).

23. G. Nakao, H. Kanasaki, M. Higuchi, K. Iida, and Y. Asada, *Effects of Temperature and Dissolved Oxygen Content on Fatigue Life of Carbon and Low-Alloy Steels in LWR Water Environment, in* Fatigue and Crack Growth: Environmental Effects, Modeling Studies, and Design Considerations, PVP Vol. 306, S. Yukawa, ed., American Society of Mechanical Engineers, New York, pp. 123-128 (1995).

24. S. Majumdar, O. K. Chopra, and W. J. Shack, *Interim Fatigue Design Curves for Carbon, Low-Alloy, and Austenitic Stainless Steels in LWR Environments*, NUREG/CR-5999, ANL-93/3 (April 1993).

25. J. Keisler, O. K. Chopra, and W. J. Shack, *Statistical Analysis of Fatigue Strain-Life Data for Carbon and Low-Alloy Steels*, NUREG/CR-6237, ANL-94/21 (Aug. 1994).

26. J. M. Keisler and O. K. Chopra, *Statistical Analysis of Fatigue Strain-Life Data for Carbon and Low-Alloy Steels*, in Risk & Safety Assessments: Where is the Balance, PVP Vol. 296/SERA-Vol. 3, F. L. Cho, ed., American Society of Mechanical Engineers, New York, pp. 355–366 (1995).

27. L. A. James, *The Effect of Temperature and Cyclic Frequency Upon Fatigue Crack Growth Behavior of Several Steels in an Elevated Temperature Aqueous Environment*, J. Pressure Vessel Technol. **116**, 122–127 (1994).

28. L. A. James, *Ramberg–Osgood Strain-Hardening Characterization of an ASTM A302-B Steel*, J. Pressure Vessel Technol. **117** (1995).

29. F. P. Ford, S. Ranganath, and D. Weinstein, *Environmentally Assisted Fatigue Crack Initiation in Low-Alloy Steels – A Review of the Literature and the ASME Code Design Requirements*, Electric Power Research Institute, Palo Alto, CA, EPRI Report TR-102765 (Aug. 1993).

30. W. E. Ruther, W. K. Soppet, and T. F. Kassner, in *Environmentally Assisted Cracking in Light Water Reactors, Semiannual Report, April–September 1994*, NUREG/CR-4667 Vol. 19, ANL-95/25, pp. 17–32 (Sept. 1995).

31. J. M. Sarver, J. R. Crum, and W. L. Mankins, *Carbide Precipitation and the Effect of Thermal Treatments on the SCC Behavior of Inconel Alloy 690*, Proc. 3rd Int. Symp. Environmental Degradation of Materials in Nuclear Power Systems – Water Reactors, G. J. Theus and J. R. Weeks, eds., The Metallurgical Society, Warrendale, PA, pp. 581–586 (1988).

32. P. L. Andresen and F. P. Ford, *Irradiation Assisted Stress Corrosion Cracking: From Modeling and Prediction of Laboratory and In-Core Response to Component Life Prediction*, Corrosion '95, Paper No. 419, Orlando, FL (March 1995).

33. M. E. Indig, J. L. Nelson, and G. P. Wozadlo, *Investigation of the Protection Potential Against IASCC*, in Proc. 5th Int. Symp. Environmental Degradation of Materials in Nuclear Power Systems – Water Reactors, D. Cubicciotti, E. P. Simonen, and R. E. Gold, eds., American Nuclear Society, La Grange Park, IL, pp. 941–947 (1992).

34. M. Kodama, S. Nishimura, J. Morisawa, S. Shima, S. Suzuki, and M. Yamamoto, *Effects of Fluence and Dissolved Oxygen on IASCC in Austenitic Stainless Steels*, in Proc. 5th Int. Symp. Environmental Degradation of Materials in Nuclear Power Systems – Water Reactors, D. Cubicciotti, E. P. Simonen, and R. Gold, eds., American Nuclear Society, La Grange Park, IL, pp. 948-954 (1992).

35. M. Kodama, R. Katsura, J. Morisawa, S. Nishimura, S. Suzuki, K. Asano, K. Fukuya, and K. Nakata, *IASCC Susceptibility of Austenitic Stainless Steels Irradiated to High Neutron Fluence*, in Proc. 6th Int. Symp. on Environmental Degradation of Materials in Nuclear Power Systems - Water Reactors, R. E. Gold and E. P. Simonen, eds., The Minerals, Metals, and Materials Society, Warrendale, PA, pp. 583–588 (1993).

36. R. Katsura, J. Morisawa, M. Kodama, S. Nishimura, S. Suzuki, S. Shima, and M. Yamamoto, *Effect of Stress on IASCC in Irradiated Austenitic Stainless Steels*, in Proc. 6th Int. Symp. on Environmental Degradation of Materials in Nuclear Power Systems - Water Reactors, R. E. Gold and E. P. Simonen, eds., The Minerals, Metals, and Materials Society, Warrendale, PA, pp. 625–631 (1993).

37. A. Jenssen and L. G. Ljungberg, *Irradiation Assisted Stress Corrosion Cracking of Stainless Steel Alloys in BWR Normal Water Chemistry and Hydrogen Water Chemistry*, in Proc. 6th Int. Symp. on Environmental Degradation of Materials in Nuclear Power Systems - Water Reactors, R. E. Gold and E. P. Simonen, eds., The Minerals, Metals, and Materials Society, Warrendale, PA, pp. 547–553 (1993).

38. H. M. Chung, W. E. Ruther, J. E. Sanecki, A. G. Hins, and T. F. Kassner, *Stress Corrosion Cracking Susceptibility of Irradiated Type 304 Stainless Steels*, in Effects of Radiation on Materials: 16th Int. Symp., ASTM STP 1175, A. S. Kumar, D. S. Gelles, R. K. Nanstad, and T. A. Little, eds., American Society for Testing and Materials, Philadelphia, pp. 851–869 (1993).

39. H. M. Chung, W. E. Ruther, J. E. Sanecki, and T. F. Kassner, *Grain-Boundary Microchemistry and Intergranular Cracking of Irradiated Austenitic Stainless Steel*, in Proc. 6th Int. Symp. on Environmental Degradation of Materials in Nuclear Power Systems - Water Reactors, R. E. Gold and E. P. Simonen, eds., The Minerals, Metals, and Materials Society, Warrendale, PA, pp. 511–519 (1993).

40. H. M. Chung, W. E. Ruther, and A. Hins, in *Environmentally Assisted Cracking in Light Water Reactors: Semiannual Report, April 1994–September 1994*, NUREG/CR–4667 Vol. 19, ANL–95/25, pp. 32–42 (Sept. 1995).

41. H. M. Chung, W. E. Ruther, and J. E. Sanecki, in *Environmentally Assisted Cracking in Light Water Reactors: Semiannual Report, October 1993–March 1994*, NUREG/CR–4667 Vol. 18, ANL–95/2, pp. 27–35 (March 1995).

42. F. Garzarolli, P. Dewes, R. Hahn, and J. L. Nelson, *Deformability of High-Purity Stainless Steels and Ni-Base Alloys in the Core of a PWR*, in Proc. 6th Int. Symp. on Environmental Degradation of Materials in Nuclear Power Systems - Water Reactors, R. E. Gold and E. P. Simonen, eds., The Minerals, Metals, and Materials Society, Warrendale, PA, pp. 607–613 (1993).

43. M. Kodama, J. Morisawa, S. Nishimura, K. Asano, S. Shima, and K. Nakata, *Stress Corrosion Cracking and Intergranular Corrosion of Austenitic Stainless Steels Irradiated at 323 K*, J. Nucl. Mater., **212–215**, 1509–1514 (1994).

44. J. M. Cookson, D. L. Damcott, G. S. Was, and P. L. Andresen, *The Role of Microchemical and Microstructural Effects in the IASCC of High Purity Austenitic Stainless Steels*, in Proc. 6th Int. Symp. on Environmental Degradation of Materials in Nuclear Power Systems - Water Reactors, R. E. Gold and E. P. Simonen, eds., The Minerals, Metals, and Materials Society, Warrendale, PA, pp. 573–580 (1993).

45. S. Kasahara, K. Nakata, K. Fukuya, S. Shima, A. J. Jacobs, G. P. Wozadlo, and S. Suzuki, *The Effects of Minor Elements on IASCC Susceptibility in Austenitic Stainless Steels Irradiated with Neutrons*, in Proc. 6th Int. Symp. on Environmental Degradation of Materials in Nuclear Power Systems - Water Reactors, R. E. Gold and E. P. Simonen, eds., The Minerals, Metals, and Materials Society, Warrendale, PA, pp. 615–622 (1993).

46. H. M. Chung, W. E. Ruther, and J. E. Sanecki, in *Environmentally Assisted Cracking in Light Water Reactors: Semiannual Report, April 1993–September 1993*, NUREG/CR–4667 Vol. 17, ANL–94/16, pp. 35–41 (June 1994).

47. C. T. Ward, D. L. Mathis, and R. W. Staehle, *Intergranular Attack of Sensitized Austenitic Stainless Steel by Water Containing Fluoride Ions*, Corrosion **25**, 394–396 (1969).

Distribution for NUREG/CR-4667, Vol. 20 (ANL-95/41)

Internal

W. J. Shack (45)

TIS Files

External

NRC, for distribution per R5

Libraries

ANL-E (2)

ANL-W

Manager, Chicago Field Office, DOE

Energy Technology Division Review Committee:

H. K. Birnbaum, University of Illinois, Urbana

R. C. Buchanan, University of Cincinnati, Cincinnati, OH

S. N. Liu, Fremont, CA

H. S. Rosenbaum, Fremont, CA

R. K. Shah, University of Kentucky, Lexington

S. Smialowska, Ohio State University, Columbus

R. E. Smith, Altran Corporation, Huntersville, NC

P. L. Andresen, General Electric Corporate Research and Development, Schenectady, NY

T. A. Auten, Knolls Atomic Power Laboratory

R. G. Ballinger, Massachusetts Institute of Technology, Cambridge, MA

W. H. Bamford, Westinghouse Electric Corp., Pittsburgh

J. M. Boursier, Electricite de France-Generating and Transmission Group Central Laboratories, Avoine, France

S. M. Bruemmer, Battelle Pacific Northwest Laboratory

H. S. Chung, Korea Atomic Energy Research Institute, Daejeon, Korea

L. Coressti, ABB CE Nuclear Power, Windsor, CT

R. L. Cowan, General Electric Co., San Jose, CA

G. Cragnolino, Southwest Research Inst., San Antonio, TX

W. H. Cullen, Materials Engineering Assoc., Inc., Lanham, MD

E. D. Eason, Modeling and Computing Services, Newark, CA

J. Fish, Knolls Atomic Power Laboratory

J. P. Foster, Westinghouse Electric Corp., Pittsburgh

M. Fox, Tucson, AZ

D. G. Franklin, Bettis Atomic Power Laboratory

Y. S. Garud, S. Levy, Inc., Campbell, CA

F. Garzarolli, KWU, Erlangen, Germany

J. Gilman, Electric Power Research Inst., Palo Alto, CA

B. M. Gordon, General Electric Co., San Jose, CA

M. M. Hall, Bettis Atomic Power Laboratory

J. W. Halley, U. Minnesota, Minneapolis

H. E. Hanninen, Technical Research Centre of Finland, Espoo

D. Harrison, USDOE, Germantown, MD

J. Hickling, CML Capcis March Ltd., Erlangen-Tennonlohe, Germany

M. Higuchi, Ishikawajima-Harima Heavy Industries Co., Ltd., Japan

C. Hoffmann, ABB CE Nuclear Power, Windsor, CT

H. S. Isaacs, Brookhaven National Laboratory

A. Jacobs, General Electric Co., San Jose, CA

L. James, Bettis Atomic Power Laboratory

C. Jansson, Vattenfall Energisystem, Vallingby, Sweden

D. P. Jones, Bettis Atomic Power Laboratory

R. H. Jones, Battelle Pacific Northwest Laboratory

R. L. Jones, Electric Power Research Institute, Palo Alto, CA

T. Karlsen, OECD Halden Reactor Project, Halden, Norway

C. Kim, Westinghouse Electric Corp., Pittsburgh

L. Ljungberg, ASEA-ATOM, Vasteras, Sweden

D. D. Macdonald, Pennsylvania State University, University Park

T. R. Mager, Westinghouse Electric Corp., Pittsburgh

R. D. McCright, Lawrence Livermore National Laboratory

A. R. McIlree, Electric Power Research Institute, Palo Alto, CA

H. Metha, General Electric Co., San Jose, CA

D. Morgan, Pennsylvania Power and Light Co., Allentown, PA

J. L. Nelson, Electric Power Research Inst., Palo Alto, CA

M. Pytel, Structural Integrity Associates, San Jose, CA

M. Prager, Materials Properties Council, New York, NY

S. Ranganath, General Electric Co., San Jose, CA

P. M. Scott, Framatome, Paris, France

A. J. Sedriks, Office of Naval Research, Arlington, VA

C. Shepherd, AEA Technology-Harwell Labs., Didcot, Oxon, UK

H. D. Solomon, General Electric Corporate Research and Development, Schenectady, NY

M. O. Speidel, Swiss Federal Institute of Technology, Zurich, Switzerland

D. M. Stevens, Lynchburg Research Center, Babcock & Wilcox Co., Lynchburg, VA

P. Tipping, Swiss Federal Nuclear Safety Inspectorate, Villigen, Switzerland

W. A. Van Der Sluys, Research & Development Division, Babcock & Wilcox Co., Alliance, OH

J. C. Van Duysen, Electricite de France-Research and Development Centre de Renardieres, Moret-sur-Loing, France

C. Vitanza, OECD Halden Reactor Project, Halden, Norway

G. S. Was, University of Michigan, Ann Arbor

J. R. Weeks, Brookhaven National Laboratory

S. Yukawa, Boulder, CO

NRC FORM 335 (2-89) NRCM 1102, 3201, 3202

U. S. NUCLEAR REGULATORY COMMISSION

BIBLIOGRAPHIC DATA SHEET

(See instructions on the reverse)

1. REPORT NUMBER *(Assigned by NRC. Add Vol., Supp., Rev., and Addendum Numbers, if any.)*
NUREG/CR-4667, Vol. 20
ANL-95/41

2. TITLE AND SUBTITLE
Environmentally Assisted Cracking in Light Water Reactors.
Semiannual Report October 1994—March 1995

3. DATE REPORT PUBLISHED
MONTH: January
YEAR: 1996

4. FIN OR GRANT NUMBER
A2212

5. AUTHOR(S)
H. M. Chung, O. K. Chopra, D. J. Gavenda, A. G. Hins,
T. F. Kassner, W. E. Ruther, W. J. Shack, and W. K. Soppet

6. TYPE OF REPORT
Technical; Semiannual

7. PERIOD COVERED *(Inclusive Dates)*
October1994—March 1995

8. PERFORMING ORGANIZATION - NAME AND ADDRESS *(If NRC, provide Division, Office or Region, U.S. Nuclear Regulatory Commission, and mailing address; if contractor, provide name and mailing address.)*

Argonne National Laboratory
9700 South Cass Avenue
Argonne, IL 60439

9. SPONSORING ORGANIZATION - NAME AND ADDRESS *(If NRC, type "Same as above"; if contractor, provide NRC Division, Office or Region, U.S. Nuclear Regulatory Commission, and mailing address.)*

Division of Engineering Technology
Office of Nuclear Regulatory Research
U. S. Nuclear Regulatory Commission
Washington, DC 20555-0001

10. SUPPLEMENTARY NOTES

M. McNeil, NRC Project Manager

11. ABSTRACT (200 words or less)

This report summarizes work performed by Argonne National Laboratory on fatigue and environmentally assisted cracking (EAC) in light water reactors (LWRs) from October 1994 to March 1995. Topics that have been investigated include (a) fatigue of carbon and low-alloy steel used in reactor piping and pressure vessels, (b) EAC of Alloy 600 and 690, and (c) irradiation-assisted stress corrosion cracking (IASCC) of Type 304 SS. Fatigue tests were conducted on ferritic steels in water with several dissolved-oxygen (DO) concentrations to determine whether a slow strain rate applied during different portions of a tensile-loading cycle are equally effective in decreasing fatigue life. Tensile properties and microstructures of several heats of Alloy 600 and 690 were characterized for correlation with EAC of the alloys in simulated LWR environments. Effects of DO and electrochemical potential on susceptibility to intergranular cracking of high- and commercial-purity Type 304 SS specimens from control-blade absorber tubes and a control-blade sheath irradiated in boiling water reactors were determined in slow-strain-rate-tensile tests at 289°C. Microchemical changes in the specimens were studied by Auger electron spectroscopy and scanning electron microscopy to determine whether trace impurity elements may contribute to IASCC of these materials.

12. KEY WORDS/DESCRIPTORS *(List words or phrases that will assist researchers in locating this report.)*
Corrosion Fatigue
Crack Growth
Irradiation-Assisted Stress Corrosion Cracking
Radiation-Induced Segregation
Stress Corrosion Cracking
A106-Gr B Steel
A302-Gr B Steel
A533-Gr B Steel
Alloy 600 and 690
Type 304 Stainless Steel

13. AVAILABILITY STATEMENT
Unlimited

14. SECURITY CLASSIFICATION
(This Page)
Unclassified
(This Report)
Unclassified

15. NUMBER OF PAGES

16. PRICE

Federal Recycling Program

NUREG/CR-4667, Vol. 20 has been
reproduced from the best available copy.